Glucose and Glutamine in the Tumor Microenvironment and CD8 T Cell Function

By

Matthew Zachary Madden

Dissertation
Submitted to the Faculty of the
Graduate School of Vanderbilt University
in partial fulfillment of the requirements
for the degree of

DOCTOR OF PHILOSOPHY
in

Molecular Pathology and Immunology
May 31, 2022
Nashville, Tennessee

Approved:

Meenakshi S. Madhur, M.D., Ph.D.
Young J. Kim, M.D., Ph.D.
Holly M. Algood, Ph.D.
Michael R. Savona, M.D.
Jeffrey C. Rathmell, Ph.D.

ACKNOWLEDGEMENTS

Many people and institutions directly contributed to this work. First, I would like to acknowledge the coauthors who contributed to the published manuscripts that are part of this dissertation (Chapter 1: Madden & Rathmell 2021; Chapter 2: Reinfeld & Madden et al 2021; Chapter 4: Levine & Hiam-Galvez et al 2021). For potential coauthors of unpublished work in Chapter 3, Lihong Bishop and John Wilson contributed reagents and expertise for STING agonism (Figure 3.6), Sam Schaefer maintained GLUT1 transgenic mice (Figure 3.8), Fiona Yull contributed mice and expertise for studying NfκB in myeloid cells (Figure 3.9), and Nowrin Chowdhury and Dawn Newcomb contributed mice and expertise for studying lung inflammation (Figure 3.10). Of potential coauthors for experiments in Chapter 4, Xiang Ye, Gabe Needle, and John Karijolich provided expertise and analysis for RNAseq and CUT&RUNseq experiments; Channing Chi, Jason Muka, Kianna Robinson, Melissa Wolf, Jackie Bader, Emilie Fisher, Brad Reinfeld, Sam Schaefer, and Debo Dahunsi helped perform experiments; Richard O'Neil provided MC38-OVA cells; and Mary Philip provided expertise and Lm-OVA. Patients treated at Vanderbilt University Medical Center generously contributed samples for analyses (Figures 2.1, 2.10, 2.11, 4.1, Table 2.1). Funding sources for this work include those acknowledged in the published manuscripts including from NIH (F30CA239367 & R01CA217987). We thank the NIH Tetramer Core Facility (contract number 75N93020D00005) for providing SIINFEKL PE tetramer and the Vanderbilt Institute for Advanced Genomics (VANTAGE) for library preparation and sequencing of RNAseq and CUT&RUNseq experiments. Figures 1.1, 2.1d, 2.3d, 2.5f, 2.16k, and 4.2c were created using Biorender.com.

I would like to thank my committee members for their consistent feedback and encouragement. Channing Chi, Kianna Robinson, and Jason Muka were undergraduate mentees in the lab. I hope they learned as much from me as I did from them. I would like to acknowledge all members of the Jeff and Kim Rathmell labs for their help, their encouragement, and for an enjoyable work environment. Specifically, I would like to thank more senior lab members Marc Johnson, Katy Beckerman, and Frank Mason for their mentorship, and fellow graduate students Brad Reinfeld and Melissa Wolf for working shoulder-to-shoulder with me through dozens of experiments. Thanks to the Justin Balko lab and Maggie Axelrod for tolerating our work in the lead castle. David Yu originally inspired me to pursue a career as a physician scientist and has been a great role model. Luc Van Kaer introduced me to immunology during the first year of medical school, and I may not have pursued graduate work in immunology if it were not for his enrapturing teaching. Mentors Jeff and Kim Rathmell been instrumental not only in this work but also in my development as a scientist. I will be forever grateful for the support they provided. I hope to pay forward the benefits of Jeff's mentorship to future trainees. The Vanderbilt Medical Scientist Training Program has been an ideal institution and community to complete my MD/PhD training. Finally, I would like to thank my friends (Abin Abraham, Maxwell Roeske, Matt Wleklinski, Kelsey McNew, and others) and family (Cathy Madden, Mark Madden, Jennifer Madden, Scott Krummey, Laura Dellalana) for their endless encouragement.

TABLE OF CONTENTS

LIST OF FIGURES

LIST OF TABLES

CHAPTER 1: INTRODUCTION

Portions of this chapter were adapted from the following manuscript published in *Cancer Discovery*:

Madden, M.Z. and Rathmell, J.C., 2021. The complex integration of T-cell metabolism and immunotherapy. Cancer Discovery, 11(7), pp.1636-1643.

Introduction to the immune system

The immune system is a network of barriers, proteins, and cells which protects a host organism from pathogens and other insults and promotes tissue homeostasis. Although the immune system is often initially framed as a mechanism for the clearance of microorganisms, its role in the promotion and resolution of inflammation across diverse diseases, including cancer, autoimmune disease, and cardiovascular disease, has been increasingly appreciated. Therapeutics targeting the immune system are of growing interests to advance human health (Murphy & Weaver 2017).

The immune system can be categorized into the innate and adaptive immune system and according to its components. This introduction will focus on the cellular components of the immune system, but it should be noted that barriers and proteins also play critical roles. Impermeable barriers such as skin and mucosa prevent the entry of pathogens into vulnerable tissues. The complement system and antimicrobial peptides are examples of proteins that help eliminate broad pathogens, and antibodies are proteins produced by the adaptive immune system to neutralize and eradicate specific pathogens. The primary “immune cells” in adult mice and humans are bone marrow-derived leukocytes or “white blood cells”. However, many non-circulating tissue-resident cells are critical for organ-specific immune protection and

homeostasis. Alternatively, any cell could be considered an “immune cell” since nearly all cells express machinery that can recognize pathogens or cellular damage to initiate an immune response and would subsequently participate during an immune response. However, for the purpose of this dissertation, “immune cells” refers specifically to leukocytes.

The innate immune cells are the “first line of defense” against invading microorganisms and can react within seconds when damage occurs. Innate cells express receptors that recognize pathogen- and damage-associated molecular patterns (PAMPs and DAMPs) which are general signals of infection and/or pathophysiology. Upon recognition of PAMPs and DAMPs, innate immune cells can exert effector function to promote inflammation and clearance of pathogens. Immune cells are specialized according to the type of immune response required by a particular pathogen or insult. Granulocytes such as neutrophils, eosinophils, and basophils, contain intracellular collections of protein called granules that can be released on pathogens. Neutrophils are important for the clearance of extracellular bacteria. Their effector functions include the production of antimicrobial peptides and immune signaling molecules known as cytokines, engulfment of bacteria for elimination (phagocytosis), and production of neutrophil extracellular traps (NETs) (Mantovani et al 2011). Eosinophils and basophils are important for the clearance of fungi and multicellular parasites. Eosinophils also contribute to pathologies such as asthma and allergy, and basophils are implicated in the life-threatening complication anaphylaxis when triggered by a specific antigen, a molecular ligand that may or may not be part of a pathogen (Wen & Rothenberg 2016). Innate lymphocytes, distinguished by their small round morphology, are another class of innate immune cell. Natural killer (NK) cells and innate lymphoid cells (ILCs) are important for specific types of immune responses against cancer and intracellular

infections including viruses and mycobacterium (NK cells and ILC type 1), parasites and fungi (ILC type 2), and extracellular bacteria (ILC type 3) (Cong 2020).

Apart from granulocytes and innate lymphocytes, macrophages and monocytes, their circulating precursors, are critical effector cells for early immunity and for the resolution of inflammation. Macrophages are phagocytes which engulf pathogens and debris for clearance. They also release cytokines to help recruit other immune cells and inform the subsequent type of immune response. Distinct from granulocytes, macrophages can play a key role in activating lymphocytes, and may be considered “professional” antigen-presenting cells (APCs) (Lavin et al 2015). Upon phagocytosis of a pathogen, macrophages can digest the proteins of the pathogen into smaller peptides and recycle these peptides bound to major histocompatibility complex class II (MHCII) as a ligand on their cell surface. Peptide bound to MHC is an antigen, the ligand for a lymphocyte receptor. On the cell surface, it can be recognized by a T cell receptor for T cell activation, part of the adaptive immune system.

The “most professional” APC is the dendritic cell (DC). Dendritic cells are specialized to sample antigens in a tissue microenvironment, become activated by inflammatory PAMPs and DAMPs, depart the inflamed tissue, home to a secondary lymphoid organ such as a lymph node, and then present antigen to lymphocytes and thereby initiate the adaptive immune response. Besides presenting MHC-bound peptides to T cells, DCs also secrete cytokines reflecting the type of inflammatory microenvironment from which they came, thereby tailoring the differentiation of their activated T cell towards a pathogen-appropriate effector function (Kapensberg 2003).

T cells are lymphocytes derived from the bone marrow like other immune cells but uniquely mature in the thymus (Klein et al 2014). In the thymus, each T cell precursor begins to express a genetically-recombined T cell receptor (TCR), the lineage-defining surface molecule of T cells. Each T cell has a TCR with a different specificity for their ligand peptide-MHC. In the thymus, both self-reactive T cells and T cells with useless TCRs that do not recognize peptide-MHC are deleted. T cells with TCRs demonstrating high affinity for self-peptide-MHC presented by thymic epithelial cells are terminated ("negative selection"), those with no or minimal affinity for self-peptide-MHC die in the absence of survival signals ("death by neglect"), and those with low tonic TCR affinity receive pro-survival signaling, proliferate, and exit the thymus as mature T cells ("positive selection"). CD4 is a TCR coreceptor recognizing MHCII and CD8 is a coreceptor recognizing MHCI, so CD4 T cells recognize peptide-MHCII derived from the endosomal (extracellular) compartment of the APC and CD8 T cells recognize peptide-MHCI derived from the cytoplasmic compartment of the APC. While all nucleated cells present peptides from their cytoplasmic cellular compartment on MHC class I, professional APCs also degrade proteins from the extracellular environment and endosomal compartment to present peptides on MHCII.

After activation by DCs, T cells grow, proliferate, and depart secondary lymphoid organs to home to inflamed tissue. There, they exert effector function according to their activation status and other environmental cues. For type 1 immunity against cancer and intracellular infection, CD8 T cells eliminate transformed or infected cells through the effector molecules perforin and granzyme B. They are also known as cytotoxic lymphocytes (CTL). CD4 T helper 1 cells (Th1) also promote type 1 immunity through the secretion of Interferon-γ. For type 2 immunity against

multicellular fungi and parasites, CD4 Th2 cells secrete interleukins 4 (IL4), IL5, and IL13, and for type 3 immunity against extracellular bacteria CD4 Th17 cells secrete IL17. Anti-inflammatory regulatory T cells (Treg) (peripheral Treg, pTreg) expressing master transcription factor FOXP3 can also differentiate, although Treg (thymic Treg, tTreg) can also mature in the thymus after demonstrating moderate affinity for self-peptide-MHC. CD4 T cells can also differentiate into follicular helper cells (Tfh). Tfh promote antibody responses by B cells (Zhu et al 2010). Like T cells, B cells are lymphocytes that express an analogous genetically-recombined B cell receptor (BCR) which recognizes antigen independent of MHC. Therefore, unlike TCRs, BCRs are not restricted to recognizing proteins and can theoretically recognize any antigen and bind any specific epitope. After receiving Tfh costimulatory signals, B cells activate and differentiate into antibody secreting cells (ASCs) including plasma cells. An antibody is a secreted form of the BCR and is important for binding to pathogens for neutralization and elimination. Antibodies are a secreted proteins found in plasma and are therefore considered the humoral component of adaptive immunity in contrast to the cellular component of T and B cells (LeBien & Tedder 2008).

Once activated, the innate and adaptive immune systems can form a cycle whereby T and B cell effector functions drive further inflammation, innate immune activity, and antigen presentation to more T and B cells (Chen & Mellman 2013). If the pathogen and the specific antigens driving T and B cell activity are cleared, then inflammation can be resolved. Setting them apart from the innate immune system, T and B cells are antigen-specific and can persist long term as memory lymphocytes to protect against repeat infections from the same antigens. Memory lymphocytes are primed for reactivation and persist in circulation, in lymphoid organs, and in tissue. Together

with antibodies produced by long-lived plasma cells, memory lymphocytes provide the "immunity" to pathogens associated with convalescence after infection or vaccination (Kumar et al 2018).

Identification of critical cells and molecules driving a specific immune response can lead to the development of targeted therapeutics to modulate inflammation and immunity. Corticosteroids, analogs of the stress hormone cortisol, are broadly immunosuppressive and are commonly used in clinical practice across multiple indications. Targeted therapies antagonizing innate signaling cytokines tumor necrosis factor α (TNFα), IL1, and IL6 are now standards of care in autoimmune diseases, whereas cancer immunotherapies to stimulate the immune system have revolutionized oncology.

While many therapies have focused on activating or blocking immune signaling pathways, an emerging approach is to exploit differences in cellular metabolism in different immune cells. Although the field is gaining greater interest, targeting immunometabolism is also an old approach to immunomodulation, as methotrexate inhibits folate metabolism in activated lymphocytes. Just as specific molecules promote particular immune responses, the metabolic programs of those immune cells support their activities (O'Neill et al 2016). In this dissertation, we focus on T cell and macrophage metabolism, although exciting discoveries on cellular metabolism and its impact on immunity continue to be made in other cell types as well (Pearce & Everts 2015, O'Brien & Finlay 2019, Kumar & Dikshit 2019).

T cell metabolism

Resting T cells utilize an oxidative catabolic metabolism that undergoes a dramatic shift upon activation. Tonic signals from the TCR through RasGRP and the cytokine IL-7 signal to maintain a low basal activity of mechanistic Target of Rapamycin Complex I (mTORC1) in naïve T cells. Together with sphingosine-1 phosphate that promotes mitochondrial metabolism and oxidative phosphorylation, these pathways generate ATP essential for cell survival and immune surveillance (Myers et al 2019, Wofford et al 2008, Mendoza et al 2017). Upon antigen encounter, the TCR activates calcium signaling that can result in tolerance or anergy if co-stimulatory signals through receptors such as CD28 are not received to enhance TCR signals and robustly activate the Phosphatidylinositide-3-kinase (PI3K)/Akt/mTORC1 and Myc signaling pathways (Esensten et al 2016, Wang et al 2011). Importantly, TCR signals alone in the absence of co-stimulation do not efficiently trigger reprogramming to support anabolic metabolism essential for cell growth and effector differentiation (Frauwirth et al 2002, Zheng et al 2009) and T cells that fail or are unable to undergo metabolic reprogramming do not adopt effector functions. Conversely, T cells with excessive metabolic reprogramming can promote inflammation and autoimmunity (Jacobs et al 2008, Perry et al 2012). An appropriate balance of co-stimulatory signals, therefore, is essential to regulate T cell metabolism for efficient yet not excessive responses.

Metabolic programming for T cell activation involves transition from catabolism to the induction of a wide range of anabolic processes that resemble the metabolic transitions long known to occur in cancer (**Figure 1.1**). Oncogenic signals through PI3K, Myc, and others can lead to increased glucose uptake and metabolism with the production of lactate even in the presence of

abundant oxygen (Andrejeva & Rathmell et al 2017). This process, termed aerobic glycolysis, is similarly induced in T cells following TCR activation with co-stimulation and is limiting to establish the extent of T cell inflammatory function and proliferation (Jacobs et al 2008). Serine and one carbon metabolism, as well as glutamine uptake and oxidation, are also increased to support redox balance, nucleotide synthesis, and mitochondrial metabolism (Ma et al 2019, Johnson et al 2018). To support the increased flux required for these pathways, T cells upregulate nutrient transporters and uptake of glucose (Macintyre et al 2014) and amino acids, including glutamine and essential amino acids including methionine (Nakaya et al 2014, Sinclair et al 2019). Uptake and metabolism of additional amino acids are also important and can play key metabolic and immunomodulatory roles, with arginine and tryptophan in particular playing key roles to shape inflammation and anti-tumor immunity (Fiore et al 2021, Szefel et al 2019). Even uptake of the non-essential amino acid alanine is necessary to satisfy the high protein synthesis demand accompanying T cell activation (Ron-Harel et al 2019). Importantly, as T cells activate and are guided by inflammatory and cytokine cues to gain distinct sets of effector functions, they also develop and require specific metabolic programs (Michalek et al 2011). If these fail to establish or are blocked, T cells are unable to elicit effector functions and may instead develop into immune suppressive regulatory T cells (induced Treg, iTreg). While iTreg were can often rely on fatty acid oxidation, activated Treg *in vivo* may also utilize glycolysis during proliferation and for migration into tissues (Kishore et al 2018, Pacella et al 2019). In the tumor microenvironment, Treg utilize lactate oxidation for suppressive function in tumors, and Treg-specific deficiency of lactate transporter MCT1 (*Slc16a1*) reduces tumor growth (Watson et al 2021). Ultimately, Treg flexible utilization of glycolysis, lactate, and fatty acid metabolism

contributes to the overall immunosuppressive nature of the tumor microenvironment and may grant a selective advantage compared to effector T cells (Pacella et al 2018).

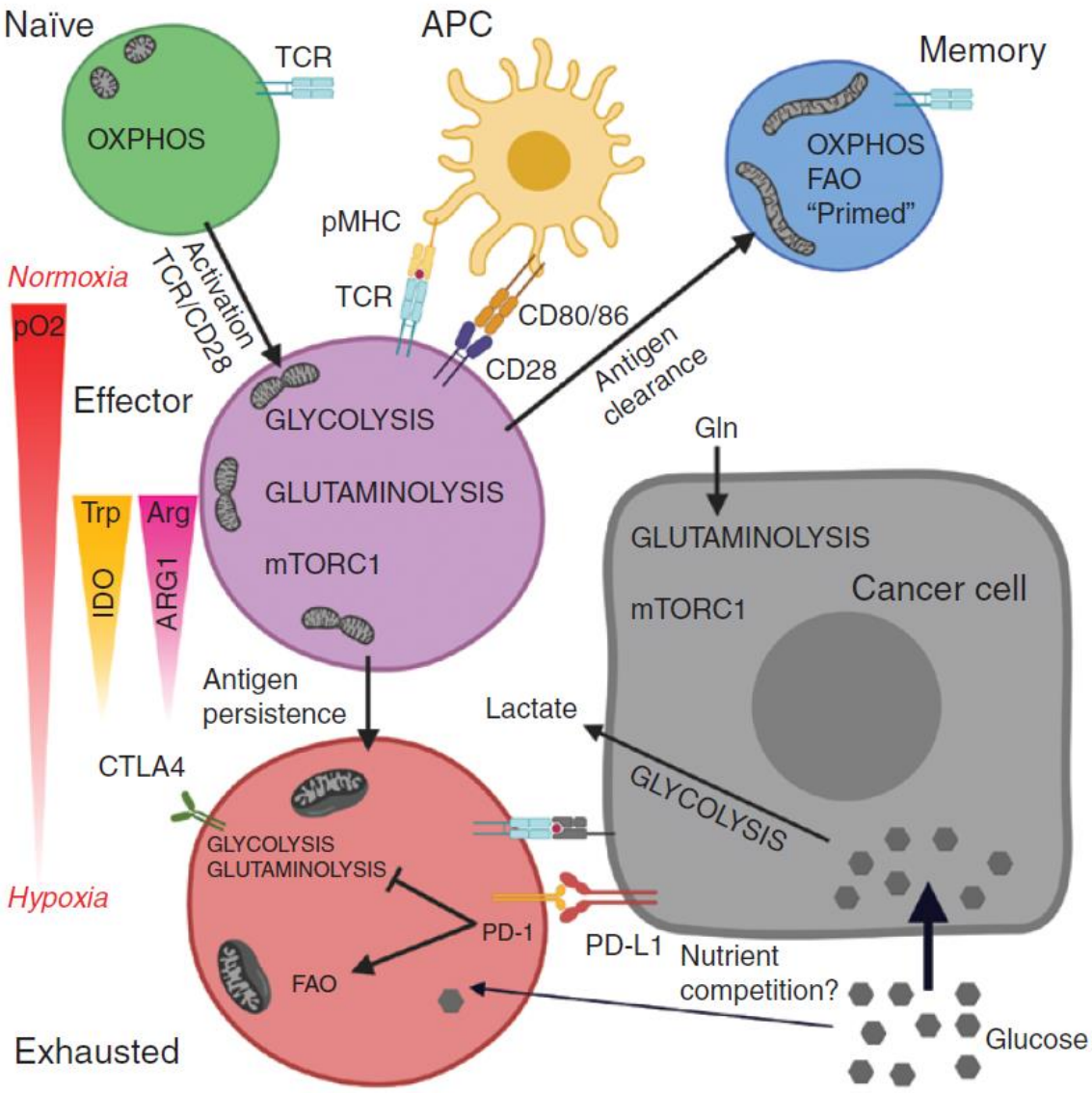

Figure 1.1: T cell metabolism drives T cell fate and function to eliminate tumors. Naïve T cells rely on oxidative metabolism (OXPHOS) and maintain robust mitochondrial quality control. After activation with co-stimulation through receptors including CD28 that activate the mTORC1 pathway, effector T cells increase glucose and glutamine (Gln) metabolism to support effector function. If antigen is cleared, effector cells can enter a long-lived memory state with stem cell-like properties. If antigen remains, as often occurs in long-term tumor elimination processes, inhibitory receptors such as PD-1 and CTLA4 can reshape T cell metabolism to reduce pathways that characterize effector T cells and lead to multiple metabolic impairments. Exhausted T cells demonstrate reduced glucose and glutamine metabolism, low quality dysfunctional mitochondrial, and a dependance on fatty acid oxidation (FAO). Potentially

contributing to T cell disfunction in the tumor microenvironment are low levels of oxygen (pO2), low levels of tryptophan (Trp) metabolized by the kynurenine pathway including indoleamine 2,3-dioxygenase (IDO), low levels of arginine (Arg) metabolized by arginase (ARG1), high levels of lactate, and potentially competition for glucose with cancer cells. Figure created with Biorender.com.

Transient TCR signaling from acutely cleared antigens leads to a distinct metabolic outcome compared to chronic stimulation from persistent antigens. Following acute antigen exposure and clearance, T cells that fail to reduce aerobic glycolysis undergo apoptosis while those that can revert back to catabolic metabolism using lipid oxidation as a primary fuel to support mitochondrial respiratory capacity can survive as memory cells (van der Windt et al 2012). The morphology of mitochondria can play a key role in electron transport efficiency, underlying mitochondrial capacity and fitness. Upon T cell activation mitochondria fragment and cristae remodel leading to relatively reduced oxidative phosphorylation, although overall metabolic flux is elevated compared to a non-activated T cell (Buck et al 2016). Transient inhibition of fragmentation during activation resulted in fused mitochondria that maintained mitochondrial oxygen consumption and supported long-term T cell survival and memory. Importantly, this treatment increased the ability of T cells to survive and eliminate tumors upon subsequent adoptive transfer (Buck et al 2016). A key characteristic of memory T cells is the ability to mount fast responses upon secondary antigen encounter. Metabolically, memory T cells remain poised through endoplasmic reticulum/mitochondrial associations and metabolic complexes to rapidly reactivate aerobic glycolysis to promote robust effector function and proliferation (Bantug et al 2018). Importantly, memory responses may be enhanced if anabolic cell metabolism is transiently suppressed during initial activation. While mechanisms are unclear, it is possible that mild metabolic stress, such as low dose 2-deoxyglucose to inhibit glycolysis, can

lead to mitochondrial adaptation to prime for future respiratory capacity and survival as memory cells (Sukumar et al 2013).

If antigens are not rapidly cleared, chronic antigen exposure can lead to T cell dysfunction, often termed T cell exhaustion. In contrast to memory T cells that are primed to quickly respond to restimulation, exhausted T cells do not produce the full array of inflammatory cytokines upon *ex vivo* stimulation, have reduced proliferative potential, express characteristic inhibitory coreceptors, and have epigenetic changes suggestive of terminal differentiation (Blank et al 2019). Exhausted T cells can also have marked metabolic dysfunction. Glucose uptake and mitochondrial oxidative metabolism are decreased, yet mitochondrial mass is increased (Bengsch et al 2016). Depolarized mitochondria accumulate in exhausted T cells, and pharmacologic enhancement of depolarization promotes epigenetic changes suggesting a causal link between metabolism and the transcriptional program of exhaustion (Yu et al 2020). Indeed, clearance of damaged and non-functional mitochondria to maintain a high level of mitochondrial quality control may be a key event to reinvigorate exhausted T cells and allow the generation of long-lived memory T cells (Bengsch et al 2016, Adams et al 2016). The combination of continuous TCR signaling with hypoxia induces an exhausted program in T cells by restricting mitochondrial regulation of ROS (Scharping et al 2021). Further, the ability of exogenous pyruvate or acetate to rescue exhausted T cell functions supports a central role for metabolic impairment in T cell exhaustion (Siska et al 2017, Qiu et al 2019).

These normal metabolic processes are critical to maintain T cell fitness and allow rapid and robust immunity. The distinct metabolic programs of different T cell subsets offer the promise of

specific modulation of immune responses through targeted therapies. Glutamine metabolism provides a striking example of selectivity and regulation of T cell responses. While all effector T cells require increased glutamine uptake upon activation and can instead differentiate into Treg when glutamine itself is limiting (Johnson et al 2018, Nakaya et al 2014), the further metabolism of glutamine differs between T cell subsets. Metabolism of glutamine through Glutaminase (GLS) to generate glutamate is required for CD4 Th17 cells and inhibition or genetic deletion of GLS is sufficient to provide protection in models of airway inflammation (Johnson et al 2018), inflammatory bowel disease (Johnson et al 2018), psoriasis (Xia et al 2020), and Systemic Lupus Erythematosus (Johnson et al 2017, Kono et al 2019). Conversely, glutamine metabolism appears to restrain the differentiation and function of CD4 Th1 and CD8 cytotoxic lymphocytes (CTL), as both cell types show increased markers of activation and effector function when glutamine metabolism is inhibited (Johnson et al 2017, Leone et al 2019). Increased differentiation upon GLS inhibition may come at the cost of excessive or terminal fates, however, as GLS-deficient Th1 cells also upregulated inhibitory receptors and appeared to lose function over time. It remains unclear if this ultimate decrease of overall function was due to reversion to a state similar to chronic antigen stimulation or terminal differentiation and increased susceptibility to apoptosis.

Changes in cell metabolism are now known to affect epigenetic marks and histone acetylation so as to influence gene expression and cell differentiation that can last long after T cells are removed from metabolic interventions (Britt et al 2020). This long-lasting impact of cell metabolism may affect both T cells that have left tumor microenvironments as well as adoptively transferred T cells that can be epigenetically programed in vitro through metabolic manipulation

for specific differentiation fates and to withstand metabolically hostile microenvironments. Acetylation of histones depends on acetyl donor molecule acetyl-CoA and the enzymatic activity of histone acetyl transferases. Cytoplasmic and nuclear acetyl-CoA is derived from fatty acid metabolism, TCA cycle citrate exported to the cytosol and converted to acetyl-CoA by ACLY, and acetate though the enzyme ACSS2. Enhanced nucleo-cytosolic acetyl-CoA, enhances epigenetic acetylation of effector molecule loci in T cells. Genetic ablation of lactate dehydrogenase reduced aerobic glycolysis and reduced IFNγ production and histone acetylation in Th1 cells by sequestering citrate in the TCA cycle to maintain cellular metabolism (Peng et al 2016). Acetate metabolism promotes CD8 effector function at sites of infection, but ACSS1/2 are downregulated in memory CD8 T cells potentially to prevent further epigenetic remodeling in these stem-like cells (Balmer et al 2020). Universal methyl donor S-adenosyl-L-methionine (SAM), necessary for histone and DNA methylation, is largely derived from methionine in activated T cells. Methionine restriction reduced Th17 cell effector molecule production and attenuated experimental autoimmune encephalitis pathology (Roy et al 2020) . Conversely, inhibition of glutamine metabolism may promote hypermethylated states as many demethylation reactions rely on the downstream glutamine metabolite α-ketoglutarate (Johnson et al 2017, Leone et al 2019). These epigenetic mechanisms now offer a straightforward *in vitro* metabolic approach to *in vivo* immunotherapy, as the epigenetic differentiation of effector immune cell therapy may be directly altered metabolically during *ex vivo* production

T cell-based Cancer Immunotherapy

Immunotherapy has revolutionized clinical oncology and now provides a distinct arm of cancer treatment to empower the immune system to eliminate cancer cells. Following on early efforts to

vaccinate against cancer that led to disappointing results, immunotherapy through Adoptive Cell Therapy (ACT) or Immune Checkpoint Blockade (ICB) now can lead to promising and durable remissions (Jun & Sadelain 2018, Wei et al 2018). While many methods for cancer immunotherapy are under study that include a variety of cell mechanisms and targets, a common approach in ACT and ICB is to engage or remove inhibition of T cells to eliminate target cancer cells. Despite early successes, however, immunotherapy has not been sufficiently effective across cancer types or for all patients, as the majority of patients fail to respond and strategies to improve immunotherapy outcomes are needed. The basic biology of T cells and how T cells interact with and are suppressed by the tumor microenvironment may contribute to these failures of ACT and ICB. In each case, cellular metabolism offers an avenue to understand the limitations of immunotherapy and may provide rational approaches to improve anti-tumor T cell activity by improving the metabolic fitness of anti-tumor T cells.

An essential component of an anti-tumor T cell response is antigen-driven T cell activation. In ACT, transferred cancer-specific T cells or T cells expressing a Chimeric Antigen Receptor (CAR) are stimulated upon interaction with target cells, while ICB blocks inhibitory signals that prevent the activation of endogenous anti-cancer T cells. In each case, antigen and co-stimulatory signals must be present for optimal activation, proliferation, and effector function. These co-stimulatory signals are provided in culture for *in vitro* expansion and as integral components of CARs in ACT and co-stimulatory signals are the direct targets for ICB, as PD-1 and CTLA4 are both inhibitory receptors of the CD28 co-stimulatory family of receptors (Schildberg et al 2016, Esensten et al 2016). A key function of co-stimulatory signals is to enhance T cell metabolism to support energetic requirements, biosynthesis, and cell signaling

processes for effector activities. CD28 promotes T cell nutrient uptake, glycolysis, and mitochondrial fitness (Frauwirth et al 2002, Geltink et al 2017), while PD-1 and CTLA4 each can suppress this pathway to instead reprogram T cell metabolism away from anabolic and effector pathways (Parry et al 2005). These challenges, however, also offer opportunities to improve ACT and ICB. How these metabolic changes influence T cell-based immunotherapy and how the tumor microenvironment may further suppress the metabolism of T cells is reviewed below.

T cell metabolism in CAR T cells and other ACT

ACT includes a variety of treatments in which immune cells are infused into patients to eliminate cancer cells. These approaches include the transfer of multiple different cell types that can be stimulated, differentiated, and engineered *ex vivo*. T cells have represented the major application for ACT and can include expanded tumor-infiltrating lymphocytes (TILs), engineered T cells modified to express TCRs specific for tumor-specific antigen peptide/MHC complexes, or antibody-based Chimeric Antigen Receptors (CARs) specific for cell surface tumor antigens. There are numerous advantages and disadvantages to different ACT strategies, which are reviewed elsewhere (Rosenberg & Restifo 2015). ACT has had promising success in some tumor types, particularly with CD19-specific CAR T cells used against B cell acute lymphoblastic leukemia (B-ALL) and B cell lymphomas, where up to half or more of patients can achieve durable remission (Maude et al 2018). Responses in other settings, however, remain poor. To improve and broaden these responses, T cell metabolism must be optimized to best support both robust initial and durable T cell responses for the specific activation stimuli, target cell, and tumor microenvironment.

Engineered CAR T cells offer a particularly promising approach to modulate T cell metabolism. By building specific signaling domains and properties into CARs, adoptively transferred T cells might be tailored for effector activity or long-lasting memory. Although many variations are being rapidly generated, the two FDA-approved CARs consist of an extracellular domain to target the B cell marker CD19 that is coupled with an intracellular portion that includes signaling domains from CD3ζ and the co-stimulatory molecules CD28 or 4-1BB. By linking TCR signaling directly with co-stimulatory signaling domains, CARs can be activated to elicit effector functions without additional need for inflammatory or co-stimulatory cues. Downstream signaling through CD28 or 4-1BB domains are thought to mediate the primary differences between the two CAR T cell treatments. Indeed, each signaling domain can elicit different metabolic effects (Kawalekar et al 2016). CAR T cells that express the CD28 signaling domain CAR can have increased glycolysis and effector responses but can be short-lived. Conversely, CAR T cells that express the 4-1BB signaling domain CAR have increased mitochondrial respiration and lipid oxidation and can be longer-lived, associated with a more central memory immunophenotype. These phenotypes are not surprising given the normal physiological functions of these co-stimulatory molecules. CD28 co-stimulation normally promotes glycolysis and effector differentiation through activation of the PI3K/Akt/mTORC1 pathway and regulation of mitochondrial morphology and function (Frauwirth et al 2002, Geltink et al 2017, Buck et al 2016) while 4-1BB may instead activate AMPK and stimulate lipid oxidation and mitochondrial biogenesis and metabolism (Choi et al 2017). 4-1BB also stimulates non-canonical NF-κB signaling to promote cell survival (Philipson et al 2020). These metabolic phenotypes of CD28 and 4-1BB CARs are reminiscent of short-lived effector T cells and long-lived memory T cells, respectively. Given this and detailed understanding of the mechanisms of CD28 and 4-1BB

signaling, a promising approach to increase CAR T cell effector function or survival has been to introduce signaling mutations. Mutation of the YMNM signaling motif of CD28, for example, was recently shown to increase CAR T cell survival and reduce signs of T cell exhaustion to enhance durable tumor control in pre-clinical models (Guedan et al 2020). The metabolic implications of this mutation are unclear, but Akt phosphorylation was maintained while MAPK and calcium signaling were reduced suggesting a shift in metabolic and mitochondrial regulation.

Other costimulatory molecules modulate T cell metabolism and may be incorporated into CAR constructs or targeted with agonist antibodies. ICOS, a member of the CD28 family, similarly promotes glycolysis and mTORC1 activity in Tfh cells (Zeng et al 2016). GITR agonism increases CD8 TIL metabolism (Sabharwal et al 2018). OX40 was expressed more highly in Treg TIL than CD4 Tconv TIL and was associated with enrichment of glycolysis and lipid metabolism transcripts. Agonism of OX40 enhanced lipid uptake in these Treg (Pacella et al 2018).

In addition to CAR, T cells harvested from tumors and *in vitro* expanded or transduced with engineered TCR can also be subject to metabolic manipulations to optimize function. These approaches are generally directed towards solid tumors and take advantage of natural or synthetically derived specificity against tumors and have both advantages and challenges. While tumor specific, T cells obtained from patient tumors are likely already epigenetically programmed and any metabolic manipulation will need to overcome this barrier. Engineered TCR can start from a naïve T cells similar to CAR but must differentiate to gain sufficient effector functions and longevity to eliminate tumors similar to CAR. The *in vitro* stimulation

period for each does offer, however, the opportunity to adapt nutrient conditions or T cell metabolism to favor appropriate effort and longevity states. In particular, T cells with low rates of glycolysis or mitochondrial potential may be generated or selected to have greater longevity while retaining effector functions (Kishton et al 2017). Similarly, targeting other pathways, such as glutamine metabolism may also promote increased T cell function in these settings (Leone et al 2019).

A significant advantage ACT has over ICB in metabolic approaches to immunotherapy is that treatments can be carried out during the *in vitro* stimulation and T cell engineering period rather than *in situ*. This approach allows the opportunity to modify T cell metabolism and mitochondria independent of effects on other cells and tissues and thus prevents any potential benefit of a metabolic therapy meant to boost T cells from also promoting the metabolism of cancer cells. This approach also eliminates concern for potential toxic side-effects of targeting metabolism in other tissues. The benefit, however, is predicated on the capacity of transient metabolic modifications during an *in vitro* period to lead to lasting effects on T cell differentiation, function, and fate *in vivo* to allow tumor elimination. This cell intrinsic stability is inherent in genetically engineered T cells, but it is also now clear that transient pharmacologic approaches may shift T cell metabolism to favor long-lived anti-cancer effector T cells for ACT.

One metabolic strategy that has proven promising to modify T cell differentiation is to selectively target the high rates of glycolysis that accompany effector T cells and that can impair the establishment of long-lasting memory. Glycolysis can be targeted directly with pharmacologic inhibitors, such as 2-deoxyglucose. This treatment of T cells stimulated *in vitro*

prior to ACT in preclinical models reduced glycolysis and proliferation, but also led to a more memory-like phenotype and greater cell survival *in vivo* (Sukumar et al 2013). As a result, 2-deoxyglucose treated T cells were better able to control tumors and extend animal life. Restricted glucose during T cell activation can also prime subsequent glucose uptake and shunting into the pentose phosphate pathway for nucleotide synthesis and altered redox balance, resulting in superior tumor control (Geltink et al 2020). The PI3K/Akt/mTORC1 pathway is a critical mechanism by which T cells induce aerobic glycolysis downstream of CD28 co-stimulation and, similar to 2-deoxyglucose, inhibition of Akt reduced glucose uptake and glycolysis and led to a more central memory phenotype. Importantly, this also improved the ability of *in vitro* inhibitor-treated CAR T cells to eliminate B cell leukemia following *in vivo* transfer (Klebanoff et al 2017).

Glutamine metabolism is generally coupled to aerobic glycolysis to provide anaplerotic substrates to maintain the TCA cycle. In CD4 Th1 and CD8 CTL, however, glucose and glutamine metabolism can become uncoupled and inhibition of glutamine metabolism can lead to an adaptive increase in glycolysis that drives T cell proliferation and effector differentiation (Johnson et al 2018, Leone et al 2019). Both GLS and broader glutamine metabolism inhibitors, therefore, can enhance the functionality of CD4 Th1 and CD8 CTL cells. In a CAR T cell model, this led to increased proliferation, ability to kill target cells, and rapid cell accumulation *in vivo*. A potential challenge to this approach to modulate glucose metabolism by targeting glutamine is that enhanced effector differentiation may be self-limiting. Similar to the fate of normal effector T cells, GLS-deficient T cells also induced inhibitory receptors and markers of terminal differentiation over time. Ultimately, permanent genetic loss of GLS led to a sharp loss

of cytotoxic function and B cell targets eventually accumulated to normal numbers (Johnson et al 2018). Nevertheless, transient *in vitro* inhibition was sufficient to induce epigenetic alterations that led to long-lasting changes in tumor-specific T cells and timed or transient inhibition of glutamine metabolism may provide a means to promote effector function while not driving T cells to exhaustion or terminal fates. Inhibition of glutamine metabolism may also be promising to reinvigorate TIL *in situ*, as tumor CD8 T cells upregulated acetate metabolism to support anabolism (Qiu et al 2019, Balmer et al 2020), in contrast to cancer cells which did not alter acetate metabolism and became catabolic.

Ultimately, memory or stem-like phenotypes are characterized by mitochondrial oxidative metabolism and strategies to mimic this state may best support long-term T cell survival and ability to eliminate cancer targets in ACT. This may be a key mechanism by which 4-1BB domain containing CARs support ACT (Kawalekar et al 2016) and approaches to directly modify mitochondria may also prove valuable. The morphology of mitochondria can play a key role in electron transport efficiency. Upon T cell activation mitochondria fragment and cristae remodel leading to reduced oxidative phosphorylation (Buck et al 2016). Transient inhibition of this fragmentation during activation, however, resulted in fused mitochondria that maintained mitochondrial oxygen consumption and supported long-term T cell survival and memory. Importantly, this treatment increased the ability of T cells to survive and eliminate tumors upon subsequent adoptive transfer (Buck et al 2016). CRISPR based gene knockout screens are a powerful tool to assess the role of metabolic genes in T cells in different contexts of inflammation and immunity. REGNASE 1 was discovered using this approach as a negative regulator of BATF, mediating mitochondrial function and morphology (Wei et al 2019). Another

strategy to rewire mitochondria in ACT is to directly promote mitochondrial lipid metabolism characteristic of memory T cells. Expression of the transcriptional co-activator PGC1α or treatment with the PPAR agonists bezofibrate or fenofibrate both increased lipid oxidation and increased T cell functionality and ability to eliminate tumors in ACT (Scharping et al 2016, Zhang et al 2017, Chowdhury et al 2018).

T Cell Metabolism in Immune Checkpoint Blockade

A fundamental difference between ACT and ICB is that while the challenge in ACT is to direct immunity against tumors using cells delivered as a pharmaceutical, the goal of ICB is to overcome inhibitory signals to activate endogenous anti-tumor specific T cells. ICB also is most commonly directed against solid tumors, where the tumor microenvironment can exert a strong influence on T cell metabolism. Beyond the initial barrier that T cells must first infiltrate into tumors, ICB must surmount several key challenges. Tumor infiltrating T lymphocytes (TIL) may have an exhausted differentiation state, with high expression of inhibitory receptors and altered epigenetic marks that impede effector function (Philip et al 2017). These changes are accompanied by diverse metabolic adaptations that lead to multiple deficits. Translocation of GLUT1 to the cell surface to support glucose uptake can be impaired and glycolytic enzymes GAPDH and Enolase can be downregulated or suppressed (Siska et al 2017, Gemta et al 2019). Mitochondria can also be dysregulated, with fragmented morphology, high production of reactive oxygen species, and poor capacity for respiration (Siska et al 2017, Scharping et al 2016). Rescue of TIL metabolism, however, with expression of PCK to promote gluconeogenesis and the replacement intracellular glycolytic intermediates or by treatment with pyruvate or acetate to directly support mitochondrial metabolism can improve T cell

inflammatory function (Siska et al 2017, Qiu et al 2019, Ho et al 2015). These findings demonstrate that the lack of metabolic flux directly contributes to T cell impairments in the TME.

One mechanism by which ICB may act to restore T cell function is to enhance T cell metabolic capacity to rescue T cells from metabolic defects imposed by the TME. Another is to promote differentiation of PD1+ TCF1+ stem-like progenitor exhausted T cells into effector T cells, which may occur in secondary lymphoid tissue, tertiary lymphoid structures, or in the tumor itself (Siddiqui et al 2019, Miller et al 2019). In either context, disrupting coinhibitory signals promotes the generation of effector cells. In addition to chronic TCR signaling, the TME can express high levels of immunosuppressive ligands, including PD-L1 or PD-L2. A normal function of both PD-1 and CTLA4 is to suppress PI3K and Akt signaling and thus oppose a key signaling mechanism of CD28-family mediated co-stimulation (Schildberg et al 2016). PD-1 can recruit SHP1/2 phosphatase to prevent PI3K activation, while CTLA4 can inhibit both the interaction of CD28 with the ligands B7-1 and B7-2 as well as recruit the phosphatase PP2a. It is not surprising, therefore, that PD-1 and CTLA4 inhibit CD28-mediated metabolic reprogramming and the induction of aerobic glycolysis that otherwise characterizes effector T cells (Frauwirth et al 2002, Parry et al 2005).

Distinguishing PD-1 and CTLA4, CTLA4 is thought to be more important for initial phases of T cell activation and thereby promote a naïve metabolic program. PD-1, in contrast, is expressed after TCR engagement. PD-1 signals restrain glucose uptake and glycolysis in T cell activation and instead promote lipid oxidation that is characteristic of long-lived quiescent cells.

Intriguingly, both anti-CTLA4 and anti-PD-1 can promote the expansion of new anti-tumor clones. Overall, inhibitory signals can prevent inappropriate T cell activation or excessive inflammation. In support of this model, stimulated PD-1-deficient T cells can maintain greater metabolic activity in chronic infection models (Bengsch et al 2016, Patsoukis et al 2015). By blocking the PD-1 and CTLA4 mediated physiologic signals that dampen effector T cell metabolism ICB can allow T cell stimulation and increased metabolism. ICB treatments that inhibit ligand interactions of PD-1 or CTLA4, therefore, relieve inhibition of PI3K/Akt/mTORC1 signaling to allow T cells to adopt an effector-like metabolism. In addition, as a metabolic shift may lead to epigenetic modifications, successful ICB may metabolically reprogram epigenetic marks to favor effector functions or cell longevity, although these changes remain to be fully understood.

In addition to PD-1 and CTLA4 that have been most extensively pursued as targets for ICB, other coinhibitory molecules also modulate T cell metabolism. Indeed, of the various ICB targets that provide or inhibit co-stimulatory signals to T cells, many have been shown to also influence cell metabolism and this may be a general mechanism by which co-stimulation promotes or suppresses T cell function. TIM3 negatively regulates glycolysis and GLUT1 expression, and may also inhibit glutaminolysis (Lee et al 2020). LAG3 negatively regulates mitochondrial metabolism (Previte et al 2019). Likewise, targeting 4-1BB and OX40 may enhance T cell mitochondrial metabolism to promote effector function and long-term survival (Choi et al 2017, Tsurutani et al 2016). Each of these metabolic regulatory functions may both directly affect biosynthetic processes and influence epigenetic marks for long-lasting influence over T cell differentiation and fate. Other family members and how these various T cell modulating

receptors may ultimately impact anti-tumor T cell metabolism and functions, however, remains to be established.

Regardless of the presence and function of co-stimulatory or inhibitory molecules, T cells in the TME must still access adequate essential nutrients to support metabolic demands. Various nutrients, however, may be limited or heterogeneous in abundance. In addition to limited oxygen in regions of hypoxia, glucose and other nutrients essential for efficient effector T cell responses may be depleted in the TME (Ho et al 2015, Chang et al 2015). Because cancer cells themselves can use an aerobic glycolysis metabolism that is similar to activated effector T cells and therefore can have similar metabolic requirements (Andrejeva & Rathmell 2017), competition may arise for these nutrients in settings where vascular exchange is limited. This potential for nutrient competition suggests that the metabolism of the TME itself may be directly immunosuppressive. Indeed, changes in tumor glucose metabolism can influence the ability of T cells to eliminate tumors and increased tumor cell glycolysis can reduce anti-tumor immunity (Chang et al 2015). The generality of such nutrient competition is uncertain, however, as measurements of metabolites in tumor interstitial fluid in some tumor settings have found that glucose and glutamine can be at normal or at only modestly decreased levels (Siska et al 2017, Sullivan et al 2019). Nevertheless, T cells from these same tumors show metabolic impairments (Siska et al 2017), suggesting that chronic antigen stimulation and immune inhibitory receptors, such as PD-1, contribute and may be the primary drive for many of these metabolic phenotypes. An unresolved question relevant to potential metabolic competition and tumors is to what extent T cells in the TME may be capable of reactivation with ICB or do ICB therapies instead engage T cells that have yet to experience prolonged engagement with tumors and tumor antigens. This

is an important question that will influence understanding of the metabolic implications of the TME on T cells as, despite these many barriers, ICB does successfully eliminate many tumors.

Macrophage Metabolism

The overall theme that glycolysis promotes inflammation and oxidative metabolism promotes immune resolution appears to hold true generally across immune cell types, not just in T cells. Macrophage activation offers an extreme example of distinct glycolytic and oxidative cellular metabolic programs linked to function. Macrophage activation by cytokines and toll-like receptor (TLR) signaling causes increased phagocytosis and secretion of cytokines. However, the specific activation signals *in vitro* cause stark changes metabolically. Activation with TLR4 agonist lipopolysaccharide (LPS) and/or IFNγ induces pro-inflammatory M1 polarization with and a glycolytic phenotype. Alternative activation with IL4 induces anti-inflammatory or pro-resolution M2 polarization and an oxidative phenotype (Rodriquez-Prados et al 2010). Increased glycolysis in M1 macrophages is partly due to induction of pyruvate kinase isoenzyme M2 (PKM2), which in addition to functioning in glycolysis also translocates to the nucleus to promote HIF1α activity and IL1β production (Palsson-McDermott 2015). The M1 versus M2 paradigm is supported by massive changes in TCA cycle metabolism. M1 macrophages have a "broken" TCA cycle with no flux through isocitrate dehydrogenase (IDH) and succinate dehydrogenase (Jha et al 2015, O'Neill 2015). Instead, glutamine and α-ketoglutarate are shunted toward succinate production which further promotes HIF1α activity and IL1β production (Tannahill 2013), and the arginosuccinate shunt promotes the production of citrate for fatty acid synthesis and the production of antimicrobial itaconate (Michelucci et al 2013). M2 macrophages

still use glucose, however, and utilize key anabolic signaling complexes mTORC1 and mTORC2 (Covarrubias et al 2016, Huang et al 2016).

While it is thought that the differences in M1 and M2 macrophages stem from M1 cells' higher demand for energy in the short term, there are limitations to the M1 versus M2 paradigm *in vivo* (Ganeshan & Chawla 2014). The paradigm has relied heavily on in vitro experiments with bone marrow-derived macrophages. Much remains uncharacterized *in vivo* macrophages, where more complicated cytokine signaling and nutrient microenvironments may yield distinct phenotypes (Bakker & Pearce 2020). The TME is one such environment where macrophages are often highly abundant and interact with T cells and cancer cells. Tumor macrophages can be highly abundant and have substantial consequences in the TME through secretion of cytokines rewiring the metabolism of other cells as well as secretion of immunosuppressive metabolites such as kynurenine (Vitale et al 2019).

Glucose Metabolism in the Tumor Microenvironment

The original finding of tumor metabolism was published nearly a century ago by Otto Warburg (Warburg et al 1924). He observed that glucose was metabolized to lactate in thin slices of Flexner-Jobling tumors serially passaged in rats, and the cellular respiration of cancer cells was severely reduced compared to normal tissues even though there was oxygen available. No *ex vivo* media conditions could rescue the reduced respiration of cancer cells. The result was so profound that Warburg later hypothesized that a defect in cellular respiration was the ultimate etiology of all cancers (Warburg 1956). Warburg's hypothesis on the origin of cancer did not hold up, and now we appreciate that cancer arises from genetic mutations However, the

preferential conversion of glucose into lactate in the presence of oxygen became known as the Warburg Effect or aerobic glycolysis. It became the most studied aspect of tumor metabolism, although therapies targeting aerobic glycolysis have had limited success (Vander Heiden & DeBerardinis 2017). Glutamine metabolism in cells exhibiting aerobic glycolysis, in addition to being an important source of carbon and nitrogen, supports anabolism through anaplerosis, demonstrating that focusing on glucose is insufficient (DeBerardinis et al 2007). Additionally, tumors can have a variety of metabolic programs and demonstrate metabolic flexibility according to their location and in response to treatment (Senyilmaz & Teleman 2015). A caveat to this approach is that the tumor slices used by Warburg were not pure cancer cells and likely included a range of tumor infiltrating cells.

With respect to the TME, the paradigm of cancer cell aerobic glycolysis led to the hypothesis that cancer cells outcompete anti-tumor immune cells for glucose. In this model, glucose is a scarce resource required by anti-tumor immune cells and its depletion is a form of immunosuppression. Glycolytic metabolism between cancer cells and CD8 T cells was inverted regressor and progressor tumor models, with progressing tumors having high cancer cell metabolism and low CD8 T cell metabolism. Overexpression of genes promoting glycolysis in cancer cells enhanced tumor growth and reduced *in vivo* fluorescent glucose analog 2NBDG uptake in CD8 TIL, suggesting that cancer cells were preventing glucose uptake in TIL (Chang et al 2015). Additionally, overexpression of phosphoenolpyruvate carboxykinase 1 (PCK1) to increase flux in late glycolysis in tumor-specific CD4 T cells improved TIL function and reduced tumor burden in a mouse model of melanoma with low interstitial glucose concentration (Ho et al 2015). These data strongly suggest that glycolytic machinery promotes the function of cancer cells and T cells in the TME, however the more specific hypothesis of competition for glucose

remains difficult to conclude. These experimental manipulations may have caused many other intrinsic (such as intrinsic metabolic program) and extrinsic (such as composition of other tumor cells) changes to the microenvironment which would explain differences in glucose metabolism. Additionally, analyses of metabolites in human and mouse tumor interstitial fluid demonstrate that, at steady state, glucose is present in the TME (Siska et al 2017, Sullivan et al 2019, Cortese et al 2020). These data would suggest that in many tumors glucose is present and may be preferentially consumed by different cells not due to competition for nutrients, but rather due to the intrinsic uptake capacity of each cell. Heterogeneity between patients, between tumor sites, and between local microenvironments within a given tumor may dictate the availability of glucose and other nutrients to particular cell subsets, but the Warburg effect does not mean low glucose availability in tumors generally.

The consequences of enhanced tumor glycolysis may be less about glucose and more about lactate. The Warburg effect also predicts high lactate in the TME compared to normal tissue. Lactate is elevated in tumor interstitial fluid (Cortese et al 2020). High lactate in the TME reduces antitumor activity of T cell and NK cells (Brand et al 2016). Anti-inflammatory Treg have greater capacity to survive in high lactate environments and use lactate as an oxidative fuel (Angelin et al 2017, Watson et al 2021). Lactate also promotes M2-like immunosuppressive tumor-associated macrophage (TAM) phenotype (Colegio et al 2014, Noe et al 2021).

Outstanding Questions and Rationale for Dissertation Research

A better understanding of metabolism in the TME and in distinct cell subsets may be crucial to improving patient outcomes in cancer. Optimizing T cell metabolism is a promising avenue of synergy with cancer immunotherapy. Normal T cell metabolic physiology can identify key

transition and regulatory points that are altered in cancer and provide opportunities in ACT and ICB cancer immunotherapies. Metabolism underlies all cellular functions and may provide approaches to increase stemness and long-term memory, enhance effector function, and reduce exhaustion in T cells through diverse mechanisms. Organism-level metabolism is another important avenue of investigation, as obesity causes dysfunctional TIL partly through differential responses to lipids (Ringel et al 2020). The paradigm of T cell stemness, supported by mitochondrial oxidative phosphorylation, has proven advantageous for ACT, whereas reversing any component of the global metabolic dysfunction of exhausted T cells in the tumor microenvironment may be a viable strategy. Interrogation of T cell metabolism alone is insufficient for studying immunotherapy, as differences between T cell and cancer cell metabolism may highlight new approaches to specifically target tumor cell subsets. It is important for future therapeutics targeting tumor metabolism to address their effect on cancer cells, T cells, macrophages, and other tumor and immune cell subsets.

Several questions have come to the forefront for the field of tumor and T cell metabolism. The distinct microenvironments of tumor specific T cells, either in the TME or in lymphoid tissue, does not adequately explain how ICB exerts activity despite potentially metabolic constraints in tumors. Terminal differentiation and T cell dysfunction is intimately tied to epigenetic alterations. It remains an ongoing question if "terminal" differentiation and its' associated epigenetics can be reversed, and whether cellular metabolism may be the lynchpin underlying effector function rescue. It also remains largely untested and uncertain which nutrients are actually available for T cells and other immune cells in the tumor microenvironment that may support cell functions and these epigenetic regulations. In this sense, our understanding of the

tumor microenvironment is rudimentary at best and a systems biology and spatial view will be essential. A fundamental question in immunotherapy for both ACT and ICB is what target is best suited to what indication? Ultimately, this will depend on gaining a better understanding of how each co-stimulatory or inhibitor molecule affects T cell physiology and gene expression and placing this in the context of the specific tumor setting and microenvironment, including available nutrients and heterogeneity of stromal, cancer, and other immune cells. As is the case for all exciting areas of research, one question begets many more as the field continues to advance and improve cancer therapy.

Fundamentally important to immunometabolism *in vivo* is the question of which nutrients are available and utilized by diverse cell types in specific tissues. Additionally, if there are differences in nutrient utilization, why do they exist? In Chapter 2 of this dissertation, we demonstrate the cancer cells do not dominate tumor glucose uptake but do dominate glutamine uptake. Glucose is most avidly up taken by myeloid cells including macrophages, and T cells do not appear to be "starved". We also suggest that, instead of competing for scarce metabolites, uptake of nutrients is governed by cell intrinsic cell programming. We expand on these nutrient uptake findings in Chapter 3.

Before utilizing treatments targeting tumor metabolism, it may be wise to ascertain the effect of therapies on distinct compartments of the TME. In Chapter 4, we ask if different strategies of glutamine inhibition could lead to differential outcomes. We find that global glutamine blockade early during T cell activation has a detrimental effect on anti-tumor function and sets CD8 T cells on a distinct differential trajectory compared to a more specific glutamine-targeting strategy

inhibiting only glutaminase. Taken together, this dissertation demonstrates the contributions of distinct cell subsets to the TME and the importance of examining cell-specific and therapy-specific contributions to TME cellular fate and function.

CHAPTER 2: CELL-PROGRAMMED NUTRIENT PARTITIONING IN THE TUMOR MICROENVIRONMENT

This chapter was adapted from the following manuscript published in *Nature*:

Reinfeld, B. I., Madden, M. Z., Wolf, M. M., Chytil, A., Bader, J. E., Patterson, A. R., ... & Rathmell, W. K. (2021). Cell-programmed nutrient partitioning in the tumour microenvironment. Nature, 593(7858), 282-288.

Introduction

Cancer cells characteristically consume glucose through Warburg metabolism (Vander Heiden & DeBerardinis 2017), a process forming the basis of tumor imaging by positron emission tomography (PET). Tumor infiltrating immune cells also rely on glucose, and impaired immune cell metabolism in the tumor microenvironment (TME) contributes to tumor immunological evasion (Siska et al 2017; Ho et al 2015; Chang et al 2015). It remains uncertain, however, if immune cell metabolism is dysregulated in the TME by cell intrinsic programs or by competition with cancer cells for limiting nutrients. Here we used PET tracers to measure access and uptake of glucose and glutamine by specific cell subsets in the TME. Surprisingly, myeloid cells had the greatest capacity to uptake intra-tumoral glucose, followed by T cells and cancer cells across a range of cancer models. Cancer cells, in contrast, demonstrated the highest glutamine uptake. This distinct nutrient partitioning was cell intrinsically programmed through mTORC1 signaling and glucose and glutamine-related gene expression. Inhibiting glutamine uptake enhanced glucose uptake across tumor resident cell types, demonstrating that glutamine metabolism suppresses glucose uptake without glucose being limiting in the TME. Thus, cell intrinsic programs drive the preferential immune and cancer cell acquisition of glucose and glutamine, respectively. Cell

selective partitioning of these nutrients may be exploited to develop therapies and imaging strategies to enhance or monitor the metabolic programs and activities of specific cell populations in the TME.

The founding observation in cancer metabolism was that tumors consume glucose to produce lactate in the presence of oxygen. Aerobic glycolysis is widely observed in rapidly proliferating cells, including activated immune cells, to support biosynthetic demands (Vander Heiden & DeBerardinis 2017). *In vivo* carbon labeling studies have confirmed that glucose supports anabolic metabolism in transformed cells and T cells (Faubert et al 2017; Ma et al 2019). Glutamine metabolism provides anaplerotic fuel, and restrains glucose-dependent differentiation and function of macrophages and T cells (Liu et al 2017; Johnson et al 2018; Leone et al 2019). These metabolic pathways may become disrupted in immune cells in the TME to prevent anti-tumor immunity (Siska et al 2017; Ho et al 2015; Chang et al 2015; Scharping et al 2021).

Glucose uptake can be measured using [18F]fluorodeoxyglucose (FDG) positron emission tomography (PET) imaging to detect cancers and monitor therapeutic responses. Depletion of TME glucose by cancer cells may drive nutrient competition as a metabolic mechanism of immunosuppression (Ho et al 2015; Chang et al 2015). High micromolar to millimolar glucose concentration have been measured in mouse and human TME (Siska et al 2017; Sullivan et al 2019; Cortese et al 2020). Further, the metabolic phenotypes of T cells can persist even after removal from the TME and culture in nutrient-replete media, including after the specific addition of pyruvate suggesting dysfunctional glycolysis (Siska et al 2017; Gemta et al 2019). The extent of intrinsic metabolic programming or nutrient competition for limited nutrients between cancer

cells and immune cells remains uncertain. Here we used PET probes to directly measure glucose and glutamine uptake in TME cell subsets.

Nutrients partition in the tumor microenvironment

Immune cells may contribute significantly to glucose consumption in the TME. We measured nutrient abundance in the tissue interstitial fluid (IF) from freshly resected human renal cell carcinoma (RCC) specimens and subcutaneous murine MC38 tumors using mass spectrometry (**Figure 2.1a-b, Table 2.1**) (Nair-Gill et al 2010). Glucose, glutamine, and lactate were all detectable in the TME at similar concentrations to matched normal kidney tissue or plasma. *In vivo* glucose uptake was next directly measured to quantify the accessibility of glucose to distinct cell populations in the TME. Subcutaneous MC38 tumors were visualized by FDG-PET imaging and per cell *in vivo* ^{18}F radioactivity was measured in fractionated tumor cell subsets (**Figure 2.1c, d**). CD45 positive selection magnetic microbeads fractionated tumor cells into enriched $CD45^-$, predominantly cancer cell, and $CD45^+$ immune cell populations (**Figure 2.1e, Figure 2.2a**). Unfractionated tumor cells demonstrated higher FDG avidity than control tissue splenocytes (**Figure 2.1f**). Strikingly, tumor infiltrating $CD45^+$ immune cells had greater per cell FDG uptake than $CD45^-$ cells. FDG autoradiography and immunohistochemistry demonstrated homogenous distribution of FDG and $CD45^+$ cells, showing differential uptake was not due to spatial distribution favoring immune cells (**Figure 2.1g-h**). Immune cells also had higher FDG avidity in BALB/c syngeneic CT26 and Renca subcutaneous tumors (**Figure 2.1i-j, Figure 2.2b-c**) and orthotopic Renca tumors demonstrated higher per cell FDG avidity in immune cells (**Figure 2.1k, Figure 2.2d**). Infiltrating immune cells had higher FDG uptake than $EPCAM^+$ cancer cells in both azoxymethane/dextran sodium sulfate-induced (AOM/DSS) inflammatory colon cancer tumors

and PyMT genetically engineered mouse model (GEMM) breast cancer models (**Figure 2.1l-m, Figure 2.2e-g**). These results show that glucose is available in the TME and preferentially partitions into infiltrating immune cells more than cancer cells across multiple models.

Table 2.1: Human kidney cancer patient characteristics.

Patients 170-248 were used for TIF analysis, 295-345 were used for pS6 analysis; N/R= not reported

Number in dataset	Patient ID	Histo	Grade	Age	Sex	Race/Ethnicity	Size (cm)	Mechanism of Attainment
1	170	ccRCC	G3	66	F	White	N/R	Primary Nephrectomy at VUMC
2	192	ccRCC	G3	65	M	Black	5.4	Primary Nephrectomy at VUMC
6	213	ccRCC	G4	59	M	White	10	Primary Nephrectomy at VUMC
9	218	ccRCC	G3	56	M	Black	6	Primary Nephrectomy at VUMC
10	219	ccRCC	G1	33	F	White	5.6	Primary Nephrectomy at VUMC
11	220	ccRCC	G3	44	M	White	9	Primary Nephrectomy at VUMC
12	225	ccRCC	G3	79	F	White	7	Primary Nephrectomy at VUMC
14	227	ccRCC	G3	62	M	White	13	Primary Nephrectomy at VUMC
15	228	ccRCC	G3	67	M	Hispanic	8.5	Primary Nephrectomy at VUMC
16	229	ccRCC	G2	74	F	White	5	Primary Nephrectomy at VUMC
17	231	ccRCC	G2	62	M	White	3.5	Primary Nephrectomy at VUMC
18	234	ccRCC	G4	79	F	White	3.5	Primary Nephrectomy at VUMC
19	235	ccRCC	G2	45	M	White	12	Primary Nephrectomy at VUMC
20	247	ccRCC	G3	38	F	White	6	Primary Nephrectomy at VUMC
21	248	ccRCC	G2	66	F	White	7.6	Primary Nephrectomy at VUMC
1	295	ccRCC	G1	65	F	White	4	Primary Nephrectomy at VUMC
2	323	ccRCC	G4	84	M	White	8	Primary Nephrectomy at VUMC
3	333	ccRCC	G3	43	M	White	9.7	Primary Nephrectomy at VUMC
4	345	ccRCC	G2	45	M	White	14	Primary Nephrectomy at VUMC

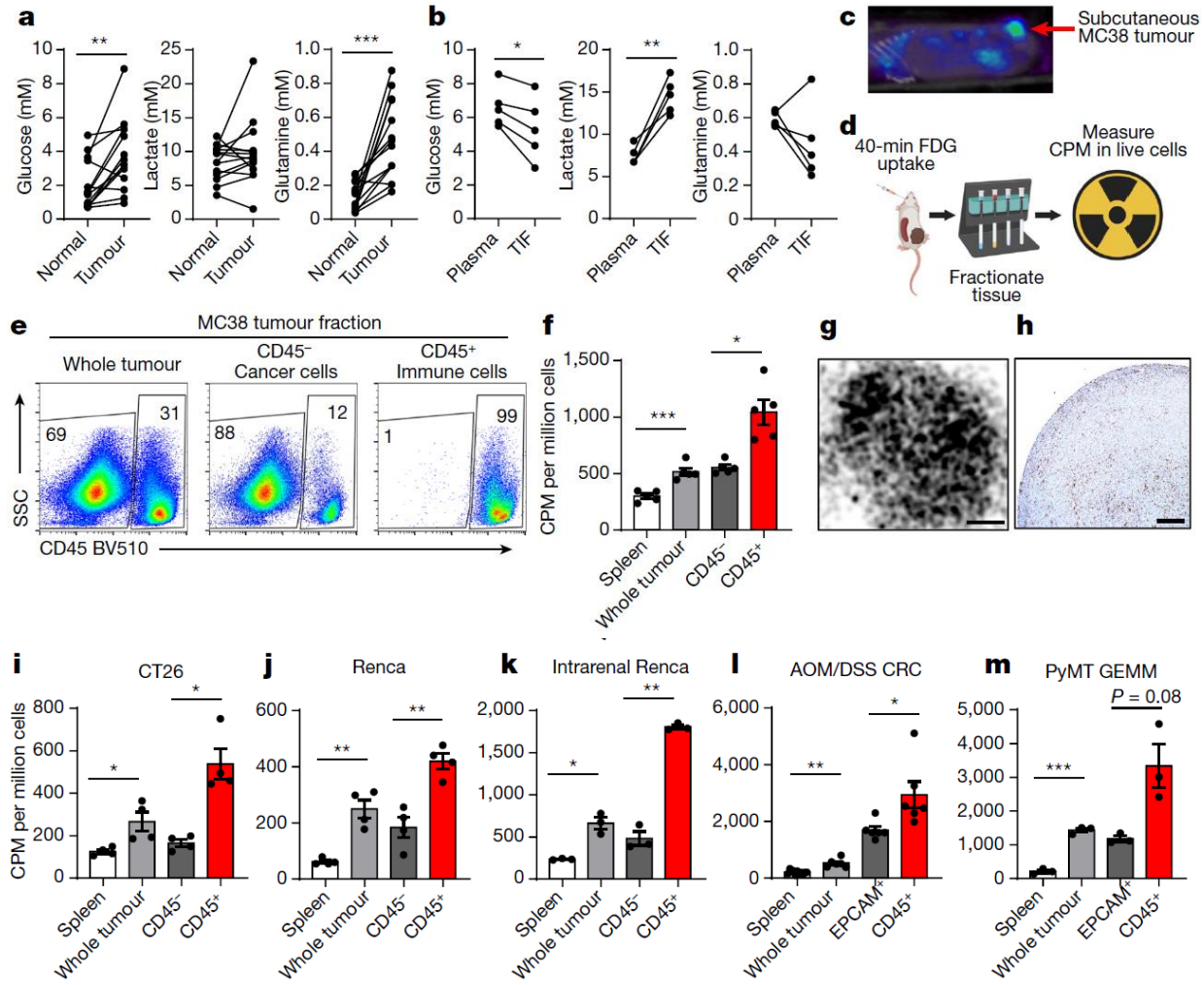

Figure 2.1: Glucose is preferentially consumed by immune cells over cancer cells. a,b Quantification of IF metabolites from (**a**) human ccRCC tumors and matched adjacent normal kidney (n=14 patients) and (**b**) murine MC38 subcutaneous tumor IF and matched plasma (n=5 mice). **c**, Representative (of n>20 mice) FDG PET image of MC38 tumor. **d**, Experimental schema. **e**, Representative flow cytometry analysis of MC38 whole tumor, $CD45^+$, and $CD45^-$ cell fractions gated on live cells. **f,** FDG avidity in designated cell fractions from MC38 tumors (n=5 mice). **g,** Representative (of n=3 mice) tissue autoradiography of MC38 tumor (scale bar = 800μm). **h,** Representative (of n=5 mice) IHC for CD45 in MC38 tumor (scale bar = 200μm). **i-m,** FDG avidity in designated tumor cell fractions from subcutaneous CT26 (n=4 mice) (**i**) and Renca (n=4 mice) (**j**) tumors; intrarenal Renca tumors (n=3 mice) (**k**); AOM/DSS-induced CRC tumors (n=6 for tumor, n=11 mice for spleen) **(l);** and PyMT GEMM tumors (n=3 mice) (**m**). Each data point represents a biological replicate and graphs show mean and SEM. (b-c, e-m) are data from representative studies performed independently at least twice. P values were calculated using paired 2-tailed t-test for (a-b) and Welch's 2-tailed t-test for (f, i-m). * $p<0.05$, ** $p<0.01$, *** $p<0.001$. AOM/DSS CRC: azoxymethane/dextran sodium sulfate-induced colorectal cancer; ccRCC: clear cell renal cell carcinoma; CPM: counts per minute; FDG PET: 18-fluorodeoxyglucose positron emission tomography; GEMM: genetically engineered mouse model; IF: interstitial fluid; PyMT: Polyoma virus middle T antigen; TIF: tumor interstitial fluid; TME: tumor microenvironment

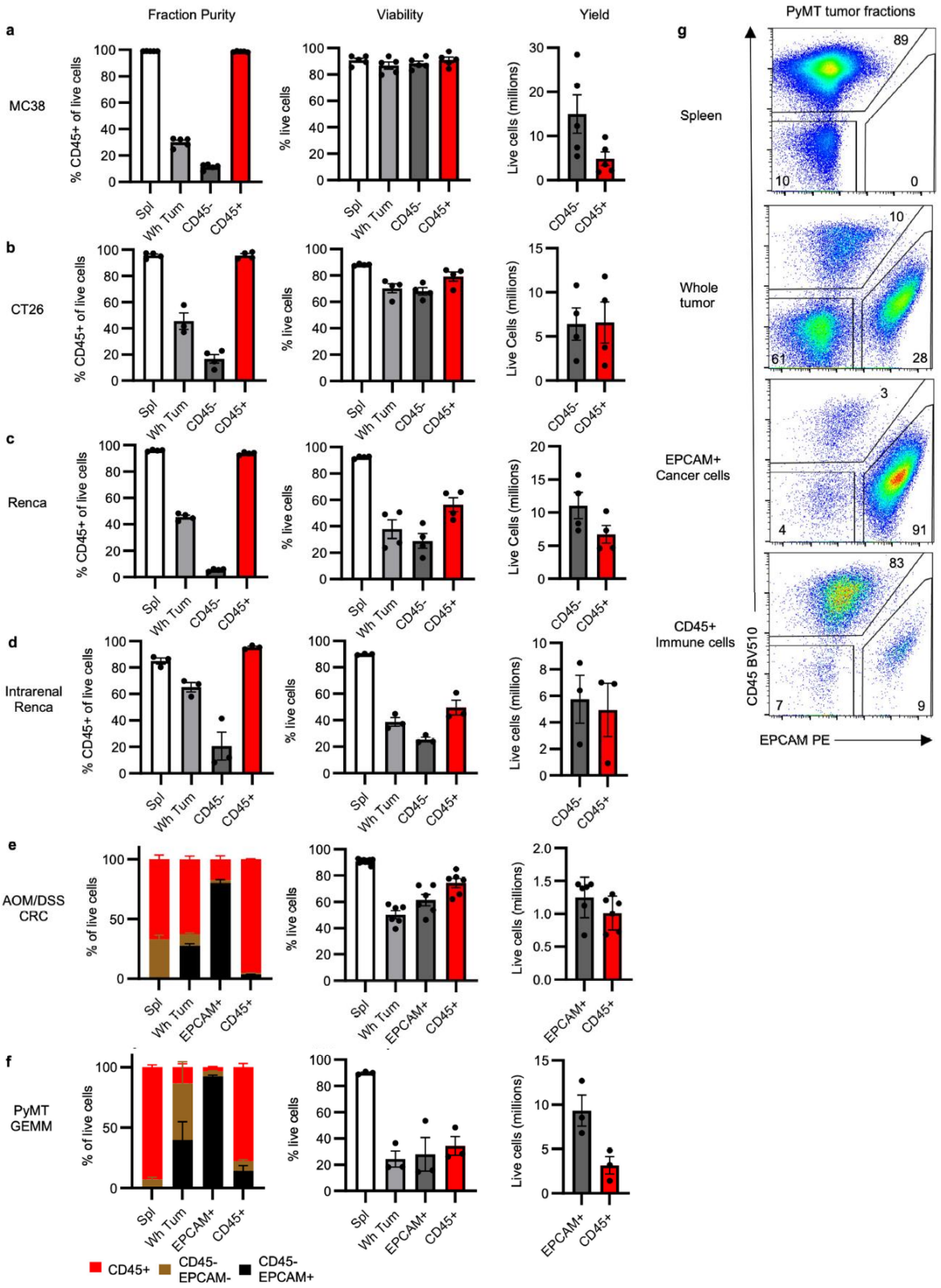

Figure 2.2: Purity, viability, and yield of isolated tumor cell populations. a-f, Fraction purity, viability, and yield for (**a**) MC38 (n=5 mice), (**b**) CT26 (n=4 mice), and (**c**) Renca (n=4 mice) subcutaneous tumors; (**d**) intrarenal Renca tumors (n=3 mice); (**e**) AOM/DSS-induced CRC

tumors (n=6 for tumors, n=11 mice for spleens); and (**f**) spontaneous PyMT GEMM (n=3 mice) tumors. **g**, Representative flow cytometry analysis of PyMT and AOM/DSS CRC whole tumor, $CD45^+$ immune cell, and $EPCAM^+$ cancer cell fractions gated on live cells. Each data point represents a biological replicate and graphs show mean and SEM. Data are representative studies performed independently at least twice. AOM/DSS CRC: azoxymethane/dextran sodium sulfate-induced colorectal cancer; GEMM: genetically engineered mouse model; PyMT: polyoma virus middle T antigen.

Multiple strategies validated that this approach accurately measures *in vivo* per cell glucose uptake. Immune cells isolated from MC38 tumors were confirmed as tumor-infiltrating based on minimal labeling following intravenous administration of fluorescent anti-CD45 antibody that efficiently labeled immune cells in blood and spleen (**Figure 2.3a**). FDG uptake had a dynamic range with a multiple-log scale of linearity (**Figure 2.3b**) and was independent of sample viability, cell yield, and tumor mass across biological replicates and tumor models (**Figure 2.3c**). To confirm that FDG uptake did not occur during tumor processing, unlabeled MC38 tumor single cell suspensions were incubated with supernatants from FDG-labeled tumors. *Ex vivo* FDG uptake did not substantially contribute to the final FDG signal (**Figure 2.3d-e**). Finally, to specifically examine cancer cells apart from other $CD45^-$ cells, $Thy1.1^+$ MC38 cells were implanted in $Thy1.1^-$ hosts and isolated using Thy1.1 positive selection microbeads. Negatively selected $Thy1.1^-$ immune cells demonstrated higher FDG avidity than $Thy1.1^+$ cancer cells (**Figure 2.3f-h**). This approach thus specifically and quantitatively measures *in vivo* glucose uptake of cancer and immune cells in the TME. We also tested the fluorescent glucose analog 2NBDG (N-(7-Nitrobenz-2-oxa-1,3-diazol-4-yl)Amino)-2-Deoxyglucose). Consistent with other *in vitro* findings (Sinclair et al 2020), 2NBDG was not specific for glucose uptake *in vivo* and comparative measures of radioactive FDG and 2NBDG uptake in T cells from mice co-injected with both tracers showed no correlation of FDG radioactivity with 2NBDG (**Figure 2.4, Figure 2.5**).

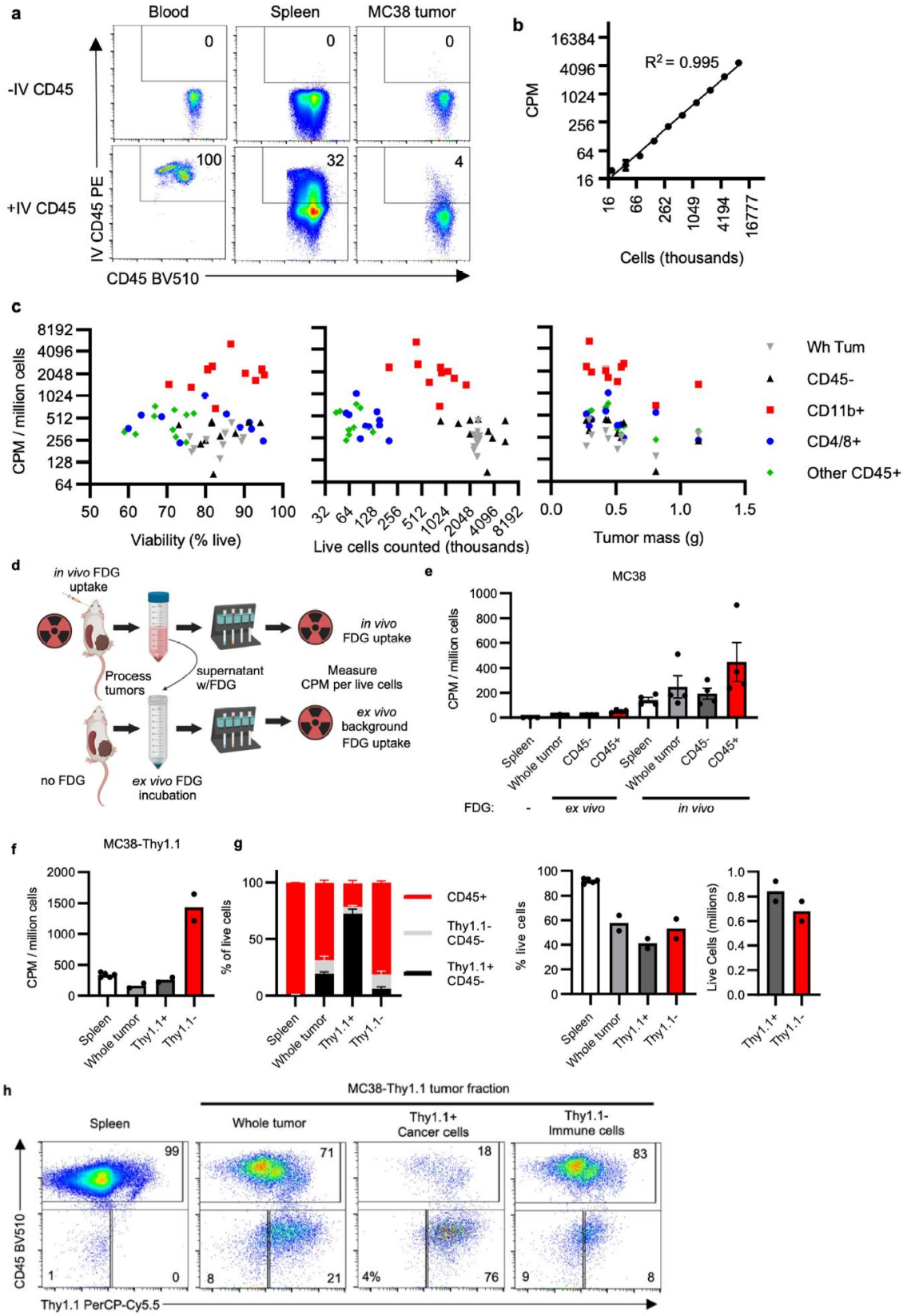

Figure 2.3: Validation of *in vivo* cellular FDG uptake assay. a, Intravenous (IV) anti-CD45 PE staining of leukocytes from designated tissues gated on live $CD45^+$ cells. **b**, Demonstration

of dynamic range of ^{18}F quantification using serially diluted *in vivo* FDG-labelled splenocytes. **c,** Correlation plots of CPM/live cell versus cell viability, cells counted, and tumor mass across multiple tumor cell populations. Only "CD45^{-}" and "Other CD45^{+}" simple linear regressions had slopes significantly different than 0 for tumor mass (n=10 mice). **d**, FDG-labelled digest supernatant from *in vivo* labelled MC38 tumors was applied to FDG-naïve MC38 tumor single cell suspensions to determine *ex vivo* background FDG uptake contribution to final signal. **e**, Cellular FDG avidity in designated *ex vivo* and *in vivo* labelled MC38 tumor cell populations (n=4 mice/group). **f**, Cellular FDG avidity in designated tumor cell fractions from MC38-Thy1.1 tumors (n=2 mice). **g**, Proportion of CD45^{+} and Thy1.1^{+} cells, cell viability, and live cell yield from MC38-Thy1.1 tumors (n=2 for tumors, n=5 mice for spleens). **h**, Representative flow cytometry analysis of MC38-Thy1.1 tumor fractions. Each data point represents a biological replicate and graphs show mean and SEM. (b, d-h) are data from a representative study performed independently at least twice. * p<0.05, ** p<0.01, *** p<0.001. CPM: counts per minute.

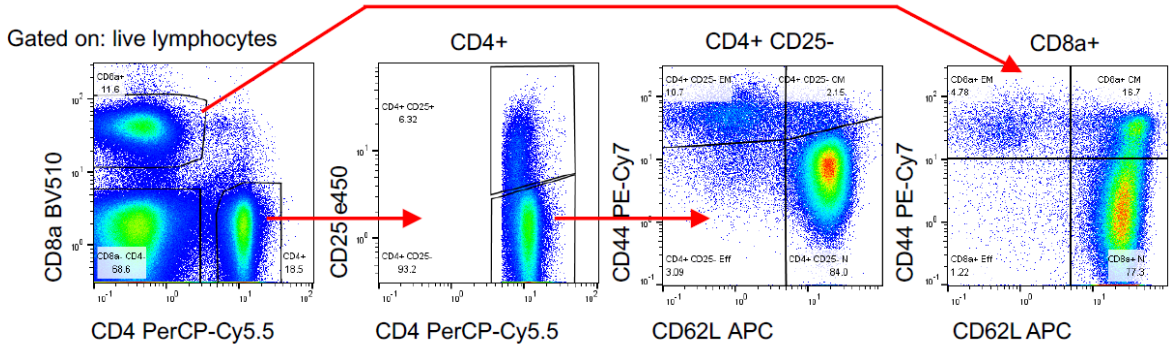

Figure 2.4: Flow cytometry gating scheme for *in vivo* 2NBDG T cell uptake.

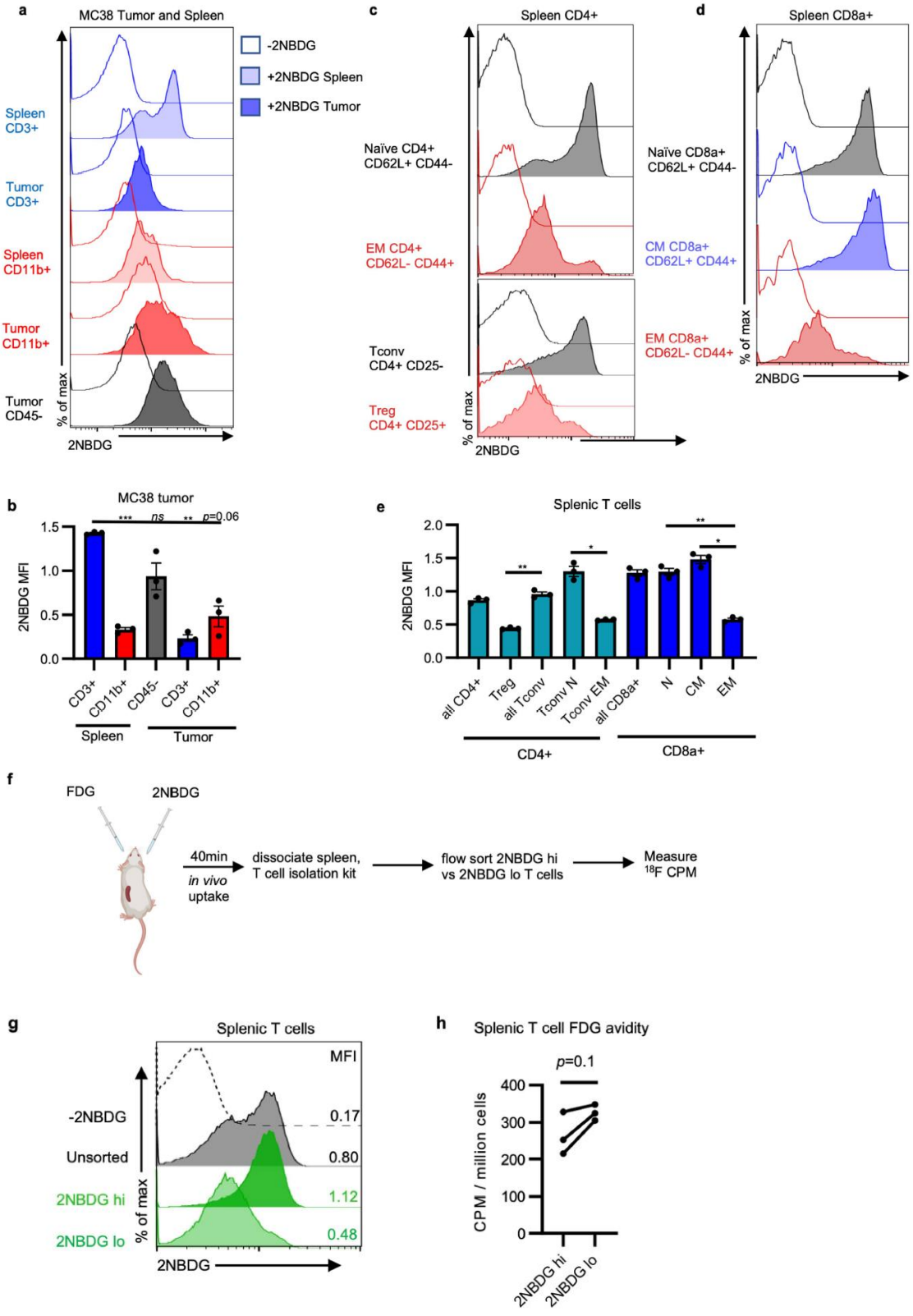

Figure 2.5: *In vivo* 2NBDG uptake does not mirror FDG uptake. **a,** Representative histograms of *in vivo* 2NBDG uptake in splenic and MC38 tumor cell subsets. **b,** MFI of *in vivo*

2NBDG uptake across spleen and MC38 tumor cells (n=3 mice). **c-d,** Representative histograms of *in vivo* splenic CD4 **(c)** and CD8 (**d**) T cell 2NBDG uptake. **e**, 2NBDG staining in splenic $CD4^+$ and $CD8^+$ subsets (n=3 mice). **f,** Schema for 2NBDG/FDG co-injection experiment. **g,** Representative histogram of 2NBDG hi and 2NBDG lo populations collected via flow sorting. **h,** Per cell FDG avidity of flow-sorted $2NBDG^{lo}$ versus $2NBDG^{ho}$ splenic T cells (n=3 mice). Each data point represents a biological replicate and graphs show mean and SEM. Data are from representative studies performed independently at least twice. P values were calculated using the Brown-Forsythe and Welch ANOVA with Dunnett's T3 for multiple comparison tests for (b,e), 2-tailed Welch's t test for CD4 comparisons in (e), and a paired t-test for (h). * $p<0.05$, ** $p<0.01$, *** $p<0.001$. 2NBDG: 2-(N-(7-Nitrobenz-2-oxa-1,3-diazol-4-yl)Amino)-2-Deoxyglucose); CM: central memory; CPM: counts per million; EM: effector memory; FDG: fluorodeoxyglucose; Tconv; conventional CD4 T cell; Treg: regulatory CD4 T cell

Myeloid cells uptake the most glucose in the tumor microenvironment

Effector T cells and inflammatory myeloid cells both use glycolysis and are subjects for immunotherapeutic strategies in the TME. $CD3^+$ T cells, $CD11b^+$ myeloid cells, and $F4/80^+$ macrophages were abundant in MC38 tumors without clear differences in spatial distribution or proximity to $CD31^+$ endothelial cells that would suggest differential nutrient access (**Figure 2.6**). Characterization of immune infiltrates across various tumor models demonstrated diversity in immune cell composition (**Figure 2.7)**. We next sought to compare the FDG uptake between tumor T cells, myeloid cells, and cancer cells in the MC38 model using microbeads to isolate each population. T cells in the TME had greater *in vivo* FDG avidity than resting splenic T cells and similar FDG avidity to cancer cells (**Figure 2.8a-b, Figure 2.9a**), suggesting that these cells are not glucose deprived. T cell glucose uptake was significantly lower, however, than that of the remaining $CD45^+$ non-T cells.

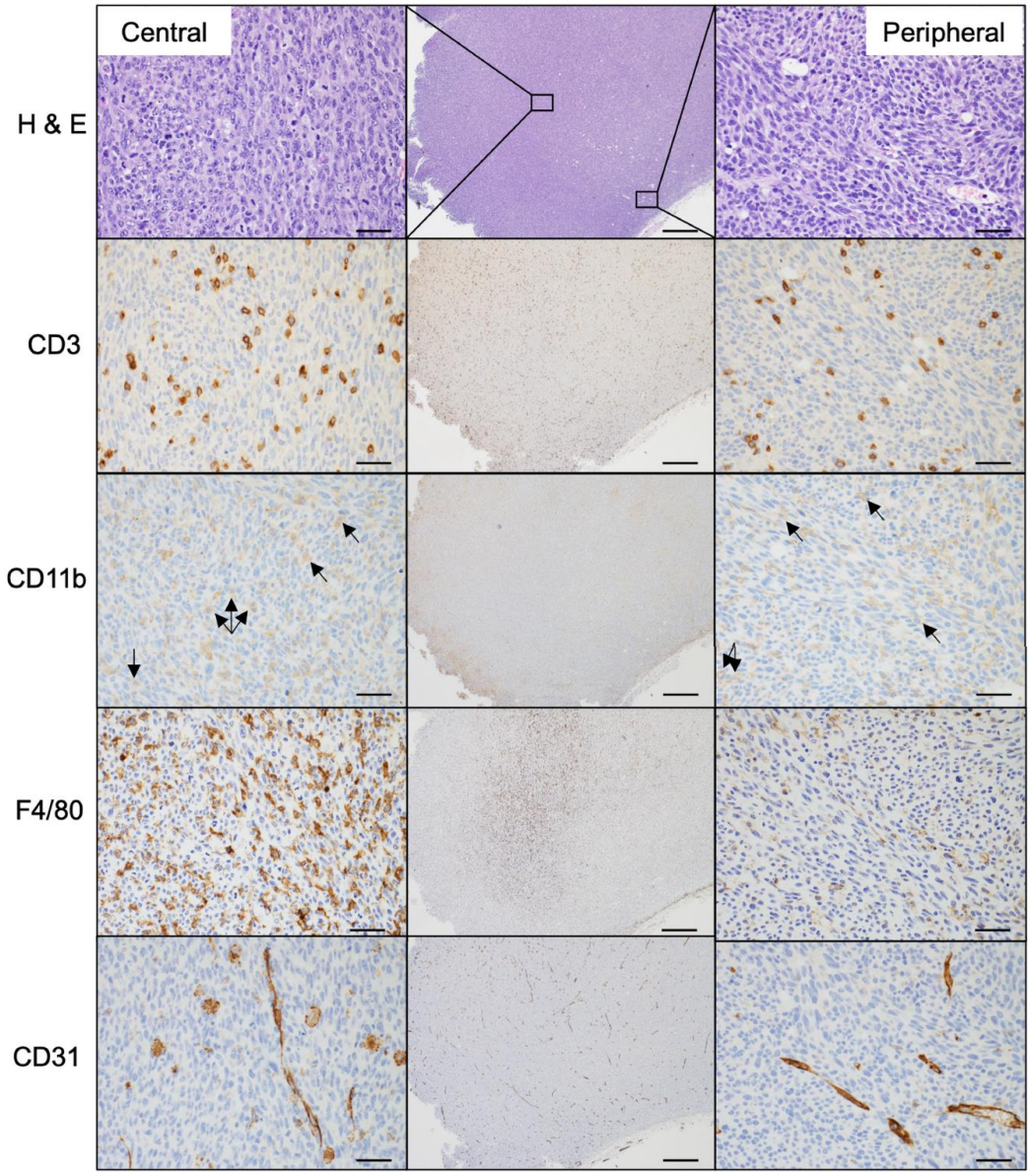

Figure 2.6: Spatial organization of immune cells in subcutaneous MC38 tumors.
Representative micrographs of H&E and indicated immunohistochemistry (IHC) stains of subcutaneous MC38 tumors. Arrows indicate positive cells on faint CD11b stain. Center column is low power overview (scale bar = 200μm). Insets demonstrate high power images from central (left) and peripheral (right) tumor locations (scale bar = 20μm). Images are representative from 5 biological replicates.

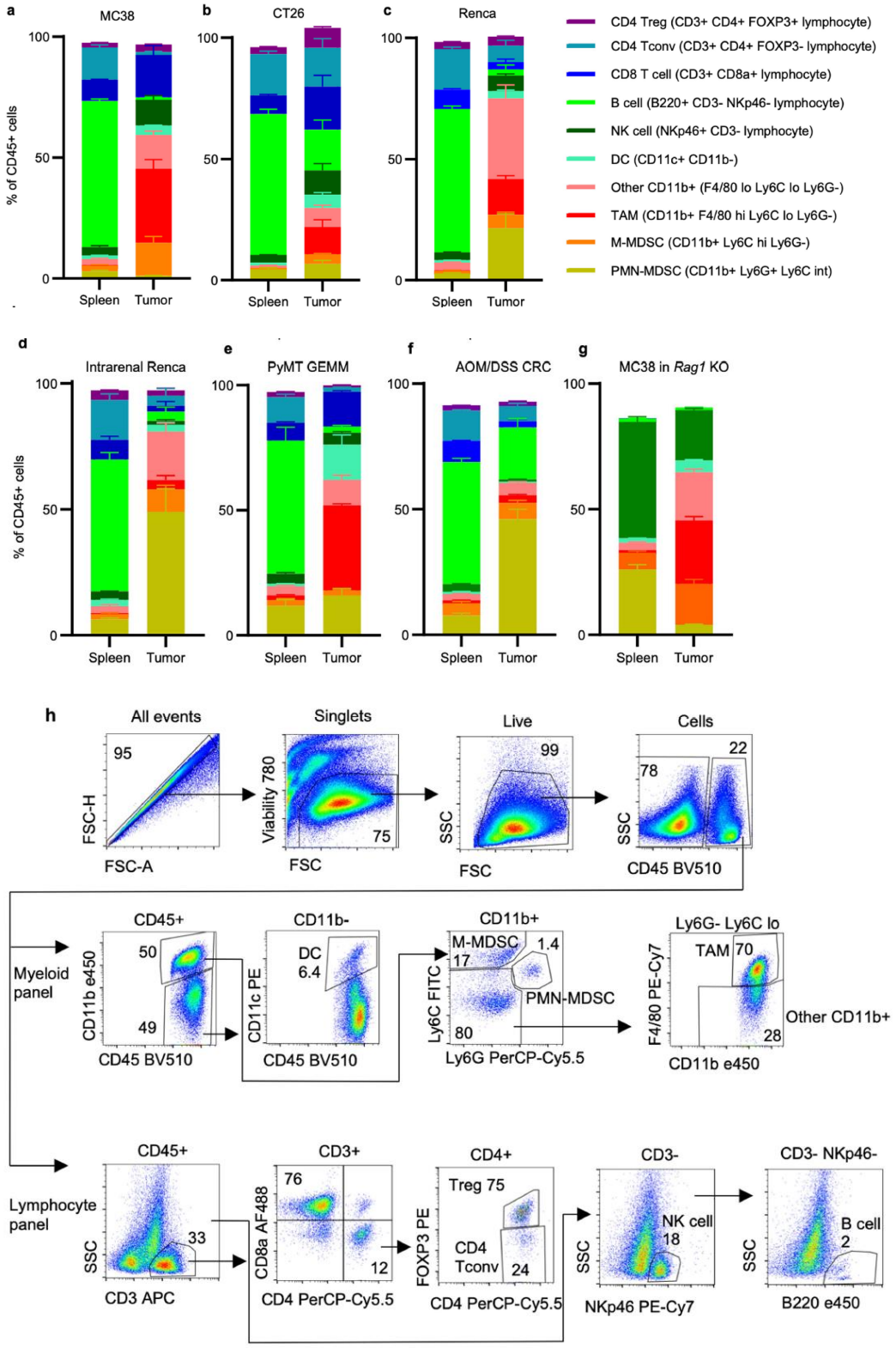

Figure 2.7: Tumor model characterizations by flow cytometry. a-g, Spleen and tumor CD45$^+$ immune cell populations from MC38 (**a**) (n=3 mice), CT26 (**b**) (n=4 mice), and Renca (**c**) (n=4 mice) subcutaneous tumors; intrarenal Renca tumors (**d**) (n=3 mice); spontaneous PyMT GEMM tumors (**e**) (n=3 mice); AOM/DSS CRC tumors (**f**) (n=6 for tumors, n=11 mice for spleens); and

MC38 subcutaneous tumors grown in *Rag1*$^{-/-}$ mice (**g**) (n=6 mice). **h,** Gating strategy for immune cell identification using lymphocyte and myeloid-focused antibody panels. Each data point represents a biological replicate and graphs show mean and SEM. Data from a-f are representative of independent experiments performed at least twice. DC: dendritic cell; M-MDSC: monocytic myeloid-derived suppressor cell; NK cell: natural killer cell; PMN-MDSC: polymorphonuclear myeloid-derived suppressor cell; PyMT: polyoma virus middle T antigen; TAM: tumor-associated macrophage.

To characterize the non-T cell CD45^{+} cells, myeloid cells were isolated using CD11b positive selection beads (**Figure 2.8c-d, Figure 2.9b**). Notably, CD11b^{+} myeloid cells displayed higher FDG uptake per cell than cancer cells and other immune cells in MC38 tumors. Myeloid cells from CT26 tumors displayed a similar phenotype (**Figure 2.9c-d**), consistent with recent reports (Nair-Gill et al 2010; Hesketh et al 2019). Flow cytometry analysis of CD45^{+} CD11b^{+} cells from MC38 tumors demonstrated two dominant cell populations: Ly6G^{-}Ly6C^{hi} cells consistent with monocytic myeloid-derived suppressor cells (M-MDSC), and Ly6G^{-}Ly6C^{lo}F4/80^{hi}CD68^{+}CD206^{hi} cells consistent with tumor associated macrophages (TAM) (**Figure 2.8e**). Isolated F4/80^{hi} cells had histiocytic morphology (**Figure 2.8f**), concordant with TAM classification. Both M-MDSC isolated using Gr1 positive selection beads and TAM isolated using F4/80 positive selection beads demonstrated high FDG avidity (**Figure 2.8g-h, Figure 2.9e-f**). CD11b^{+} cells demonstrated high glucose uptake even in B- and T cell-deficient *Rag1*$^{-/-}$ (**Figure 2.7g**), showing that high glucose uptake in myeloid cells is independent of adaptive immunity (**Figure 2.9g**). Conventional type 1 dendritic cells (cDC1) are critical to support anti-tumor CD8 T cell activity (Spranger et al 2017). CD11b^{-}CD11c^{+} cDC, displaying a MHCII^{+}CD103^{+}Ly6C^{-} phenotype consistent with cDC1, had lower glucose uptake than CD11b^{+} myeloid cells but greater glucose uptake than cancer cells and non-myeloid immune cells in the TME (**Figure 2.9h-j**).

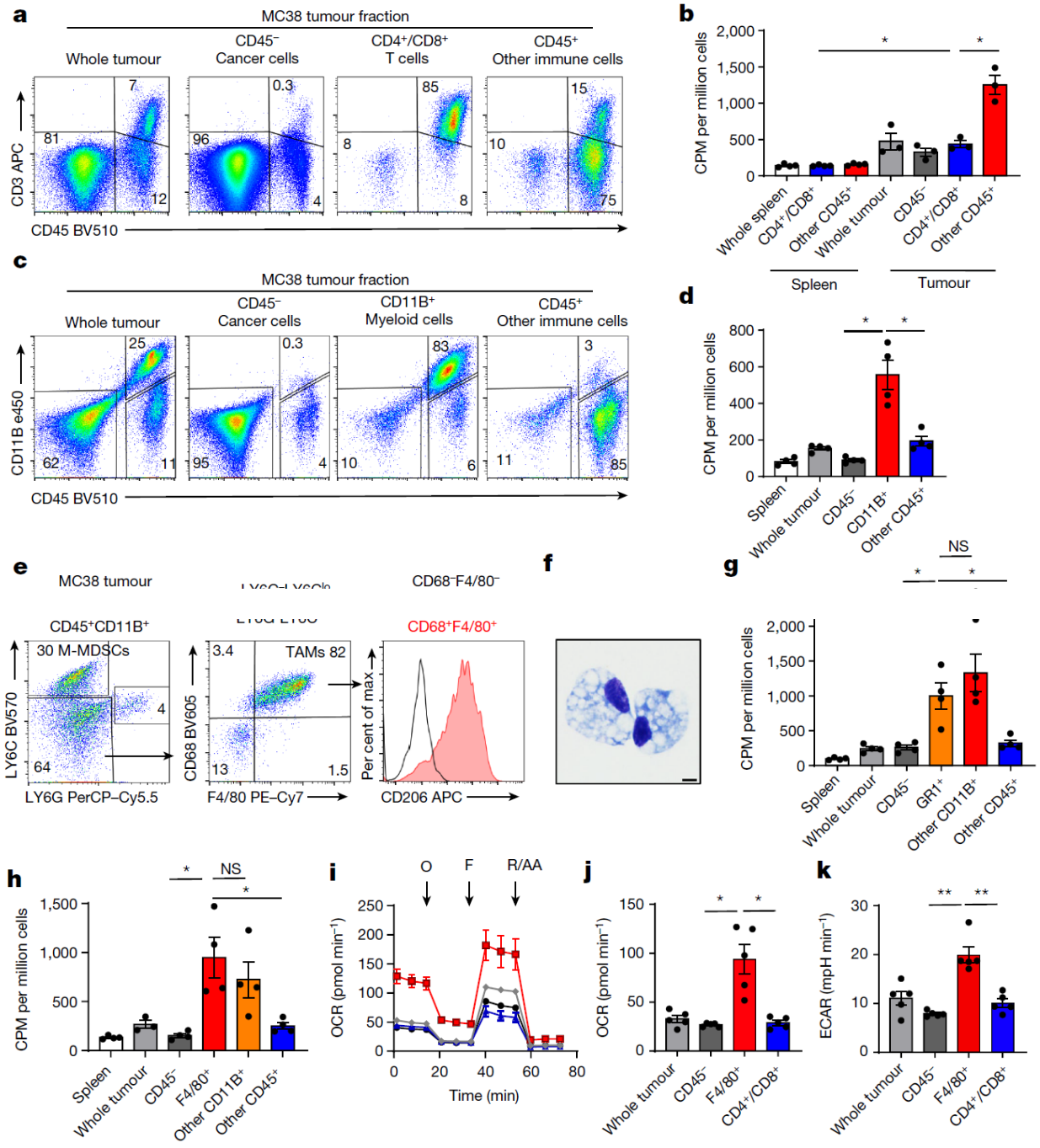

Figure. 2.8: TME myeloid cells uptake more glucose than cancer cells. a, Representative flow cytometry from CD4/8 microbead fractionated MC38 tumors gated on live cells. **b**, FDG avidity in designated cell fractions (n=3 for tumor, n=4 mice for spleen). **c,** Representative flow from CD11b microbead fractionated MC38 tumor gated on live cells. **d,** FDG avidity in designated cell fractions (n=4 mice). **e**, Representative flow cytometry plots of MC38 tumor CD11b^{+} myeloid cells. **f**, Representative (of n=2 mice) H&E-stained micrograph of F4/80 microbead-isolated TAM (scale bar = 5μm). **g-h**, FDG avidity in designated MC38 tumor cell fractions using Gr1 (n=4 except Wh Tum n=3 mice) (g) or F4/80 microbeads (n=4 mice) (h). **i,** Representative (of n=5 mice) OCR tracings from MC38 tumor cell fractions with oligomycin

(O), FCCP (F), and rotenone and antimycin A (R/AA). **j-k,** Basal mitochondrial OCR (**j**) and cellular ECAR (**k**) of MC38 tumor fractions (n=5 mice). Each data point represents a biological replicate except for (i) which shows technical replicates of a single biological replicate, and graphs show mean and SEM. Independent representative studies were performed at least twice. P values were calculated using Welch's 2-tailed t-test. * $p<0.05$, ** $p<0.01$, *** $p<0.001$. ECAR: extracellular acidification rate; M-MDSC: monocytic myeloid-derived suppressor cell; OCR: oxygen consumption rate; TAM: tumor-associated macrophage

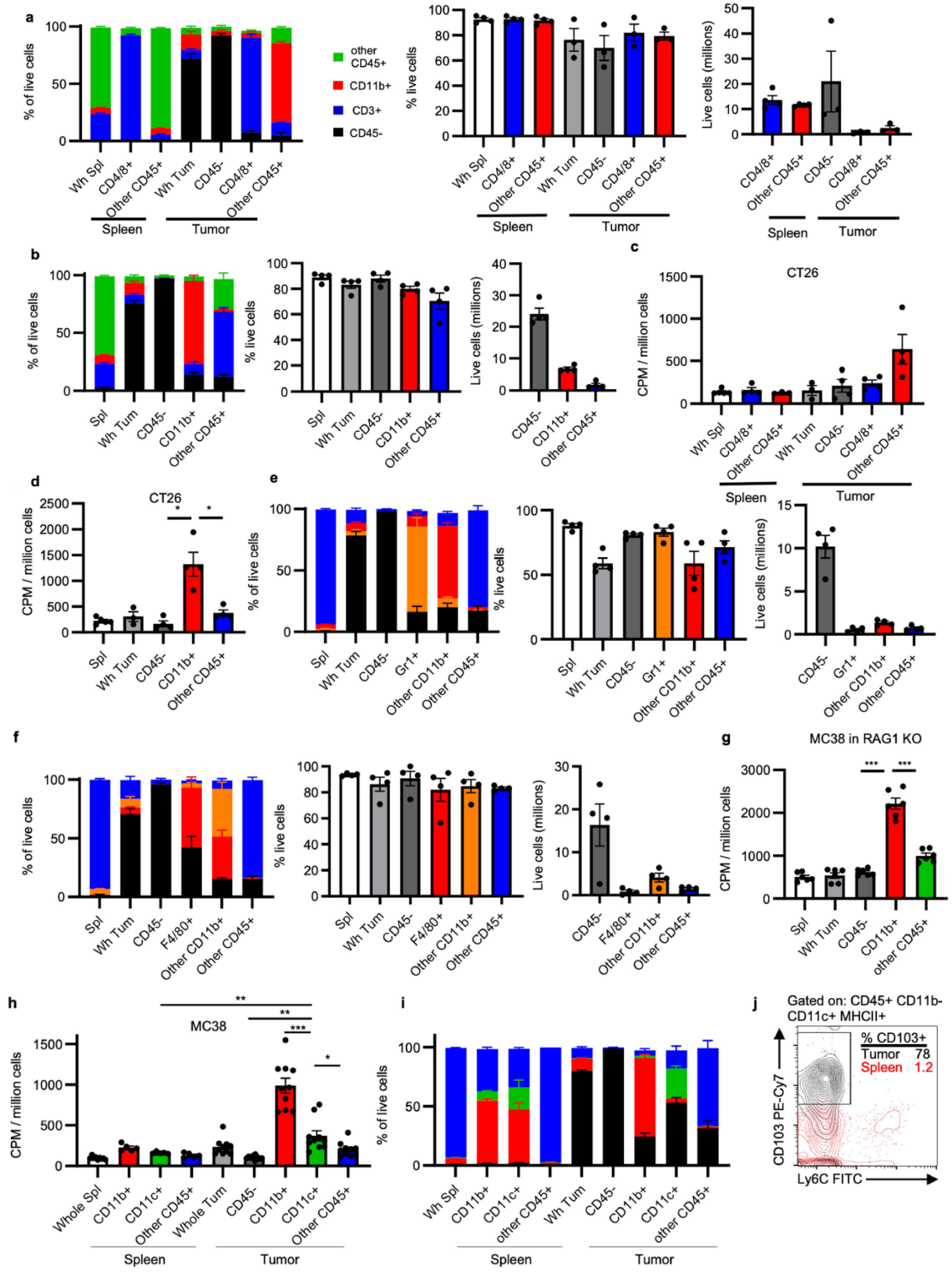

Figure 2.9: MC38 and CT26 cell isolation characterization and glucose uptake in RAG1 KO mice and in cDC. **a-b**, Fraction composition, viability, and live cell yield from MC38 tumor fractions isolated using CD4/8 microbeads (n=3 for tumors, n=4 mice for spleens) (**a**) and CD11b microbeads (n=4 mice) (**b**). **c-d**, Cellular FDG avidity in designated CT26 tumor cell

fractions using CD4/8 microbeads (n=5 for Wh Spl, n=3 for Spl other CD45+ and Wh Tum, n=4 mice for all others) (**c**) and CD11b microbeads (n=5 for spleens, n=3 for Wh Tum, and n=4 mice for all others) (**d**). **c-f**, Fraction composition, viability, and live cell yield from MC38 tumor fractions isolated using Gr1 microbeads (**e**) and F4/80 microbeads (**f**) (n=4 mice). **g,** Cellular FDG avidity in designated MC38 tumor cell fractions from *Rag1* KO mice (n=6 mice). **h,** Cellular FDG avidity in MC38 tumor cell fractions using CD11b and CD11c microbeads (n= 9 for Wh Spl, n=5 for spleen fraction, n=10 mice for all others). **i,** Fraction composition of CD11c purification (n= 9 for Wh Spl, n=5 for spleen fraction, n=10 mice for all others). **j,** Representative flow cytometry illustrating CD103 and Ly6C staining of cDC ($CD45^+$ $CD11b^-$ $CD11c^+$ $MHCII^+$ cells) from MC38 tumor and spleen. Each data point represents a biological replicate and graphs show mean and SEM. Data are representative of independent experiments performed at least twice. (h) includes data from two independent experiments. P values were calculated using Welch's 2-tailed t-test. * $p<0.05$. ** $p<0.01$, *** $p<0.001$. cDC1: type 1 conventional dendritic cell

We conducted extracellular flux assays on microbead-fractionated MC38 tumors to validate metabolic activity of cells in the TME. Isolated $F4/80^+$ TAM maintained higher basal cellular extracellular acidification rate (ECAR) and mitochondrial oxygen consumption rate (OCR) than tumor infiltrating T cells and cancer cells (**Figure 2.8i-k**). These studies show TAM and M-MDSC consume the most per cell glucose in the TME and maintain active glucose metabolism. Consistently, myeloid infiltration has been correlated with FDG avidity in non-tumor bearing lymph nodes in human and mouse gynecological malignancies (Mabuchi et al 2020). Our data extend these findings directly to the TME and reveal the relative metabolic phenotypes of heterogeneous cells in the TME.

mTORC1 and transcription programs support metabolism in the tumor microenvironment

Mechanistic target of rapamycin complex 1 (mTORC1) supports anabolic metabolism and nutrient uptake (Saxton & Sabatini 2017). We observed mTORC1 pathway activity by higher levels of phosphorylated ribosomal protein S6 (pS6) in tumor myeloid cells compared to other tumor cell subsets in human ccRCC, murine MC38, and murine CT26 tumors (**Figure 2.10, Figure 2.11a-c,**

Figure 2.12a, Table 2.1). To determine whether mTORC1 supports glucose uptake in the TME, we treated MC38 tumor-bearing mice with rapamycin for four days and measured FDG uptake in tumor cell populations. Rapamycin did not affect tumor weights, glucose, glutamine, or lactate concentration in the TME, but significantly decreased pS6 levels, T cell infiltration, Ki67 levels in cancer cells and T cells, and TAM cell size (**Figure 2.11d, Figure 2.12b-f).** Rapamycin treatment led to significant decreases in myeloid and cancer cell FDG uptake (**Figure 2.11e**). Extracellular flux demonstrated that *in vivo* rapamycin treatment decreased myeloid cell metabolism *ex vivo*, while cancer cells and T cells remained unchanged (**Figure 2.11f-h**). Tumor CD8 T cells and TAM retained phenotypic markers after rapamycin treatment, but CD8 T cells displayed a functionally less activated phenotype (**Figure 2.12g-n, Figure 2.13**).

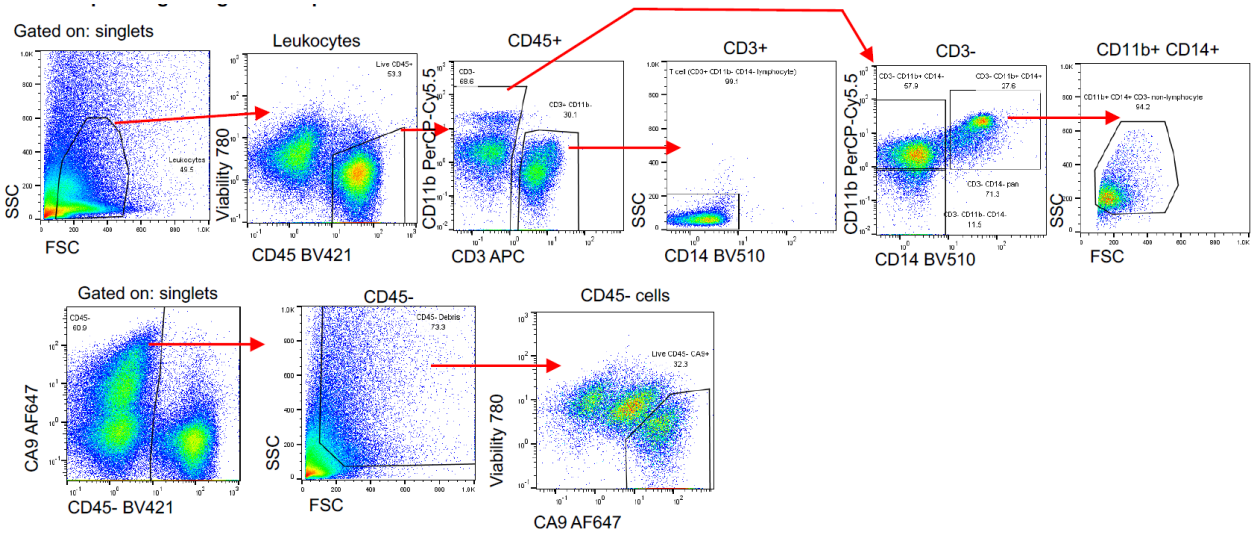

Figure 2.10: Flow cytometry gating scheme for pS6 analysis of human ccRCC tumors.

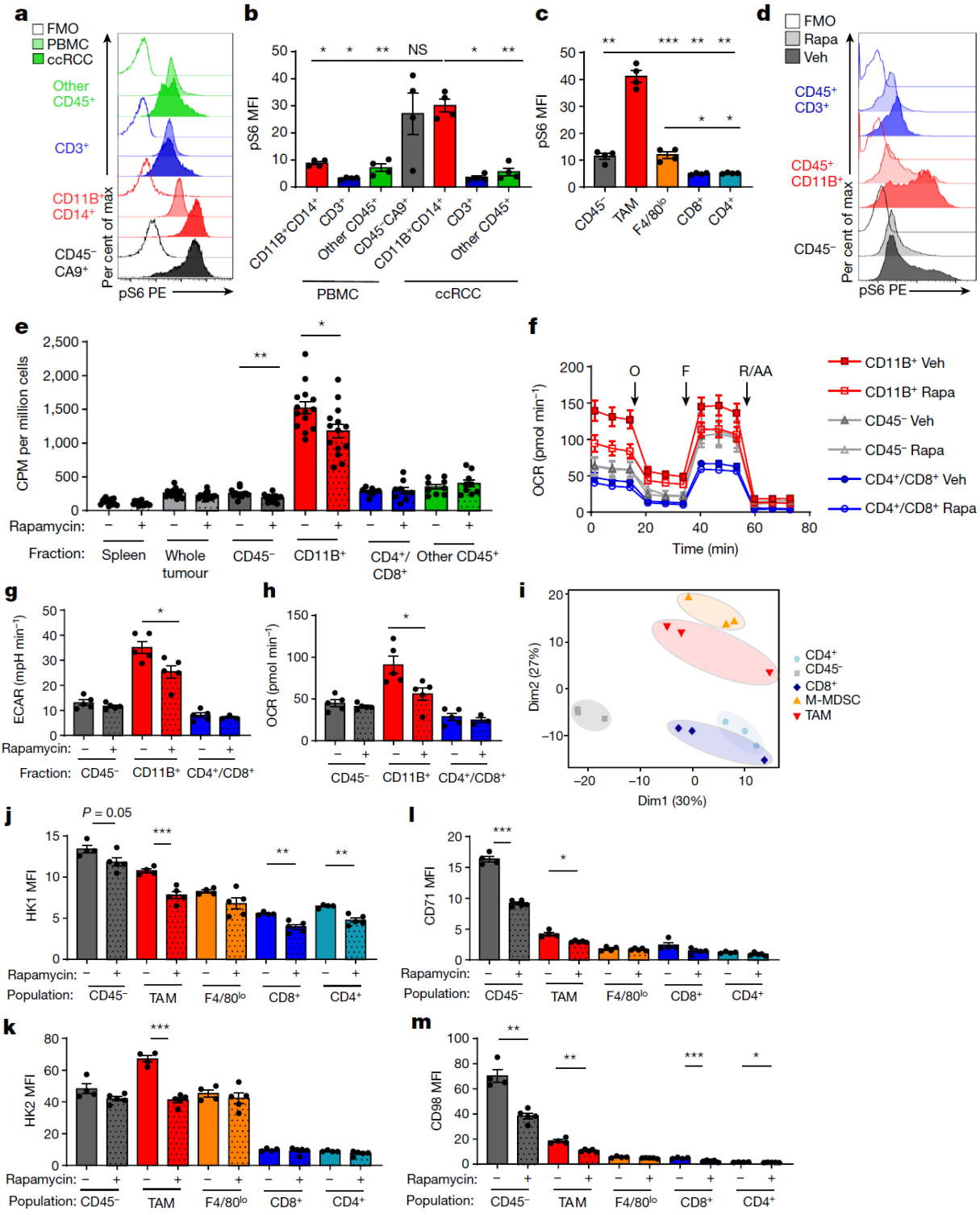

Figure 2.11: mTORC1 supports glucose uptake and metabolism in the TME. a-c, Phosphorylated S6 (pS6) levels in indicated cell populations by flow cytometry in human peripheral blood mononuclear cells (PBMC) and matched ccRCC (representative histograms **a**, quantification **b**) (n=4 patients) and MC38 tumors (**c**) (n=4 mice). **d**, Representative histograms

of pS6 levels in MC38 tumor cells from mice treated with rapamycin or vehicle. **e**, FDG avidity in designated MC38 tumor cell fractions with rapamycin treatment (n=15 for Spl Veh, n=8 for CD4/8$^+$ veh, n=9 for CD4/8$^+$ rapa and other CD45$^+$, and n=14 mice for all other groups). **f,** Representative (of n=5 mice/group) OCR tracings from fractionated MC38 tumors from mice treated with rapamycin or vehicle with indicated injections of oligomycin (O), FCCP (F), and rotenone and antimycin A (R/AA). **g-h,** Basal cellular ECAR (**g**) and mitochondrial OCR (**h**) of MC38 tumor fractions from mice treated with rapamycin or vehicle (n=5 except for CD4/8$^+$ rapa n=3 mice/group). **i,** PCA plot of metabolism-related mRNA transcripts from CD45$^-$, TAM, M-MDSC, CD8 T cell, and CD4 T cell flow-sorted populations from MC38 tumors (n=3 mice). **j-m**, Flow cytometry quantification of HK1 (**j**), HK2 (**k**), CD71 (**l**), and CD98 (**m**) in MC38 tumor cell populations from mice treated with rapamycin or vehicle (n=4 for veh, n=5 mice for rapa). **c-d, i-m** are representative of at least two independent experiments. (e**)** is the combined data of three independent experiments. Each data point represents a biological replicate except for (f) which shows technical replicates of a single biological replicate, and graphs show mean and SEM. P values were calculated using Brown-Forsythe and Welch ANOVA with Dunnett's T3 for multiple comparison tests for (b-c) and Welch's 2-tailed t-test for (e-m). * p<0.05, ** p<0.01, *** p<0.001. FMO: fluorescence minus one; MFI: median fluorescence intensity; M-MDSC, monocytic myeloid derived suppressor cell; PBMC: peripheral blood mononuclear cell; pS6: phosphorylated ribosomal protein S6 (Ser235/236); Rapa: rapamycin

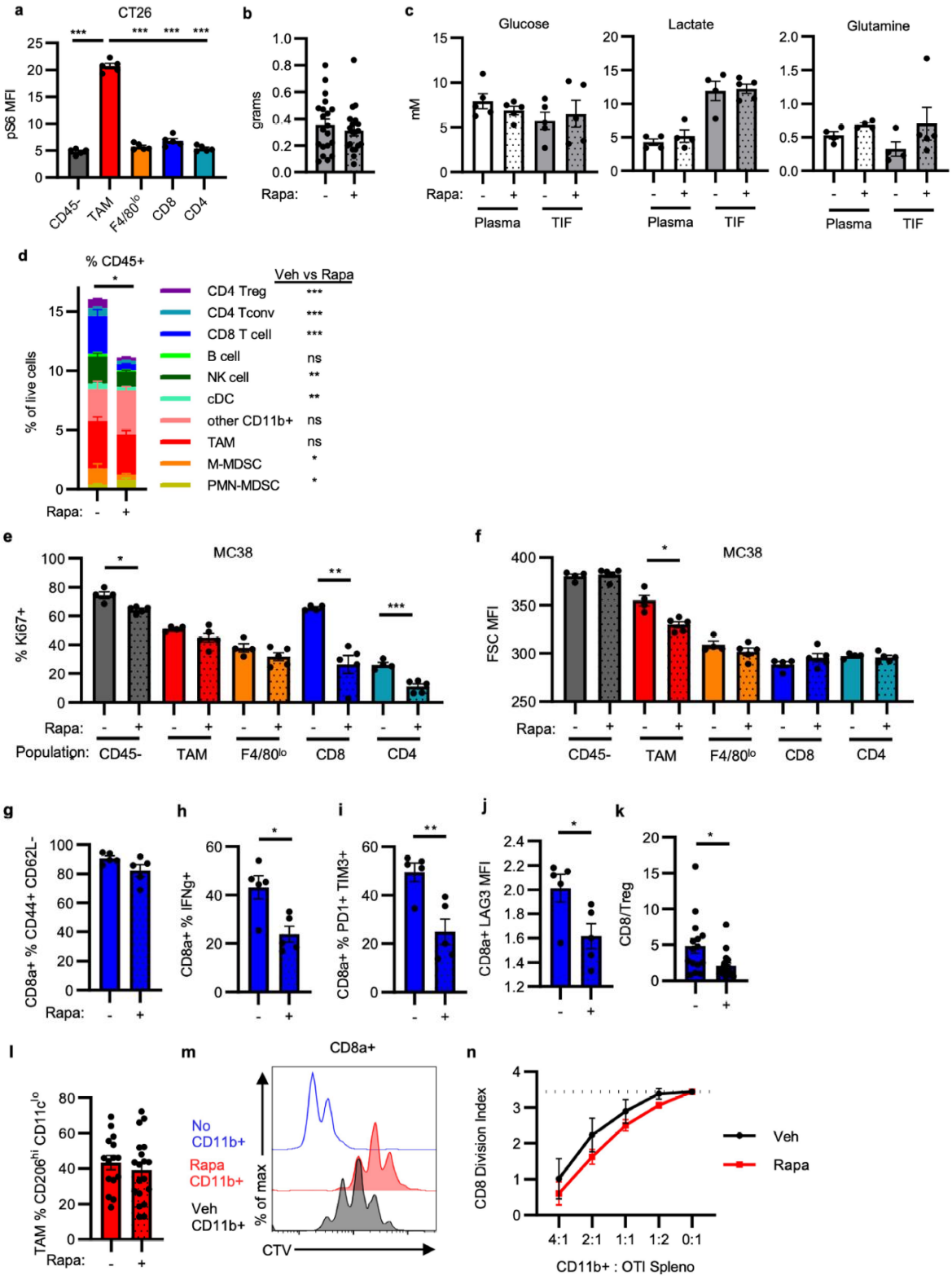

Figure 2.12: Effect of rapamycin treatment on the MC38 TME. **a**, pS6 levels in CT26 tumor populations (n=5 mice). **b,** MC38 tumor mass at study endpoint with rapamycin (n=20 for veh, n=19 mice for rapa). **c**, Metabolite concentrations in tumor interstitial fluid (TIF) and matched

plasma from MC38 tumor-bearing mice treated with rapamycin or vehicle (n=5, except for lactate and glutamine plasma and TIF veh n=4 mice). **d,** Immune cell infiltration of MC38 tumors from mice treated with rapamycin or vehicle (n=15 for veh, n=19 mice for rapa). Significance between rapamycin and vehicle treatment for individual populations indicated in legend. Significant decrease in total $CD45^+$ cell infiltration is noted. **e-f,** Flow cytometry quantification of Ki67 positivity (**e**) and cell size (forward scatter, FSC) (**f**) from MC38 tumor populations in mice treated with rapamycin or vehicle (n=4 for veh, n=5 mice for rapa). **g-k** MC38 tumor $CD3^+CD8a^+$ T cell phenotypes from rapamycin or vehicle treated mice for effector memory phenotype (**g**), *ex vivo* IFNγ production (**h**), PD1 and TIM3 expression (**i**), LAG3 expression (**j**) (n=5 mice/group), and ratio of CD8 T cells to $CD4^+FOXP3^+$ Treg (**k**) (n=15 for veh, n=19 mice for rapa). **l,** % M2-like TAM ($CD11c^{lo}CD206^{hi}$) in MC38 tumors from mice treated with rapamycin or vehicle (n=15 for veh, n=19 mice for rapa). **m-n**, Myeloid suppression assay representative histogram of $CD8a^+$ OT-I T cell dilution of CellTrace Violet (CTV) indicative of proliferation (**m**) and quantification of division index (**n**) for MC38 tumor myeloid cells isolated using CD11b microbeads from rapamycin and vehicle-treated mice (n=5 mice/group). Each data point represents a biological replicate and graphs show mean and SEM. Data in (a, e-j) are representative of independent experiments performed at least twice. (b, d, k-l) display data merged from 4 independent experiments. P values were calculated using the Brown-Forsythe and Welch ANOVA with Dunnett's T3 for multiple comparison tests (a) and Welch's 2-tailed t-test (b-l, n). * $p<0.05$. ** $p<0.01$, *** $p<0.001$. pS6: phosphorylated ribosomal protein S6 (Ser235/236); Rapa: rapamycin; TIF: tumor interstitial fluid.

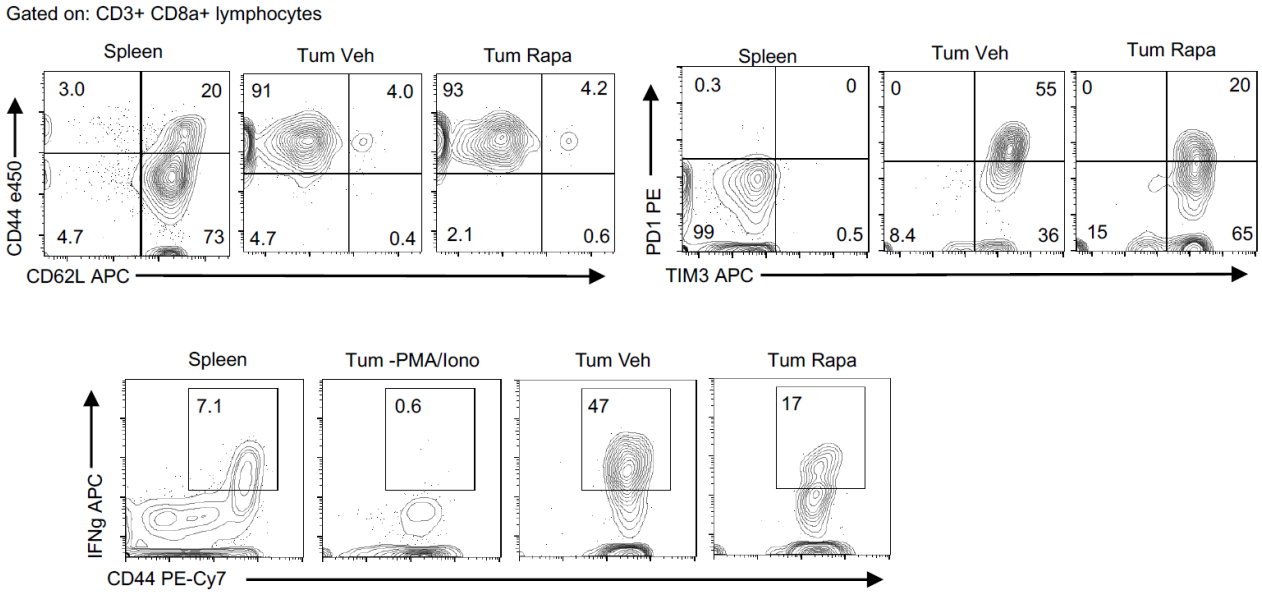

Figure 2.13: Flow cytometry gating strategy of tumor-infiltrating T cells from rapamycin-treated tumors.

Flow-sorted CD45$^-$ cancer cells, TAM, M-MDSC, CD8 T cells, and CD4 T cells from MC38 tumors were transcriptionally profiled (**Figure 2.14a**). In untreated tumors, principal component analysis and unbiased clustering based on only metabolism-related transcripts grouped samples by cell identity (**Figure 2.11i, Figure 2.14b**). Corresponding with increased glucose uptake in myeloid cells, gene set enrichment analysis revealed relative enrichment of glucose-related pathways in M-MDSC and TAM (**Figure 2.14c, Table 2.2**). Glucose transporters demonstrated population-specific expression, with cancer cells and myeloid cells expressing high transcript levels of *Slc2a1* (GLUT1) and T cells expressing high levels of *Slc2a3* (GLUT3). Hexokinase isoforms *Hk2* and *Hk3*, which catalyze glucose phosphorylation in cells as the rate-limiting initial phosphorylation of glucose in glycolysis, were most highly expressed in myeloid cells in contrast to broadly expressed *Hk1*. CD45$^-$ cancer cells displayed amino acid, lipid, and signaling-related transcripts, and CD8 T cells were enriched in nucleotide-related transcripts. Rapamycin increased glycolysis-related transcript levels, particularly in CD45$^-$ cancer cells, while other metabolic gene transcripts decreased, including amino acid-related transcripts (**2.15a-e**). Gene expression levels and changes after rapamycin treatment were confirmed at protein levels by flow cytometry. Rapamycin treatment reduced HK1 across tumor cell populations and HK2 specifically in TAM, potentially underlying differences in glucose uptake **(Figure 2.11j-k)**. GLUT1 levels remained unchanged (**Figure 2.15f**), yet iron transporter CD71 and amino acid transporter CD98 protein levels decreased with rapamycin treatment (**Figure 2.11l-m**).

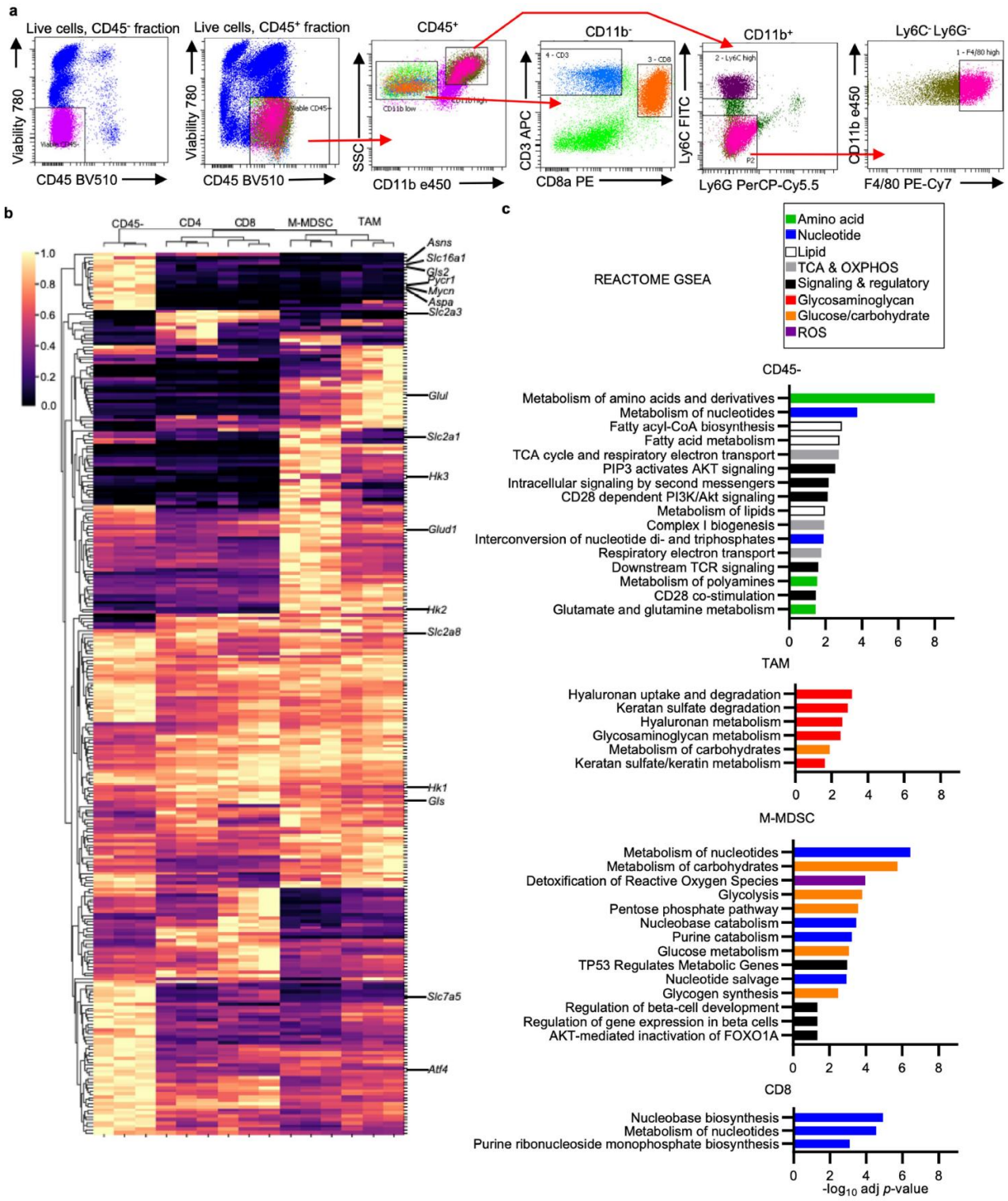

Figure 2.14: Metabolic transcriptional signatures of MC38 tumor cell populations. a, Cell sorting scheme of MC38 tumor cell populations used for mRNA transcript analyses. **b,** Clustering analysis heatmap of differentially expressed metabolic genes from MC38 tumor cell populations. Select genes annotated. **c**, Reactome gene set enrichment analysis for genes most highly expressed in each MC38 tumor population. Significantly enriched gene sets are shown and colored according to metabolic pathway. OXPHOS; oxidative phosphorylation; TCA; tricarboxylic acid cycle

Table 2.2: Genes most highly expressed in distinct MC38 tumor populations.
Gene lists were generated based on clustering analysis of differentially expressed genes (FDR <0.01) and were subsequently used for gene set enrichment analysis.

CD45-		TAM	M-MDSC	CD8	CD4
Fah	Prdx1	Slc27a1	Ass1	Fdx1	Slc2a3
Aox1	Akt1s1	Idh2	Nt5e	Psph	Adora2a
Asns	Fahd1	Naglu	Haa0	Eno3	Hsd11b1
Slc16a1	Nadk2	Ada	Slc16a3	Rrm1	Ehhadh
Gls2	Pck2	Gmpr	Slc3a1	Rrm2	Pparg
Mapk8ip1	Acat2	Ptgs1	Upp1	Ppat	Nos1
Ptges	Fasn	Apoe	Vegfa	Cad	Odc1
Ak5	Sqstm1	Gatm	Cybb	Shmt1	Glrx
Pycr1	Pemt	Alox5	Apoc2	Tfrc	Hif1a
Mycn	Pfkm	Trf	Deptor	Bcl2	
Aspa	Psmb10	Idh1	Prdx5	Afmid	
Adh7	Txn1	Fnip2	Atox1	Pfkb1	
Scd1	Nme2	Car9	Gpx1	Impdh1	
Thbs2	Psma7	Dglucy	Pgd	Slc1a5	
Sardh	Acaca	Tbxas1	Ampd3	Kmt2a	
Mras	Prkaa1	Glul	Gda	Plcg1	
Pik3r2	Gpx4	Hexa	Hk3	Pik3r1	
Atg101	Atf4	Slc16a7	Nfe2l2	Cab39	
Ndufa7	H6pd	Gns	Slc7a11	Rpia	
Cox7c	Ppm1a	Gusb	Ptgs2	Lta4h	
Ndufa6	Impdh2	Hexb	Thbs1	Me2	
Acat1	Pycrl	Pla2g15	Kynu	Mycn	
Ndufa12	Agk	Aldob	Gad1	Gart	
Ndufb10	Gmps	Acy1	Kmo	Idh3a	
Ndufb2	Ampd2	Fabp5	Hdc	Acadl	
Mat2a	Mrps5	Slc16a6	Nat8l	Prps1	
Psmc1	Ndufa4		Aldh2	H2-Ke6	
Psma3	Sod1		Mgst3	Tfam	
Uqcr10	Ak3		Aprt		
Wdr45	Tecr		Eno1		
Map3k12	Adk		Uck2		
Prr5	Hadh		Pdk3		
Psat1	Rptor		Akt1		
Slc7a5	Srr		Glud1		
Ctps	Mcat		Pgm1		
Pebp1	Shmt2		Txnrd1		
Insr	Pdp1		Ern1		
Cbr4	Rictor		Nadk		
Srm			Akt3		
			Psmb10		
			Slc3a2		
			Pfkl		
			Pkm		
			Aloa		
			Mpc1		
			Pgk1		
			Xdh		
			Taldo1		
			G6pdx		
			Map2k1		
			Sod2		

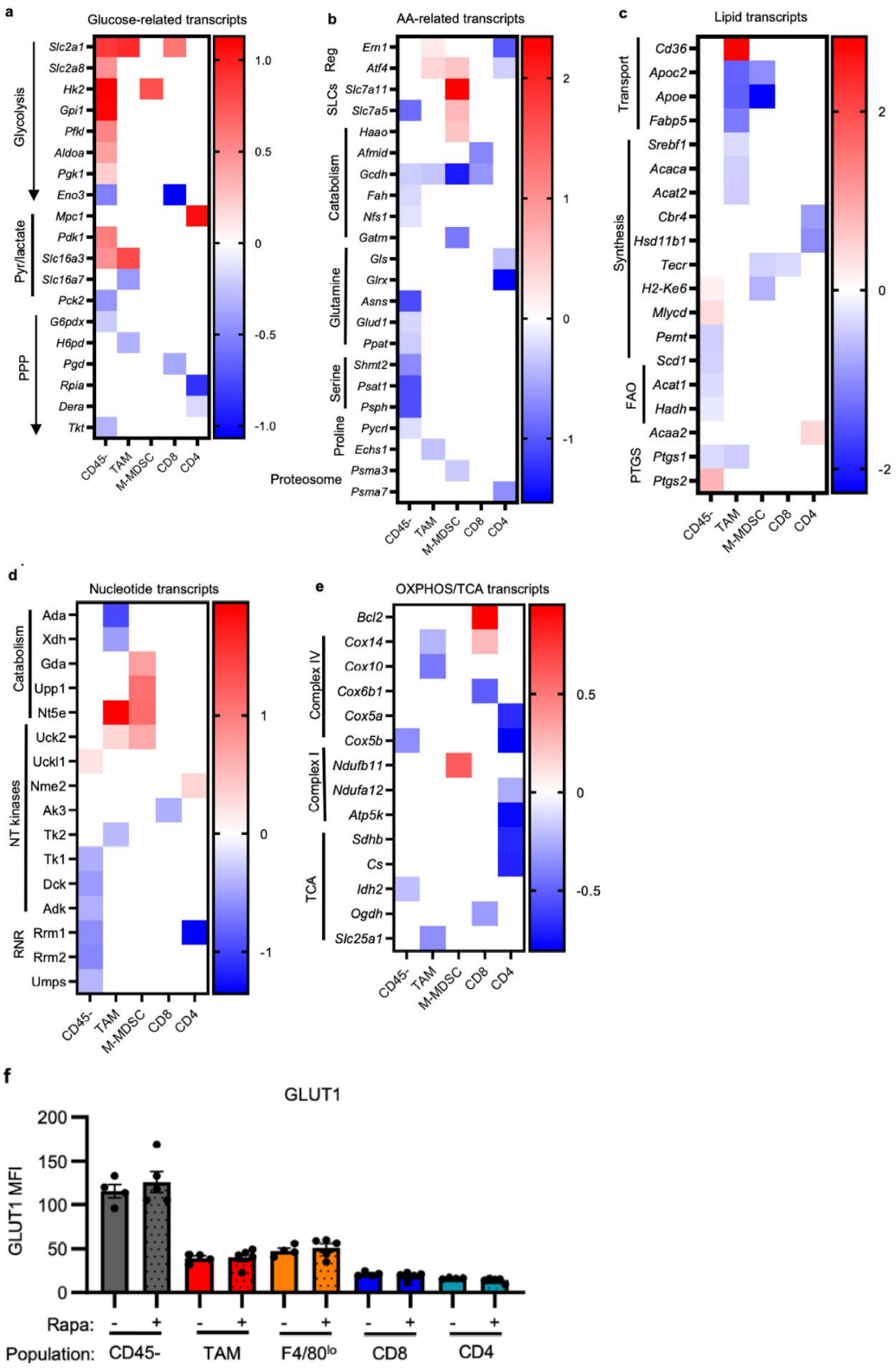

Figure 2.15: Effects of rapamycin on MC38 tumor population metabolic markers. a-e, Heatmaps of significantly altered metabolic genes between rapamycin and vehicle-treated MC38 tumor cell populations for indicated metabolic pathways. White spaces indicate non-significant

changes with rapamycin treatment for that gene and tumor cell population. Genes were grouped and classified manually. (n=3/group, except n=2 for rapamycin treated M-MDSC and CD4) **f,** Flow cytometry quantification of GLUT1 expression in MC38 tumor populations from mice treated with rapamycin or vehicle (n=4 for veh, n=5 mice for rapa). Each data point represents a biological replicate and graphs show mean and SEM. AA: amino acid; FAO: fatty acid oxidation; NT: nucleotide; OXPHOS: oxidative phosphorylation; PPP: pentose phosphate pathway; PTGS: prostaglandin synthases; Reg: regulatory genes; RNR: ribonucleotide reductase; SLCs: solute carrier proteins; TCA tricarboxylic acid cycle

Cancer cells uptake relatively more glutamine and lipids in the tumor microenvironment

Having shown that systemic glucose is preferentially consumed by tumor-infiltrating myeloid cells, we hypothesized that other nutrients also have distinct patterns of uptake in the TME. *Ex vivo* uptake of fluorescently labelled palmitate (C16 BODIPY) was highest in $CD45^-$ cancer cells, corroborating transcript enrichment data and showing that other nutrients may partition differently than glucose in the TME (**Figure 2.17a-c**). We postulated based on transcript data that glutamine uptake would also be greatest in $CD45^-$ cancer cells. TME glutamine metabolism has been shown to promote cancer cell growth while impairing anti-tumor immunity (Leone et al 2019). MYCN and ATF4 drive glutamine utilization (Yoshida et al 2020), and *Mycn* and *Atf4* were more highly expressed in MC38 cancer cells than immune cells (**Figure 2.16a-b**). Glutamine metabolism enzymes *Aspa*, *Asns*, and *Gls2* were also specifically expressed in the MC38 cancer cells, as well as other amino acid-related transcripts *Pycr1* and *Slc7a5* (**Figure 2.14b**). Tumor-bearing mice were injected with ^{18}F-(2S,4R)4-Fluoroglutamine (^{18}F-Gln) (Zhou et al 2017) to measure glutamine pool size and uptake in the TME. Subcutaneous MC38 tumors were ^{18}F-Gln avid (**Figure 2.16c, d**). In contrast to FDG, however, $CD45^-$ cancer cells demonstrated greater ^{18}F-Gln avidity than $CD45^+$ immune cells in MC38 (**Figure 2.16e**), CT26, Renca, and spontaneous AOM/DSS tumor models (**Figure 2.17d-f**).

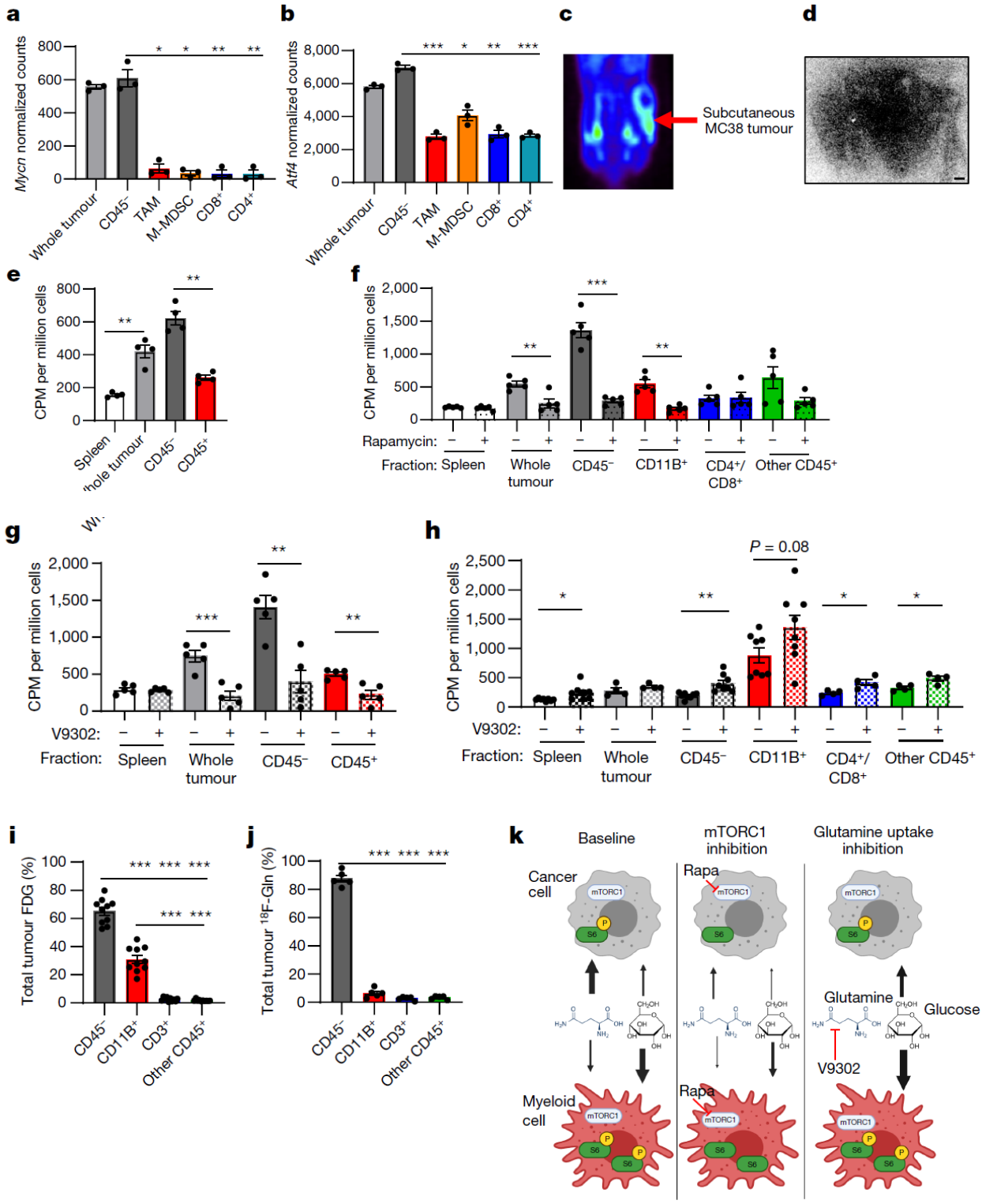

Figure 2.16: Glutamine partitions into cancer cells in the TME. a-b, Glutamine-related transcription factor mRNA transcript levels of flow-sorted MC38 tumor cell populations (n=3 mice). **c,** Representative ^{18}F-Gln image of subcutaneous MC38 tumor. **d,** ^{18}F-Gln autoradiography image of subcutaneous MC38 tumor (scale bar = 800μm). **e,** Cellular ^{18}F-Gln avidity in designated

MC38 tumor cell fractions (n=4 mice). **f-g,** Cellular ^{18}F-Gln avidity in MC38 tumor cell fractions from mice treated with vehicle or rapamycin (f) or V9302 (g) (n=5 mice/group). **h**, FDG avidity in MC38 tumor cell fractions from mice treated with V9302 or DMSO (n=4 for Wh Tum, CD4/8^{+}, and other CD45^{+}; n=8 mice for all others). **i-j** Contribution of cell populations to total MC38 tumor FDG (i) (n=10 mice) and ^{18}F-Gln signal (n=5 mice) (j). **k,** Model for nutrient partitioning in the TME. Each data point represents a biological replicate and graphs show mean and SEM. Data are representative of at least two independent experiments. (h) shows combined data of two independent experiments. P values were calculated using Welch's 2-tailed t-test for (e-h) and Brown-Forsythe and Welch ANOVA with Dunnett's T3 for multiple comparison tests for (a-b, i-j). * p<0.05, ** p<0.01, *** p<0.001. ^{18}F-Gln: ^{18}F-4-fluoroglutamine; DMSO: Dimethyl sulfoxide; V9302: ASCT2 inhibitor.

Rapamycin reduced amino acid-related transcripts and CD98 protein levels. Correspondingly, rapamycin treatment sharply decreased ^{18}F-Gln uptake in CD45^{-} and myeloid cells (**Figure 2.16f**). To assess the relationship between glutamine and glucose uptake, tumor-bearing mice were treated with V9302, a small molecule inhibitor of the glutamine transporter ASCT2 (Schulte et al 2018). V9302 broadly decreased glutamine uptake by cells in the TME (**Figure 2.16g**), but increased glucose uptake in all tumor cell populations in the TME (**Figure 2.16h**). V9302 also decreased MC38 tumor mass and T cell infiltration (**Figure 2.17g, h**) and increased the frequency of tumor M2-like macrophages (**Figure 2.17i, j**). Together these data demonstrate that glutamine uptake and metabolism actively restrain glucose metabolism *in vivo* and that tumor infiltrating cells can access and increase glucose uptake beyond basal levels when glutamine is restricted. Cell-intrinsic programs of distinct tumor cell subsets thus dictate glucose and glutamine uptake in the TME.

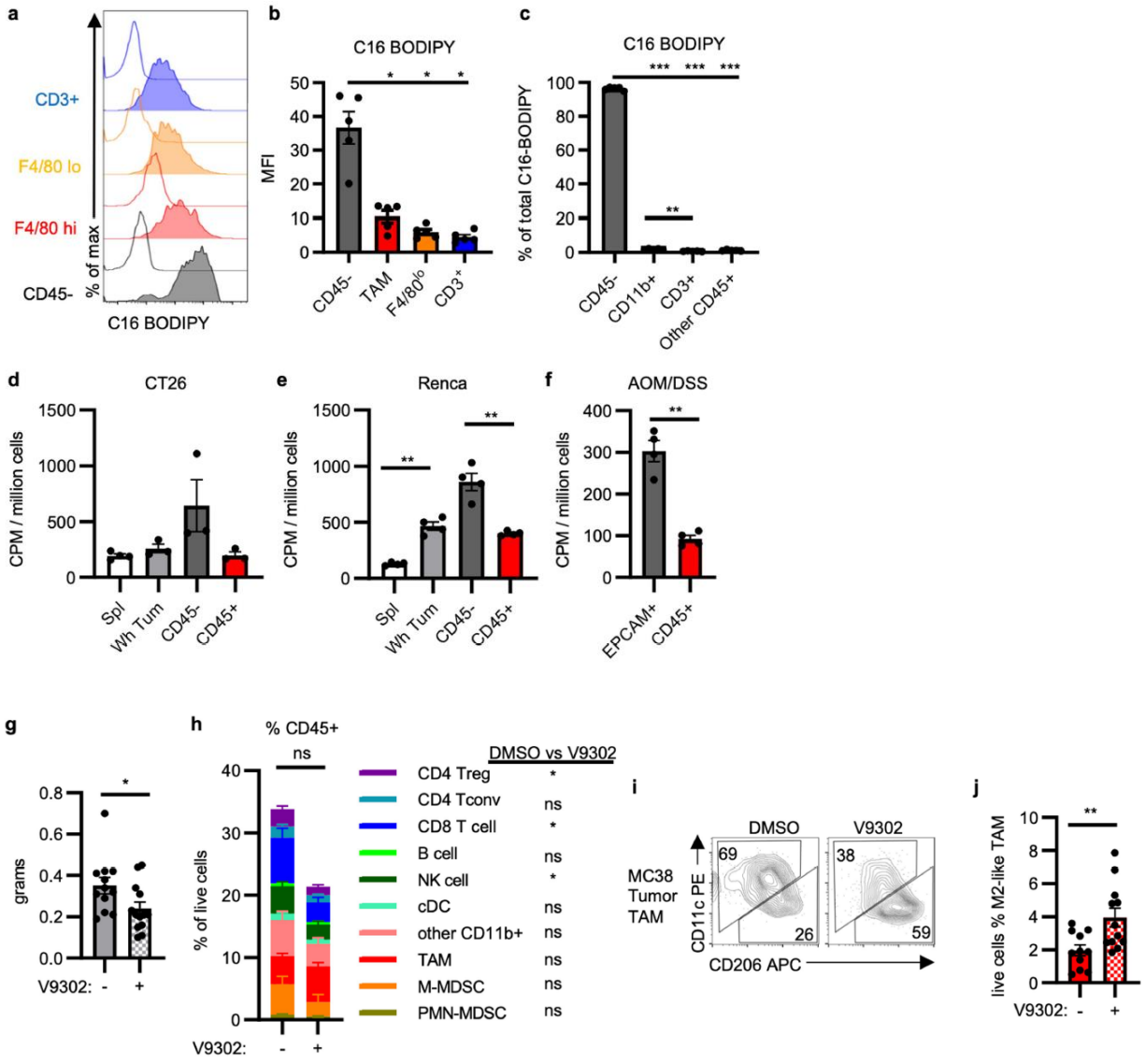

Figure 2.17: Fatty acid and glutamine uptake and the effect of V9302 treatment on the TME. a-b, Representative histograms (**a**) and quantification (**b**) for *ex vivo* staining of C16 BODIPY by indicated MC38 tumor cell populations from tumor single cell suspensions (n=5 mice). **c**, Percent contribution to total tumor C16 BODIPY signal from indicated tumor cell populations (n=5 mice). **d-f,** Cellular ^{18}F-Gln avidity in designated tumor cell fractions in CT26 (n=4 for spleen, n=3 mice for tumor) (**d**) and Renca (n=5 mice) (**e**) subcutaneous tumors and AOM/DSS spontaneous tumors (n=4 mice) (**f**). **g,** MC38 tumor mass from mice treated with V9302 or DMSO (n=13 for V9302, n=12 mice for DMSO). **h,** Immune cell infiltration of MC38 tumors from mice treated with V9302 or DMSO (n=13 for V9302, n=12 mice for DMSO). Significance between V9302 and DMSO treatment in distinct populations is indicated in legend. There is no significant change in total CD45$^+$ cell infiltration (n=13 for V9302, n=12 mice for DMSO). **i-j,** Representative plot (**i**) and abundance (**j**) of MC38 M2-like TAM from mice treated with V9302 or DMSO (n=13 for V9302, n=12 mice for DMSO). Each data point represents a biological replicate and graphs show mean and SEM. Data are representative of at least two independent experiments. (g-j) are data combined from two experiments. P values were

calculated using the Brown-Forsythe and Welch ANOVA with Dunnett's T3 for multiple comparison tests (b,c) or Welch's 2-tailed t-test (d-j). * $p<0.05$, ** $p<0.01$, *** $p<0.001$. C16 BODIPY: C16 (4,4-Difluoro-5,7-Dimethyl-4-Bora-3a,4a-Diaza-s-Indacene-3-Hexadecanoic Acid) (fluorescent analog of palmitate); V9302: glutamine uptake inhibitor

Selective nutrient partitioning

Our findings demonstrate discrete metabolic selections regulate glucose and glutamine uptake within the TME. In the context of the whole tumor, multiplying the per cell glucose uptake by the abundance of each cell type showed that cancer cells accounted overall for approximately 2/3 of glucose uptake, with myeloid cells accounting for another 1/3 and other immune cells contributing negligibly (**Figure 2.16i**). In contrast, glutamine and lipid per-cell and total tumor uptake were dominated by cancer cells (**Figure 2.16j, Figure 2.17c**). These results support the notion that glucose is not grossly limiting in the TME and utilization is instead modulated by cell intrinsic programs and glutamine uptake (**Figure 2.16k**).

Discussion

The data presented in this chapter reveals that diverse cell populations preferentially acquire distinct metabolites from a common pool of metabolites available in the TME (Sullivan et al 2019, Kilgour et al 2021), and further demonstrates that tumor myeloid cells consume significantly more glucose than tumor infiltrating T cells or cancer cells on a per-cell basis, which each remain more active than in unrelated tissues. This has implications for metabolism-targeting agents as well as myeloid targeting therapies, with the potential to either enhance or impair tumor-related inflammation. These data also support targeting glutamine metabolism as a specific strategy to hamper cancer cell growth while also increasing glucose consumption and altering immunophenotype in the TME as a result.

Previous studies have suggested competition for glucose in the TME between cancer cells and T cells contributes to immunosuppression (Ho et al 2015; Chang et al 2015; Cascone et al 2018). However, the data herein show that glucose is not broadly limiting, and TME resident cells have the capacity to increase glucose uptake *in vivo* when glutamine uptake is restricted. This cell-intrinsic programming provides a new level of insight into the innerworkings of the TME. Here, a program of mTORC1-driven glutamine uptake may suppress glycolytic gene expression and glucose metabolism in cancer cells. There is also growing evidence that glycolytic cancer cell transcriptional programs are associated with immunosuppressive TMEs and directly recruit suppressive myeloid cells (Li et al 2018; Chafe et al 2019) while TAM glycolysis may drive hypoxia via endothelial dysfunction (Wenes et al 2016) and cytokine production (Jeong et al 2019). These findings support a model where glycolytic tumors are immunoinhibitory not directly due to nutrient deficiencies but rather because of large scale microenvironmental changes which alter intrinsic cellular programming and that different nutrients may follow distinct, but cell and tumor-type specific patterns.

Myeloid cells directly consume FDG out of proportion to the cancer cells and thus account for a significant fraction (30%) of measured tumor glucose uptake in PET imaging. These findings also help explain intratumoral regional variability in FDG avidity observed on PET imaging as well as the PET avid nature of Hodgkin's lymphoma, a disease entity with far more inflammatory cells than transformed tumor cells. Understanding the biology of distinct cell types in the complex TME has contributed substantially to shaping models of tumorigenesis. Our studies extend these approaches to evaluate *in vivo* metabolic features of tumor cell types and show that individual cell

populations have distinct nutrient uptake programs that may play an important role in therapy response or resistance.

It is noteworthy that two other groups produced similar results using FDG. Nair-Gill et al 2010 described their own kind of ^{18}F-tracer partitioning, with myeloid cells picking up relatively more FDG and lymphocytes consuming more ^{18}F-deoxycytidine analog ([18F]–2-fluoro-d-(arabinofuranosyl)cytosine, or ^{18}F-FAC) in murine tumors and tumor-draining lymph nodes. These results are consistent with the findings presented in this chapter, including transcriptome analysis showing enrichment in nucleotide-related pathways in tumor CD8 T cells (**Figure 2.14c**). In Hesketh et al 2019, the investigators found that in murine xenograft tumors myeloid cells demonstrated greater FDG uptake than human cancer cells. Again, their results are consistent but using a non-syngeneic tumor model.

This study has some limitations that may limit the generalizability of the conclusions. First, the only *in vivo* nutrient uptake data presented are from murine tumor models. We provide supportive human TIF and flow cytometry data suggesting that glucose is not functionally scarce in the TME and that mTORC1 activity is high in human myeloid cells, but it would be logistically close to impossible to conduct the analogous ^{18}F studies for patients. Limited attempts at *ex vivo* FDG uptake in resected human kidney tumors were technically inconclusive.

It is possible that not all tumors will demonstrate the same pattern of glucose and glutamine uptake as demonstrated here. That is to be expected, however, in the model of nutrient partitioning. Cancer cells will be variably glycolytic based on their cellular program, which may

in turn influence the programs of other TME cells indirectly through signaling or, potentially, through competition for nutrients. The results of this study do not preclude the possibility of nutrient competition in TME with low concentration of nutrients, but allow for the development of a model whereby cell intrinsic factors are more important for nutrient uptake. Heterogeneity between human tumors is expected to be greater than those mouse models tested here.

This work does not show the direct contributions of myeloid cells to FDG PET imaging, although a natural hypothesis follows that myeloid cells significantly contribute to tumor FDG PET scans according to **Figure 2.16i**. Experimental attempts to selectively eliminate macrophages via intraperitoneal and intratumoral injection of liposomal clodronate were not successful. A clinical trial to prospectively compare paired FDG and ^{18}F-glutamine PET imaging in kidney cancer patients and correlate with surgical specimens is under consideration at Vanderbilt. We would hypothesize that ^{18}F-glutamine may be more sensitive for tumor than FDG, and that FDG signal would be associated with myeloid cell composition.

A potential systematic error which may challenge these findings is selection bias during tumor dissociation. These results rely on digesting tumors to single cell suspensions, and therefore may be losing/killing cancer cells that are the most FDG avid. This oversimplifies the tumor microenvironment and may be eliminating cells from areas of necrosis or that have concentrations of different cell subtypes. The data may only represent nutrient uptake in the most viable parts of tumors. While **Figure 2.1g-h** and **Figure 2.6** demonstrate spatial homogeneity in MC38 tumors, this will not be the case across all tumor types. or from necrotic zones. **Figure 2.3f-h** also argues against an error in impure cancer cells, but it is possible that even among a

"homogenous" cancer cell line more glycolytic cells are being lost based on spatial and/or non-genetic heterogeneity. Technical considerations for measuring *in vivo* ^{18}F-nutrient uptake including strengths and limitations are discussed in Chapter 3.

Another limitation for this work is the lack of specifically targeting the metabolic program of a single tumor cell type. Instead, there is a reliance on pharmacologic inhibitors that affect all TME cells. An important future direction will be to show that the metabolic program of a single cell subset alters its nutrient uptake independent of all other TME cell types. Alternatively, an intervention on one cell subtype may affect the uptake of other TME cells, suggesting direct (if nutrient concentration is limiting) or indirect (secondary to TME cell function altering other metabolic cell programs) nutrient competition.

In this chapter a model of cell-programmed nutrient partitioning in the TME was established. These results have potential implications for ^{18}F-nutrient PET tumor imaging and for therapies targeting metabolism in the TME. In Chapter 3, other tumor and inflammatory contexts are explored using ^{18}F-nutrient uptake.

CHAPTER 3: GLUCOSE UPTAKE IN OTHER TUMOR AND INFLAMMATORY CONTEXTS

The data in this chapter are unpublished.

Introduction

The methodology developed in Chapter 2 proved a powerful tool to measure *in vivo* nutrient uptake across different cell subsets. We tested other hypotheses about glucose and glutamine uptake across tumor and inflammatory contexts. The experiments highlighted in this chapter demonstrate the strengths and limitations of our approach to measuring *in vivo* nutrient uptake. They also provide preliminary data for future work in the field. Each experiment will be introduced in its respective section.

Validation of cellular FDG avidity across different cell numbers

In **Figure 2.3** we provided evidence that our method of FDG uptake truly measures glucose uptake *in vivo*. In **Figures 2.4-2.5**, we demonstrate that FDG uptake does not match 2NBDG staining, consistent with other reports casting doubt on the accuracy of 2NBDG as a glucose uptake-specific reporter (Sinclair et al 2020). An outstanding technical question not addressed on our manuscript is the ranges of live cells counted and counts per minute (CPM) over which our assay provides linear results. This is particularly important as we calculate cellular FDG uptake by dividing the radioactive CPM by number of live cells in each sample. Isolated tumor CD4/8+ and Other CD45+ lymphocyte fractions tend to yield fewer live cells than CD11b+ myeloid and CD45- cancer cell fractions. Differences in live cell yield between different tumors or between different tissues (spleen and tumor) may also hypothetically affect results.

To determine the range of live cells over which the *in vivo* FDG assay provides linear radioactive CPM, we dissociated *in vivo* labelled FDG-avid MC38 tumors, isolated myeloid, T cell, other immune cell, and cancer cell fractions, and serially diluted the cells to below the detectable range of CPM radioactivity (**Figure 3.1a**). Linear regression analysis demonstrated linearity along almost three orders of magnitude of cell count, from 20 million to 40,000 live cells. The slope of each line indicates cellular glucose avidity (CPM /million cells) and demonstrated the same FDG uptake phenotypes observed in Chapter 2: CD11b+ > CD4/8+ ~ CD45- (991 > 232 ~ 212 CPM/million cells). Notably, elevated myeloid FDG uptake held even up until the limit of detection of radioactivity at <100,000 cells, suggesting that the assay is valid at low cell numbers so long as radioactivity is significantly above background (average background plus two standard deviations above n=5 background measurements). However, linear regression analysis of live cell count versus cellular FDG avidity (**Figure 3.1b**) shows that lower cell counts may overestimate cellular FDG avidity. While this may be a limitation of our approach, the primary result of **Figure 2.3** is apparent with myeloid cell glucose uptake substantially greater than other cell populations. Additionally, the strength of the interaction appears weak over the range of cell numbers typically measured in an experiment (100,000 – 10 million), and would be incorporated in the variability of FDG avidity between biological replicates within an experiment.

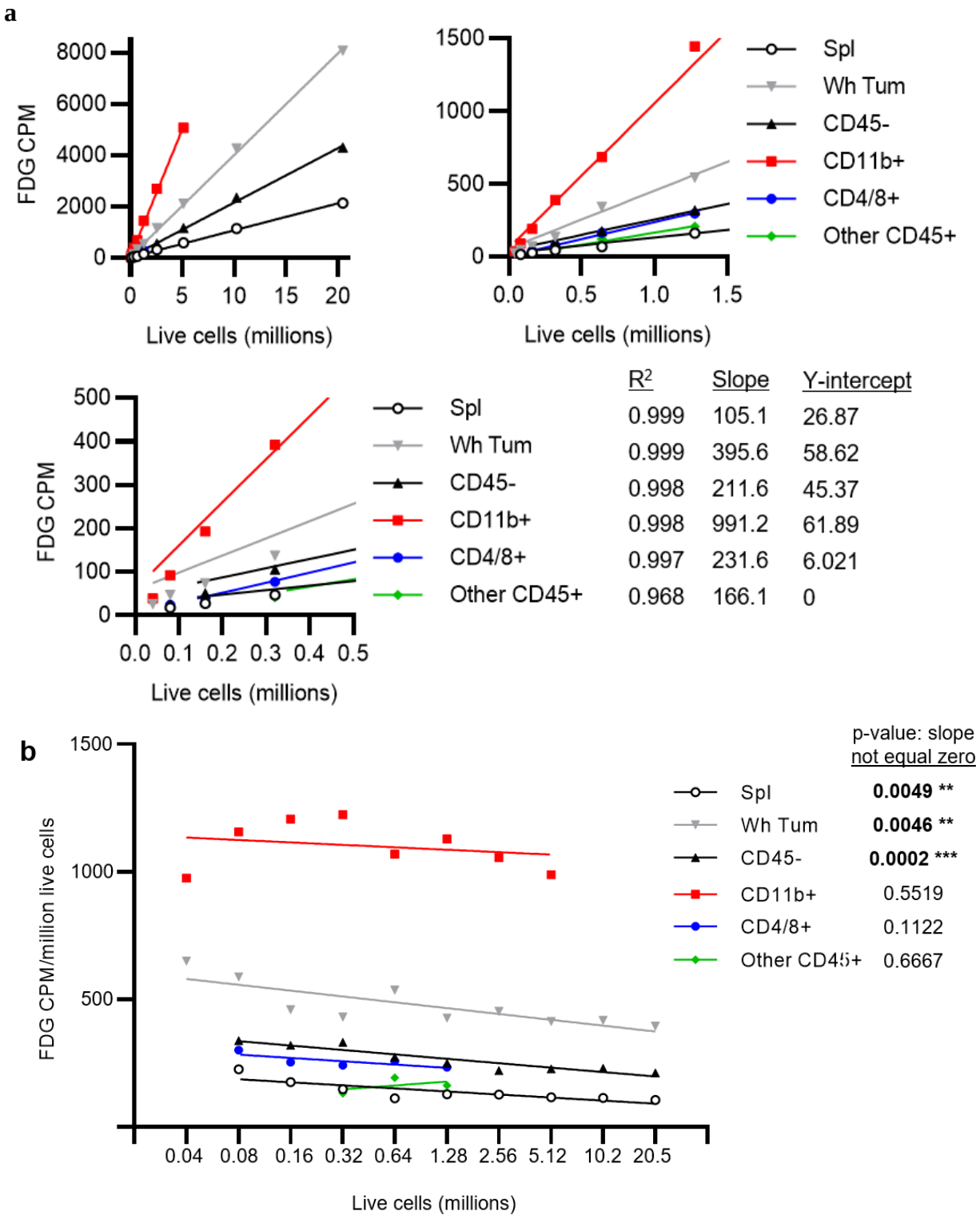

Figure 3.1: MC38 tumor cell FDG avidity across varied cell numbers. FDG-avid splenocytes, MC38 tumor cells, and microbead-isolated tumor cell populations were counted and serially two-fold diluted. (**a**) Linear regression for CPM vs. Live cells from the minimum cell number needed for signal above background (40,000 for CD11b+ and Whole Tumor, 80,000 live

cells for Spleen, CD45-, and CD4/8+, and 320,000 live cells for Other CD45+) to maximum yield or 20 million live cells. Plots of the same linear regression analysis are shown at different scales. (**b**) Linear regression for CPM/live cells vs. log2-transformed live cells. Data points are averages of technical duplicates pooled from n=5 mice.

Tumor FDG avidity normalization by total protein

Our primary readout for "cellular glucose uptake" is FDG counts per minute (CPM) divided by millions of live cells in the sample. We regularly checked FDG avidity normalized to millions of total cells, as well, to ensure that differences in viability between samples did not change the overall phenotype (**Figure 2.3c**). One additional consideration besides viability of the samples is the size of the cells. Larger cells, which we would expect in the tumor microenvironment to be cancer cells and myeloid cells, might be expected to have greater metabolic activity just based on biomass alone which would accentuate per-cell measurements. To control for differences in cell size, we normalized MC38 tumor FDG CPM signals to live cells, total cells, and total protein in each sample (**Figure 3.2**). In all cases, tumor CD11b+ myeloid cells demonstrated the highest FDG avidity, consistent with the primary conclusions from **Figure 2.8**.

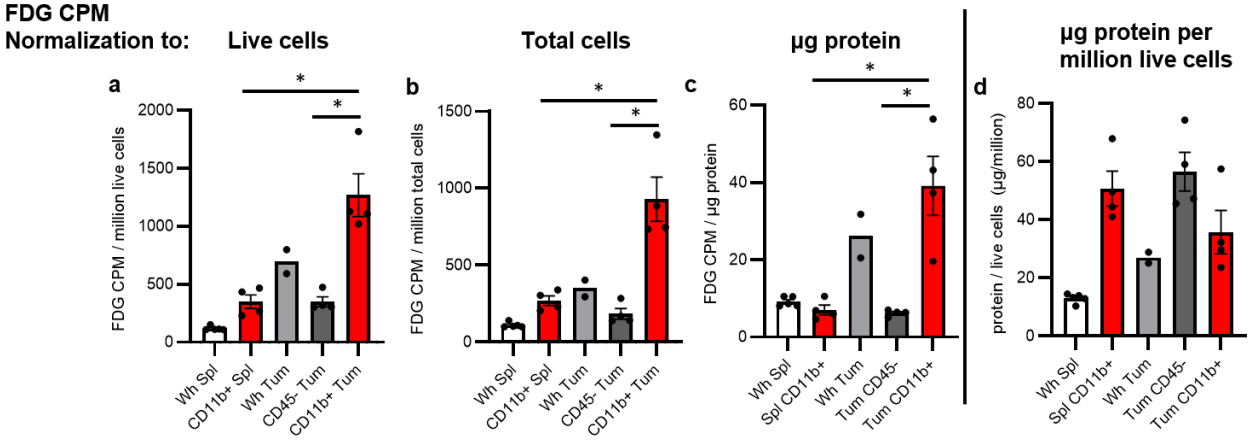

Figure 3.2: MC38 tumor cell FDG avidity normalized to total protein. a-c, Indicated spleen and MC38 tumor fraction FDG signal normalized to millions of live cells (**a**), millions of total cell (**b**), and total protein (**c**). **d**, Protein yield per million live cells. P-values indicate result of Welch's 2-tailed t-test (* $p<0.05$)

CD8 versus CD4 T cell glucose uptake in MC38 tumors

In **Figure 2.8**, we demonstrated that total T cell glucose uptake in the tumor microenvironment approximates cancer cell glucose uptake and exceeds the uptake of resting splenic T cells. The two predominant T cell subsets are cytotoxic CD8 and helper CD4 T cells, both of which are found in different proportions in TMEs (**Figure 2.7**). We sequentially isolated myeloid, CD8 T cell, CD4 T cell, and cancer cell fractions from FDG-avid MC38 tumors by using CD11b, CD8, CD4, and CD45 microbeads, respectively. Tumor CD8 and CD4 T cell fractions demonstrated similar glucose uptake, both greater than their respective splenic populations (**Figure 3.2a-d**). Tumor CD8 T cells expressed PD-1 and TIM3 consistent with an exhaustion phenotype, whereas CD4 T cells were predominately regulatory T cells expressing FOXP3 (**Figure 2.13**, **Figure 3.2e**). It is remarkable here that, despite having phenotypes associated with reduced glycolytic metabolism, both CD8 and CD4 T cells show elevated glucose uptake compared to splenic counterparts.

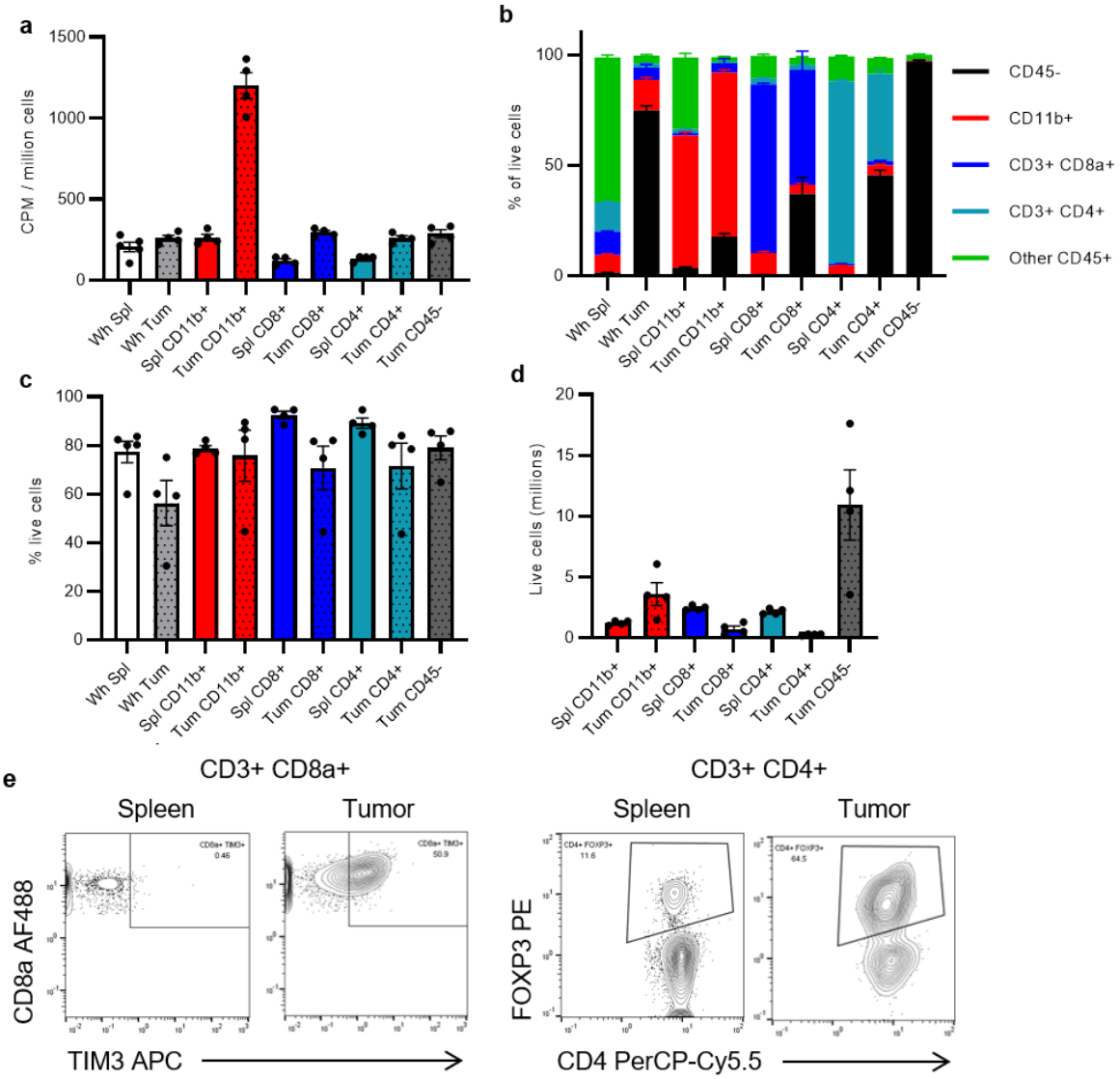

Figure 3.3: CD8 and CD4 T cell FDG uptake in MC38 tumors are similar. Cellular FDG avidity (**a**), cellular composition (**b**), viability (**c**), and live cell yield (**d**) of designated cell fractions in spleen and tumor (n=4-5 mice). **e**, Representative flow cytometry analysis in CD8 and CD4 T cells from tumor and spleen.

Cellular glucose and glutamine uptake with anti-PD-1 immunotherapy in MC38 tumors

The intersection of immune cell metabolism and cancer immunotherapy is described in Chapter 1. PD-1 inhibitory signaling reduces anabolic metabolism in T cells (Schildberg et al 2016). Therefore, we hypothesized that anti-PD-1 immunotherapy would specifically reduce glucose uptake in T cells in the TME. We treated mice bearing subcutaneous MC38 tumors with control

IgG or anti-PD-1 therapy for 5 days prior to analyzing *in vivo* FDG and ^{18}F-glutamine uptake. Anti-PD-1 antibody treatment blocked fluorescent anti-PD-1 antibody staining on tumor T cells but did not have an effect on final tumor size at the timepoints analyzed (**Figure 3.3a-b**). No significant effect on glucose uptake was observed across TME cell populations (**Figure 3.3c**). ^{18}F-glutamine showed a trend toward reduced uptake across tumor populations, particularly in T cells (**Figure 3.3d**). A limitation to these experiments was that the clone of MC38 cell lines used was subsequently shown to not be sensitive to anti-PD-1 therapy. Subsequent experiments in an MC38 clone directly obtained from a vendor and shown to be sensitive to anti-PD-1 at later timepoints also demonstrated no difference in glucose uptake in the TME (**Figure 3.3e-f**).

The absence of a change in glucose uptake was unexpected, given PD-1's direct inhibitory effect on signaling upstream of glycolytic programming. It is possible that our method is not sufficiently sensitive or precise to detect the hypothesized increase in FDG signal. Biologically, it is also possible that the most significant T cells responding to anti-PD-1 are in secondary lymphoid organs. The non-significant decrease in glutamine uptake would need to be repeated in future experiments but may be of interest as pharmacologic inhibition of glutamine metabolism particularly in T cells has been associated with improved tumor control (Leone et al 2019).

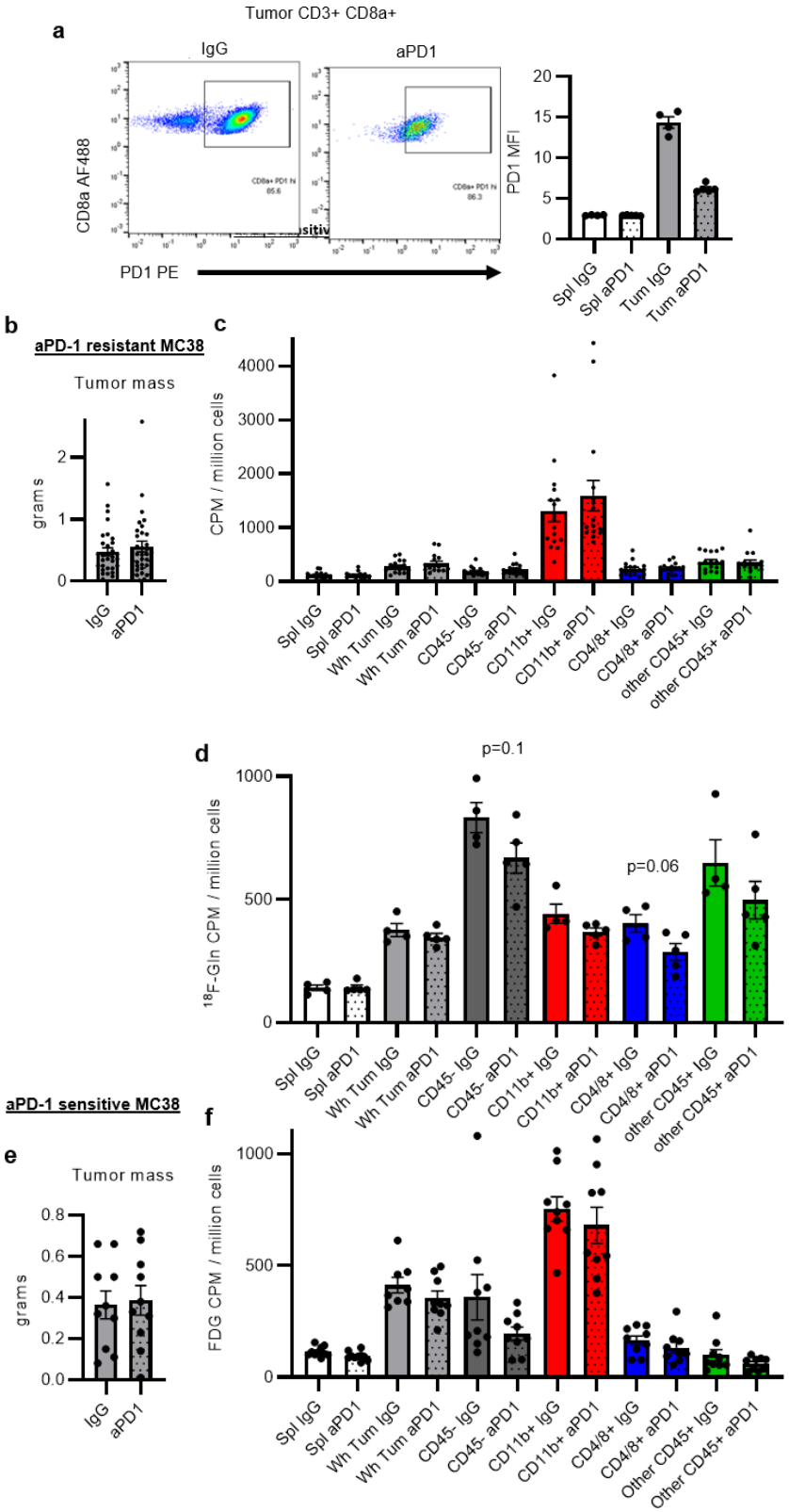

Figure 3.4: Effect of anti-PD-1 on MC38 tumor glucose and glutamine uptake. **a**, Representative PD-1 flow cytometry staining on tumor CD8 T cells with *in vivo* IgG and anti-PD-1 treatment. **b-c,** Effect of anti-PD-1 treatment on final tumor mass (**b**) and cellular FDG

uptake (**c**) in MC38 tumor resistant to anti-PD-1 treatment (n=15-20 mice from 4 independent experiments). **e-f**, Effect of anti-PD-1 treatment on final tumor mass (**e**) and cellular FDG uptake (**f**) in MC38 tumors sensitive to anti-PD-1 treatment (n=10 mice from 2 independent experiments). P-values indicate result of Welch's 2-tailed t-test.

Cellular glucose uptake with anti-CTLA4 immunotherapy in MC38 tumors

CTLA4 signaling directly inhibits CD28 costimulatory signals in T cells, thereby reducing PI3K/Akt/mTORC1-mediated anabolic metabolism and glycolysis. We therefore hypothesized that anti-CTLA4 treatment would increase FDG uptake in T cells. Anti-CTLA4 had no effect on tumor mass but did deplete intratumor Treg, a known effect of the anti-CTLA4 antibody used in mice (**Figure 3.4a-b**). Anti-CTLA4 treatment had no effect on glucose uptake across MC38 tumor cell populations. Like the results using anti-PD-1, it is possible that our method for measuring glucose uptake is not sufficiently sensitive or precise to detect the hypothesized increase in FDG signal. Alternatively, we may not have used an appropriate tumor model to detect the effect of anti-CTLA4 or we are not isolating specific cell populations affected by treatment. It is intriguing to note that glucose uptake across cell types was not affected by the depletion in tumor Treg, but depletion by another method would be necessary to confirm.

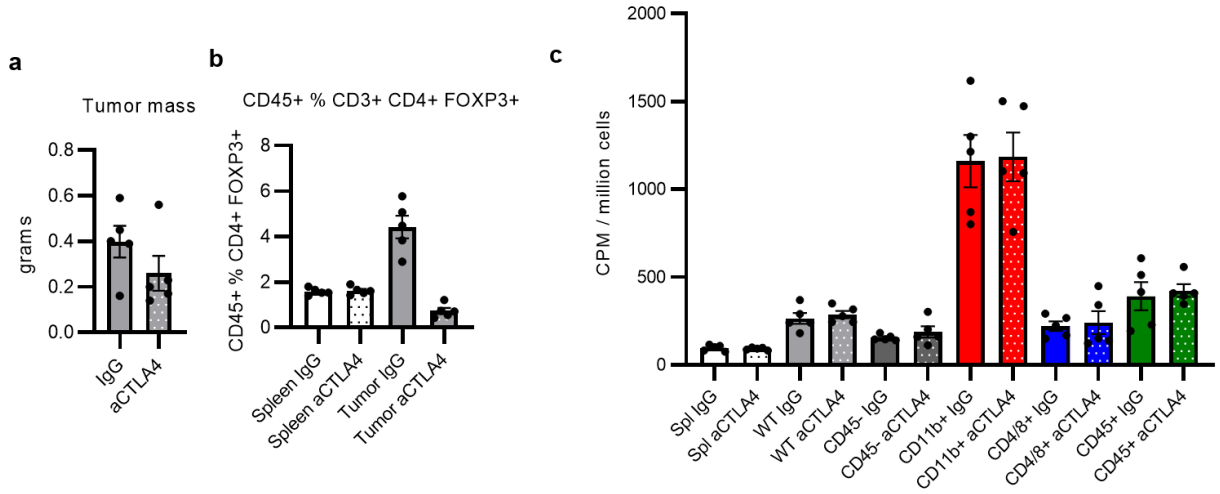

Figure 3.5: Effect of anti-CTLA4 on MC38 tumor glucose uptake. **a**, Final tumor mass after treatment with IgG of anti-CTLA4 antibodies. **b,** Relative abundance of Treg in spleen and

tumor with IgG of anti-CTLA4 antibodies. **c,** Effect of anti-CTLA4 treatment cellular FDG uptake (n=5 mice).

Cellular glucose uptake with STING agonism in MC38 tumors

The innate immune STING pathway recognizes cytoplasmic DNA and activates NFkB and type I interferon signaling. Agonism of STING is under investigation as a form of cancer immunotherapy (Flood et al 2019). We hypothesized that tumor treatment with intratumoral injection of STING agonist ADU-S100 would promote more effector anti-tumor phenotypes in tumor immune cells associated with increased glucose uptake. Four days after starting treatment, STING agonism did not change tumor size but did alter the immune infiltrate of tumor, including relatively fewer Treg and more CD11b^{+} Ly6C^{hi} monocytic myeloid-derived suppressor cells (M-MDSC) (**Figure 3.5a-c**). There was no change in glucose uptake across tumor cell populations (**Figure 3.5d**). We are limited in our ability to make conclusions based on this null result as noted in the anti-PD-1 and anti-CTLA4 experiments.

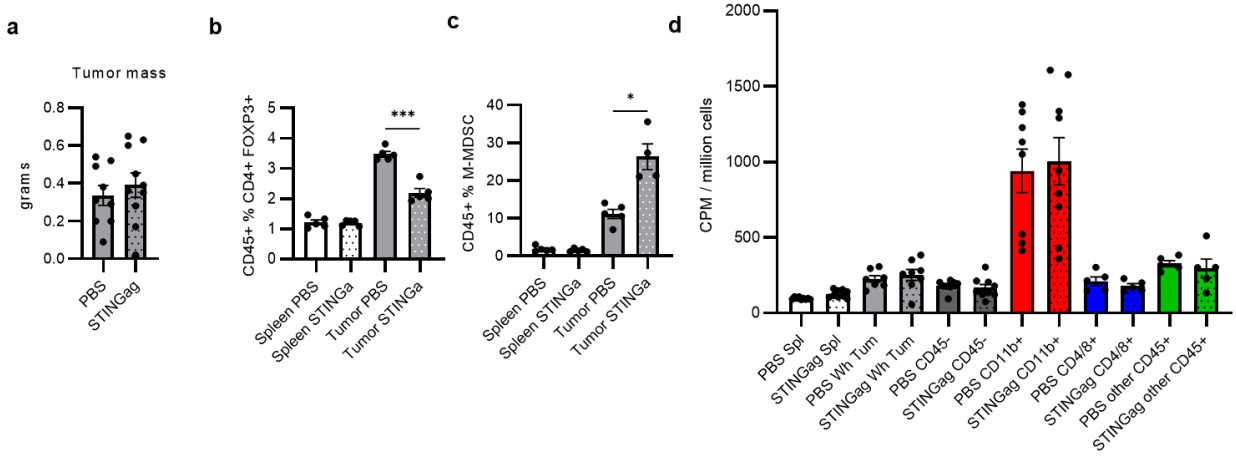

Figure 3.6: Effect of intratumoral STING agonist on MC38 tumor glucose uptake. **a**, Final tumor mass after treatment with intratumoral PBS or STING agonist. **b-c,** Relative abundance of Treg and M-MDSC in spleen and tumor with intratumoral PBS or STING agonist. **d,** Effect of intratumoral STING agonism treatment cellular FDG uptake (n=10 mice). Data merged from two independent experiments. P-values indicate result of Welch's 2-tailed t-test (* $p<0.05$, *** $p<0.001$).

Cellular glucose uptake with PI3Kγ/δ inhibition in MC38 tumors

PI3K signaling promotes mTORC1 activity and anabolic metabolism. PI3Kγ and PI3Kδ are catalytic subunits specifically expressed in leukocytes (Okkenhaug 2013). We hypothesized that IPI-145 (Duvelisib), a PI3Kγ/δ-selective inhibitor (Davis et al 2017), would specifically decrease glucose uptake in tumor infiltrating immune cells. Treatment of MC38-tumor bearing mice for five days reduced splenic lymphocyte pS6 and Ki67 levels, but did not change these markers in tumor cell populations (**Figure 3.6 a-b**). There was also no change in final tumor mass (**Figure 3.6c**). Glucose uptake in the tumor microenvironment was not altered, although there was a trend toward reduced glucose uptake in splenocytes (**Figure 3.6d**). It is possible that the treatment failed to reach tumor resident cells, or that a higher dose would be required to inhibit downstream mTORC1 signaling and proliferation.

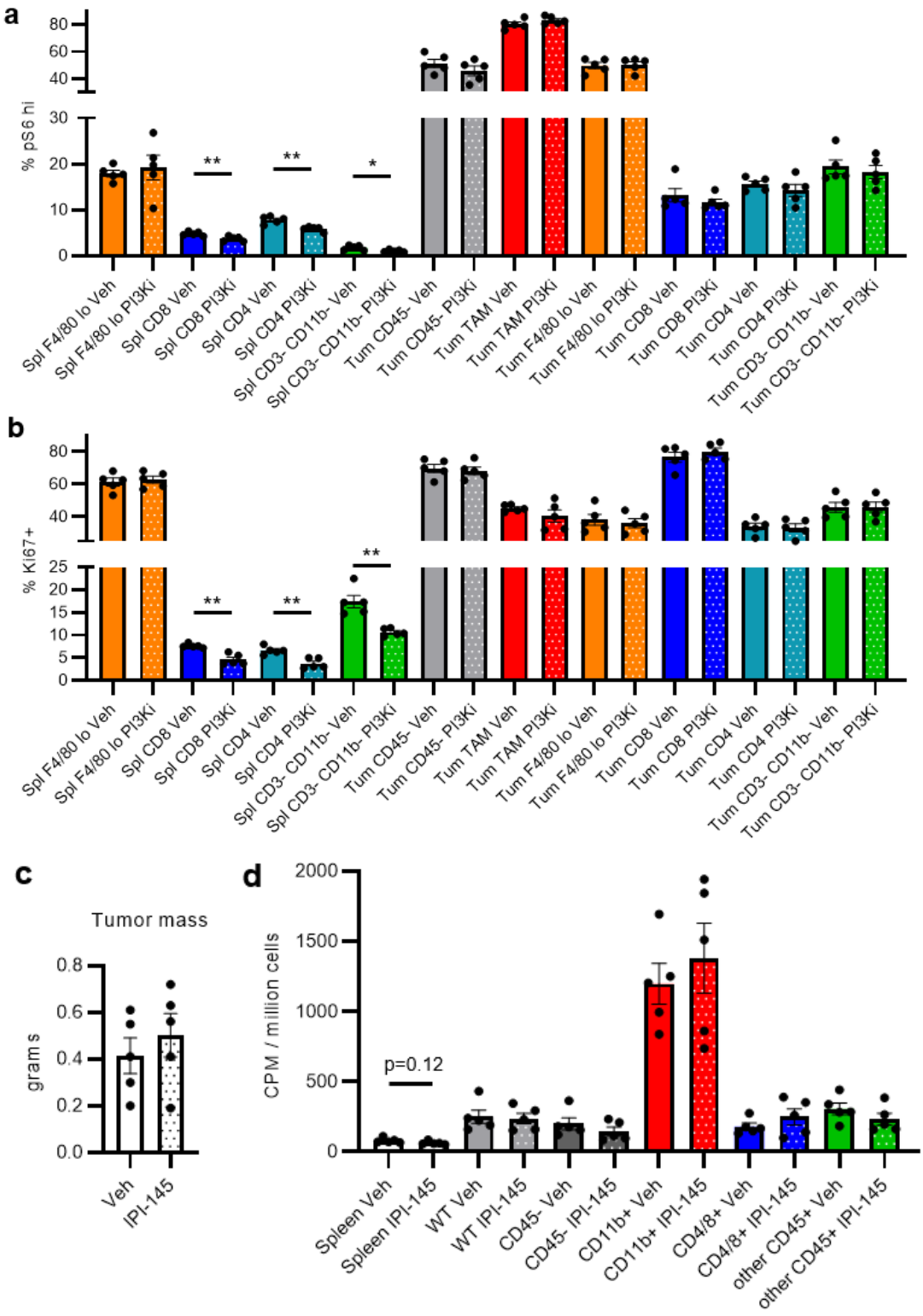

Figure 3.7: Effect of PI3Kγ/δ inhibitor IPI-145 on MC38 tumor glucose uptake. **a-b,** pS6 (**a**) and Ki67 (**b**) levels in indicated spleen and tumor cell populations. **c,** Final tumor masses. **d,** Cellular FDG avidity in indicated cell populations (n=5 mice). P-values indicate result of Welch's 2-tailed t-test (* $p<0.05$, ** $p<0.01$).

Cellular glucose uptake in T cells with exogenous expression of GLUT1

The glucose transporter GLUT1 is upregulated during immune cell activation and supports glycolytic programming for effector T cell function (Macintyre & Garriets et al 2014). We hypothesized that overexpression of GLUT1 in T cells would increase glucose uptake in the tumor microenvironment. We implanted tumors in transgenic mice with exogenous GLUT1 expression driven by the Lck promotor, such that only T cells have enhanced GLUT1 levels (Zhao et al 2007). Flow cytometry analysis of GLUT1 demonstrated elevated GLUT1 specifically in splenic CD8 and CD4 T cells and tumor CD4 T cells, but not tumor CD8 T cells. The basal expression of GLUT1 in WT CD8 T cells approximated the splenic expression of GLUT1 in transgenic CD8 T cells (**Figure 3.7a**). There was no difference in tumor size in wild type and GLUT1 transgenic animals (**Figure 3.7b**). Cellular FDG uptake was not significantly different in tumor T cells, although splenocytes demonstrated a significant increase in glucose uptake consistent with exogenous GLUT1 in T cells which account for approximately one quarter of total splenocytes (**Figure 3.7c**). There was no difference in the abundance of CD8, CD4 Tconv, or CD4 Treg in spleen and tumor from wild type and GLUT1 transgenic animals (**Figure 3.7d**). Tumor GLUT1 transgenic CD8 expressed less PD1 and TIM3, although similar CD44 and CD69, consistent with a less terminally differentiated tumor resident phenotype (**Figure 3.7e**). However, only GLUT1 transgenic spleen CD8 and spleen and tumor CD4, not tumor CD8, expressed more IFNγ on *ex vivo* stimulation, such that GLUT1 expression was associated with IFNg production (**Figure 3.7f**).

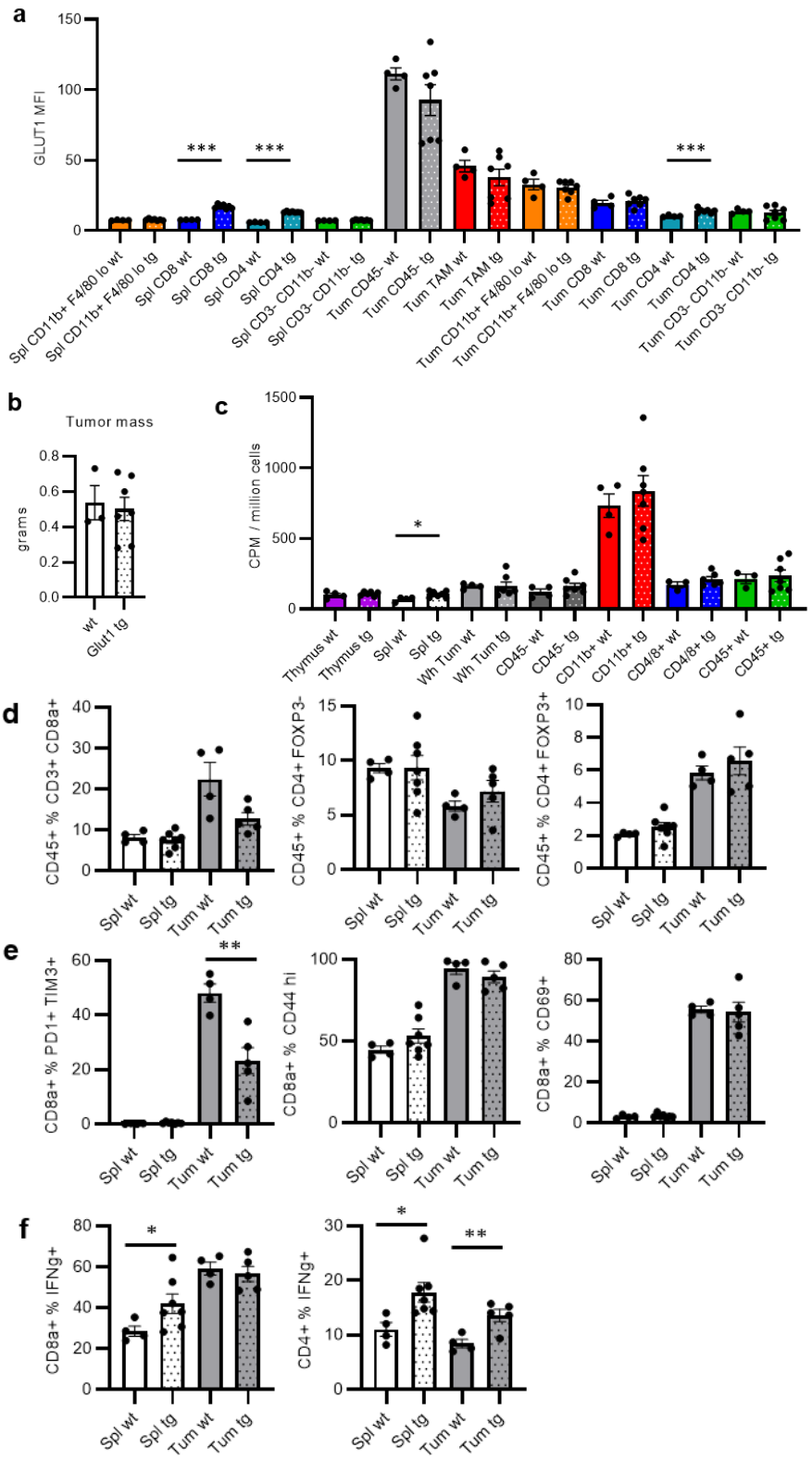

Figure 3.8: Effect of transgenic expression of GLUT1 in T cells on splenic and MC38 tumor glucose uptake. **a-b,** GLUT1 levels in indicated spleen and tumor cell populations. **b,** Final tumor masses. **c,** Cellular FDG avidity in indicated cell populations (n=4 WT mice, n=7 Glut1

Tg mice). **d**, Relative abundance of CD8, CD4 Tconv, and CD4 Treg cells. **e**, Surface marker immunophenotypes of CD8 T cells. **f**, IFNg production of CD8 and CD4 T cells. P-values indicate result of Welch's 2-tailed t-test (* $p<0.05$, ** $p<0.01$).

Cellular glucose uptake with exogenous myeloid-specific NFκB signaling

NFκB signaling drives immune cell differentiation and effector functions. We hypothesized that activation of NFκB would drive immune cell glucose uptake across different tissue types. To test this hypothesis, we employed a model with transgenic monocyte-macrophage-specific NFκB activation, whereby a constitutively activated form of IKK2 (cIKK2) is expressed under the control of colony stimulating factor receptor 1 promotor (Connelly et al 2011, Hoover & Hufnagel et al 2020). MC38 tumors obtained similar sizes after seven days of cIKK2 induction (**Figure 3.9a**). The total number of bone marrow cells collected from cIKK2 mice was significantly decreased compared to controls (**Figure 3.9b**), consistent with results showing that cIKK2 expression under the Vav promotor causes terminal differentiation of hematopoietic stem cells (Nakagawa et al 2018, Nakagawa & Rathinam 2018). While overall CD11b+ myeloid cell frequencies did not change in bone marrow, spleen, and tumor, the overall Ly6G+ neutrophil contribution decreased (**Figure 3.9c-d**), potentially suggesting favored monocytic differentiation. The overall frequency of CD11b+ Ly6G- monocytic cell subsets changed in the bone marrow, spleen, and tumor compartments, with seemingly enhanced macrophage differentiation in tumors (**Figure 3.9e-f**). Surprisingly, *in vivo* cellular FDG uptake was not altered in MC38 tumors, but was 4.3-fold greater in whole splenocytes and 16-fold greater in bone marrow cells from cIKK2 mice (**Figure 3.9g**). Future work may focus on uncovering which cells specifically uptake glucose in the bone marrow and periphery and how blocking glucose uptake or glycolysis affects cIKK2-induced myelopoiesis.

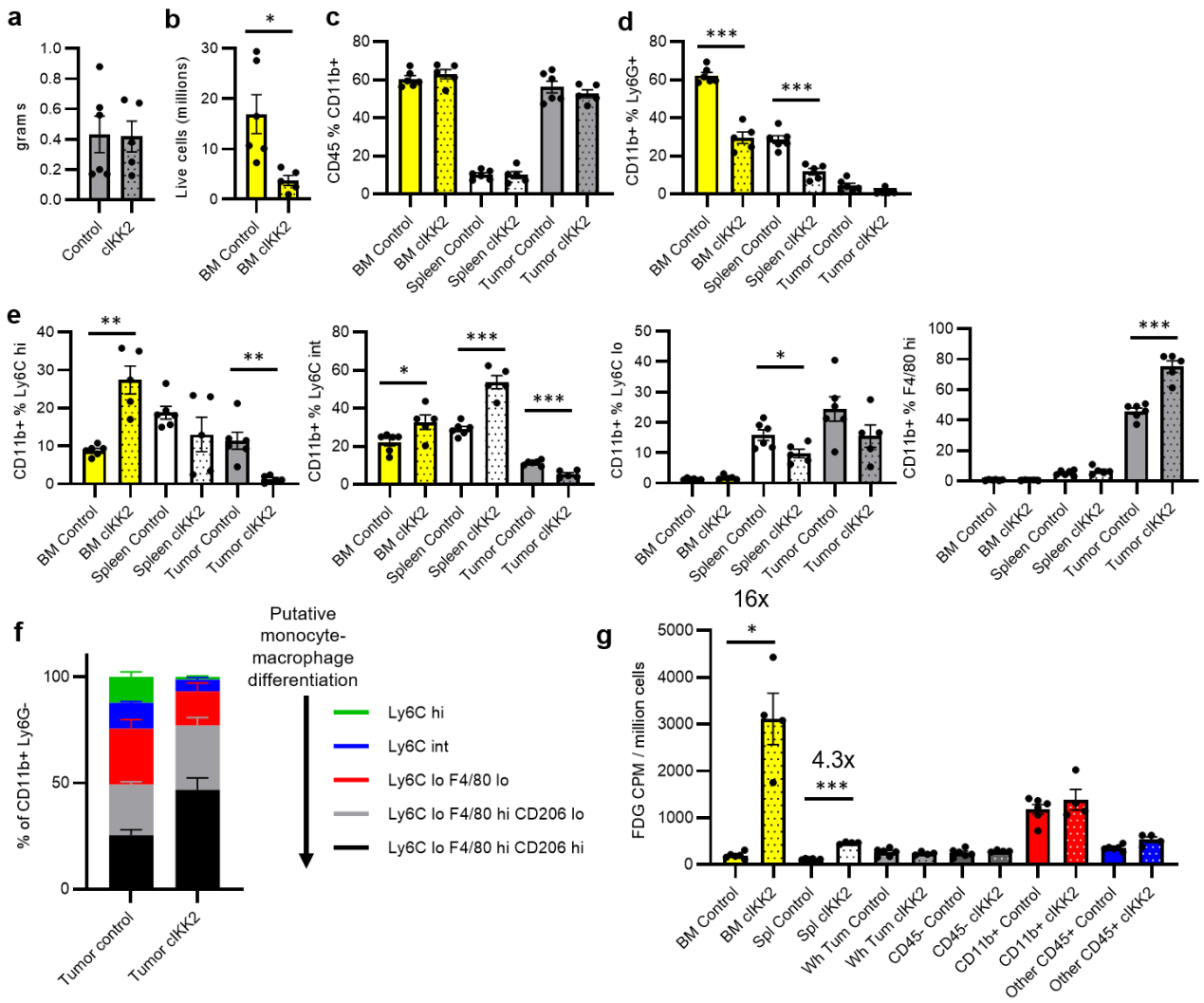

Figure 3.9: Effect of transgenic constitutive activation of NFκB signaling in monocytic cells on bone marrow, spleen, and MC38 tumor glucose uptake. **a,** Final tumor mass. **b,** Live cell yield from bone marrow. **c**, Total myeloid cell composition of immune cell compartment. **d**, Total neutrophilic cell composition of myeloid cell compartment. **e**, Total monocytic-macrophage compositions of myeloid cell compartment. **f**, MC38 tumor monocyte-macrophage composition according to Ly6C, F4/80, and CD206 expression. **g**, Cellular FDG uptake in bone marrow, spleen, and indicated MC38 tumor cell populations. n=6 control mice, n=5 cIKK2 transgenic mice. P-values indicate result of Welch's 2-tailed t-test (* $p<0.05$, ** $p<0.01$, ***$p<0.001$).

Cellular glucose uptake in inflamed lung

Activated immune cells in across diverse inflammatory contexts and tissues upregulate glucose metabolism. We hypothesized that myeloid cells may be the greatest major consumers of glucose in situations other than cancer. A recent study demonstrated that microglia, the resident

macrophages of the brain, uptake more glucose than other brain parenchymal neurons and astrocytes (Xiang et al 2021). We induced allergic lung inflammation in mice through intranasal sensitization with Alternaria extract for 10 days prior to measure *in vivo* FDG uptake in dissociated lung cells (**Figure 3.10a-c**). Isolated CD11b+ myeloid cells had significantly higher FDG avidity than CD4 and other CD45 microbead-isolated cell fractions (**Figure 3.10d**). The magnitude difference in glucose uptake is likely greater than was measured due to myeloid cell contamination of CD4 and other CD45 cell fractions (**Figure 3.10c**).

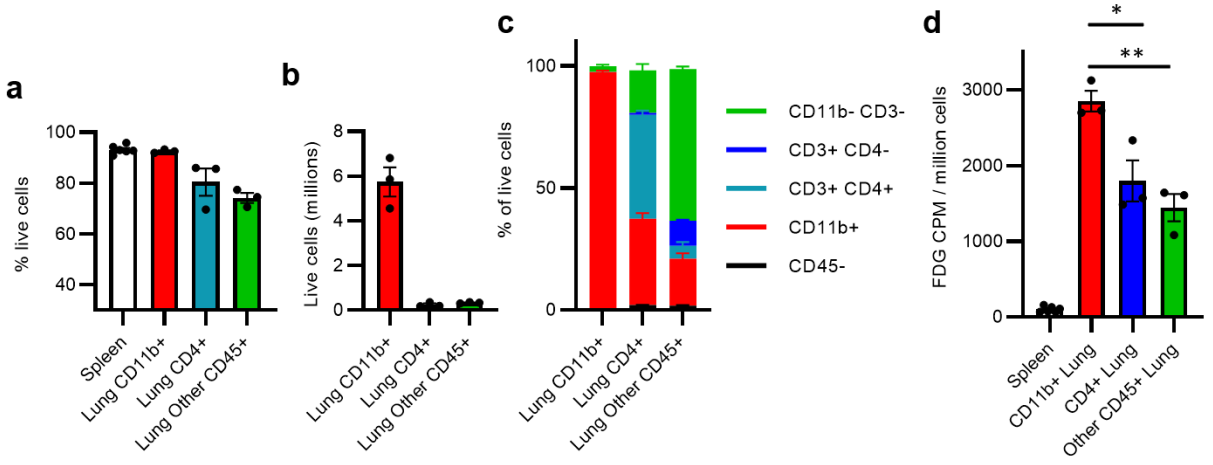

Figure 3.10: Cellular glucose uptake in Alternaria-sensitized inflamed lung. a, Cell viability of inflamed lung. **b,** Live cell yield from inflamed lung fractions. **c**, Cell composition microbead-isolated lung fractions. **d**, Cellular FDG uptake in spleen and inflamed lung cell fractions. n=3 mice for fractions, n=6 mice for spleens. P-values indicate result of Welch's 2-tailed t-test (* $p<0.05$, ** $p<0.01$).

Discussion

Our approach to measuring ^{18}F-nutrient uptake has many notable strengths. The most important aspect was the ability to measure cell type-specific nutrient uptake as opposed to bulk tumor metabolism. This simple approach to tumor metabolism allowed us to test the paradigm of cancer cell-dominant glucose uptake. While fluorescent analogs delivered *in vivo* are logistically appealing and permit single cell analysis by flow cytometry, we demonstrated that glucose

analog 2NBDG does not have the same uptake pattern as FDG, in agreement with other recent work (Sinclair et al 2020). FDG is a glucose molecule with a single hydroxyl group replaced with ^{18}F, whereas 2NBDG incorporates a nitrobenzofurazan fluorophore which is itself bulkier than glucose and likely accounts for its different net uptake behavior *in vivo*. FDG also has the added appeal of being broadly clinically utilized in oncology. The molar dose of FDG is minute compared to circulating glucose, meaning that FDG is non-saturating and systemic metabolism is unaltered by the assay (Kohl et al 2021).

There are numerous technical limitations in our assay that merit caution. In terms of accuracy, **Figure 3.1** shows that, at low isolated cell numbers, the calculated FDG avidity may be overestimated. This could be a result of accuracy of the cell count, or less likely an artifact of the experiment in Figure 3.1. The use of antibodies bound to magnetic microbeads permits processing of multiple samples side by side with high cell yields. However, the degree of enrichment is approximately ten-fold, so rare cell populations are difficult to purify. **Figure 2.9i** demonstrates tumor cDC enrichment less than plurality, although the degree of enrichment combined with low background cancer cell FDG uptake strengthened our decision to conclude that cDC have higher glucose uptake than cancer cells. In other contexts, low purity may reduce differences between samples, as in **Figure 3.10**, or reduce the confidence of our conclusions, as in **Figure 3.3**. Overall, antibodies bound to magnetic microbeads have proven a powerful approach, but they require a cell population approximately 10% of total live cells and themselves need to have specific binding.

Multiple sources of variability affect the precision of our assay. An initial source of variability is the dose ^{18}F injected into the mouse, although this can be easily corrected by measuring the precise dose at the time of injection. Another source of variability may be the glucose metabolic state of the mouse. Our mice were fed *ad labitum* prior to cellular ^{18}F-nutrient assays, and it is possible that overnight fasting may have helped normalized serum glucose levels. Similarly, differences in mouse mass, adiposity, and sex could lead to both technical and biologic variation that should be considered in future experiments. In the TME, differential vascularization may produce different total FDG delivery to tumor cells, necessitating paired analyses if possible. Differences in fraction purity between like samples can vastly effect FDG signal. It is necessary to confirm fraction purity in every isolated sample. A potentially large source of variability is uncertainty in cell counts using an automated cell counter with trypan. Finally, normalization of radioactivity to time of injection is possible and reduces variability to a limited extent.

Future Directions

Major questions in tumor metabolism and immunometabolism are directly testable using ^{18}F-nutrient uptake. In tumors, it will be interesting to test mediators of cell type-specific nutrient uptake, following up from Chapter 2. Ongoing and future experiments will test the role of cancer cell-specific VHL and myeloid cell-specific HK3 knockout on TME glucose uptake. Additionally, responses to immunotherapy and metabolism-targeted therapy may lead to key insights on basic mechanisms of action on distinct cell subsets. We should not over conclude from the null results in **Figures 3.4-3.7**, as the effect of immune-targeted therapies are likely to be tumor type-, tissue-, and time-dependent. We measured orthotopic and subcutaneous Renca

tumor glucose uptake, but a more relevant comparison will be measuring how metabolic programs change from primary to metastatic sites.

For immunometabolism, **Figures 3.9-3.10** demonstrate exciting initial results continuing to probe myeloid cell glucose metabolism in non-cancer contexts. Do different tissue and inflammatory microenvironments confer cell-selective nutrient uptake? We may hypothesize that myeloid cells are always uniquely poised to uptake glucose across tissue microenvironments based on their cellular metabolic program. For T cell metabolism, comparing the *in vivo* nutrient uptake antigen-specific naive CD8 T cells, effector CD8 cells responding to acute infection, memory CD8 cells, and exhausted CD8 cells responding to chronic infection or tumors. It will also be important to measure antigen specific-cells in both lymphoid tissue and inflamed tissue/tumors. Analogous experiments for different effector CD4 subsets could also be performed. Thy1.1 microbeads have worked well for antigen-specific T cell isolation, and if technically necessary Rag KO mice could also be utilized to enhance T cell purity.

In this dissertation we interrogated *in vivo* glucose and glutamine uptake with ^{18}F probes, and *ex vivo* palmitate uptake with a fluorescent probe. Many nutrients can be synthesized as ^{18}F tracers. Most important in the tumor context of our work may be lactate. ^{18}F tracers may not be perfect indicators of uptake, however, as they can be further metabolized and effluxed out of cells. FDG is a dead-end tracer which, after being phosphorylated, is not further metabolized.

The use of flow sorting for more specific cell subsets will be necessary to move beyond magnetic bead isolations. Magnetic beads essentially limit analyses to a single cell surface marker sorted

sequentially. Use of a flow sorter combined with logistically optimized tissue processing and radiation measurement will permit more accurate and specific conclusions regarding how particular cells partition nutrients in tissue microenvironments.

CHAPTER 4: GLUTAMINE DETERMINES EARLY CD8 T CELL DIFFERENTIATION TRAJECTORY

Data from Figure 4.1 were adapted from the following manuscript originally published in *Immunity*:

Levine, L. S., Hiam-Galvez, K. J., Marquez, D. M., Tenvooren, I., Madden, M. Z., Contreras, D. C., ... & Spitzer, M. H. (2021). Single-cell analysis by mass cytometry reveals metabolic states of early-activated CD8+ T cells during the primary immune response. Immunity, 54(4), 829-844.

All other data are unpublished.

Introduction

In Chapter 2 and 3 we explored how different cell types uptake nutrients, particularly in the TME. Our analysis of how cells differentially utilized the nutrients and how they determine cell function was limited. Here, we explore the role of glutamine in CD8 T cell differentiation and anti-tumor function. There is increasing interest in glutamine-targeting therapeutics in cancer, and understanding how these molecules impact T cell fate is important to holistically evaluate consequences *in vivo* (Wise & Thompson 2010, Lemberg et al 2022).

Overall, previous studies have shown that glutamine promotes effector T cell function, but precise mechanisms and targets for optimal glutamine inhibition remain unclear. Glutamine uptake increases during T cell activation supported by a transcriptional program that broadly promotes glutaminolysis (Wang et al 2011). T cell activation in the absence of glutamine

decreases cell blasting and proliferation, although TCR signaling and activation marker upregulation remain intact, consistent with its classification as a conditionally essential amino acid for proliferating cells (Carr et al 2010). Apart from affecting T cell activation, alterations to glutamine metabolism alter T cell differentiation. Different perturbations of glutamine metabolism have distinct effects on CD4 T cell fate. *In vitro* differentiation of CD4 cells in media without glutamine promoted iTreg differentiation, in a manner dependent on reduced α-ketoglutarate downstream of glutamine (Klysz et al 2015). Correspondingly, inhibition of GOT1 reduces α-ketoglutarate to promoted iTreg over Th17 differentiation (Xu et al 2017). Deficiency of glutamine transporter ASCT2 (*Slc1a5* KO) decreased Th1 and Th17 CD4 differentiation *in vitro* and attenuated models of T cell-dependent bowel and neuro-inflammation *in vivo* but had no effect on iTreg (Nakaya et al 2014). Inhibition or deficiency of Glutaminase (GLS) decreased Th17 differentiation *in vitro* and attenuated models of skin, lung, and bowel inflammation *in vivo* (Xia et al 2020) but promoted Th1 differentiation (Johnson et al 2018).

Diverse mechanisms have been proposed for the differential effects of glutamine perturbations. The regulation of reactive oxygen species through glutathione production is linked to GLS-dependent Th17 differentiation (Johnson et al 2018). Altered epigenetics from the availability of α-ketoglutarate for the function of epigenetic modifying enzymes also affects Th17 and Th1 fates (Chisolm et al 2017, Johnson et al 2018). Glutamine is important for the synthesis and transport of other amino acids. Glutamine is effluxed during the cotransport influx of branched chain amino acids. T cells with deficiency of large neutral amino acid transporter LAT1 (*Slc7a5* fl/fl CD4-Cre) demonstrated a marked failure to proliferate and gain effector function, partially dependent on the presence of glutamine for cotransport (Sinclair et al 2013).

Cytotoxic CD8 T cells are critical mediators of anti-tumor immunity. Precise roles for glutamine in CD8 T cell differentiation and function are unclear. As outlined in Chapter 1, there is substantial evidence that blocking anabolic pathways in tumor-specific CD8 T cells during *in vitro* expansion prior to adoptive transfer promotes a stem-like phenotype which enhances anti-tumor activity *in vivo* (Kishton et al 2017). When tumor specific T cells were activated in conditions depleted of glutamine, with pan-glutamine inhibition by small molecule DON (6-Diazo-5-oxo-L-norleucine), or with inhibitors of the conversion of glutamate to α-ketoglutarate, tumor growth was better controlled than under control conditions. T cells activated with depleted glutamine also demonstrated enhanced oxidative and glycolytic metabolism, enhanced cytotoxicity, and increased markers of stem-like differentiation (Nabe et al 2018). Correspondingly, GLS inhibition with small molecule CB839 enhanced Th1 and CD8 effector differentiation and promoted CAR T cell persistence *in vivo* and effector function *in vitro* (Johnson et al 2018). CB839 treatment *in vivo* also enhanced adoptive cell therapy and immune checkpoint blockade therapies (Varghese & Pramanik et al 2021). *In vivo* treatment with a DON derivative promoted anti-tumor CD8 activity associated with enhanced anabolic flux. Strikingly, DON treatment of cancer cells had an reverse effect, causing reduced growth and upregulated catabolic metabolism (Leone et al 2019).

Here, we hypothesized that specific targeting of glutamine metabolism through inhibition of GLS with CB839 would have a distinct effect from pan-glutamine blockade with DON or depletion of glutamine. Both CB839 and DON are being developed for applications in oncology. DON is a glutamine-analog which competitively and irreversibly inhibits a large number of

glutamine-using enzymes, some of which may be beneficial and some detrimental to effector T cell differentiation and function (Ahluwalia et al 1990). Consistent with its broad pharmacologic targets, it has been shown to have limiting toxicities in people (Lemberg et al 2022). We show that treatment of CD8 T cells with DON during the first 48hr of activation has a detrimental effect on T cell persistence *in vivo*. These differences are driven by distinct transcriptomic, epigenetic, and metabolic differentiation trajectories. Ultimately, DON-treated CD8 T cells fail to control tumor growth as well as control or CB839-treated T cells, suggesting caution on its use with adoptive cell therapies which may be secondary to inhibition of additional glutamine-related targets besides GLS.

Patient CAR T cells demonstrate metabolic differentiation trajectory *in vivo*

We first examined the expression of key metabolic markers by mass cytometry in CAR T cells from the peripheral blood of patients with B cell lymphoma. Consistent with metabolic differentiation over time, CD8 CAR T cells initially expressed high levels of multiple metabolism-related proteins. Over multiple weeks post infusion, these markers decrease except for fatty acid oxidation enzyme CPT1a (**Figure 4.1**). This result is consistent with fatty acid catabolism being important for persisting memory T cell survival (Pearce et al 2009).

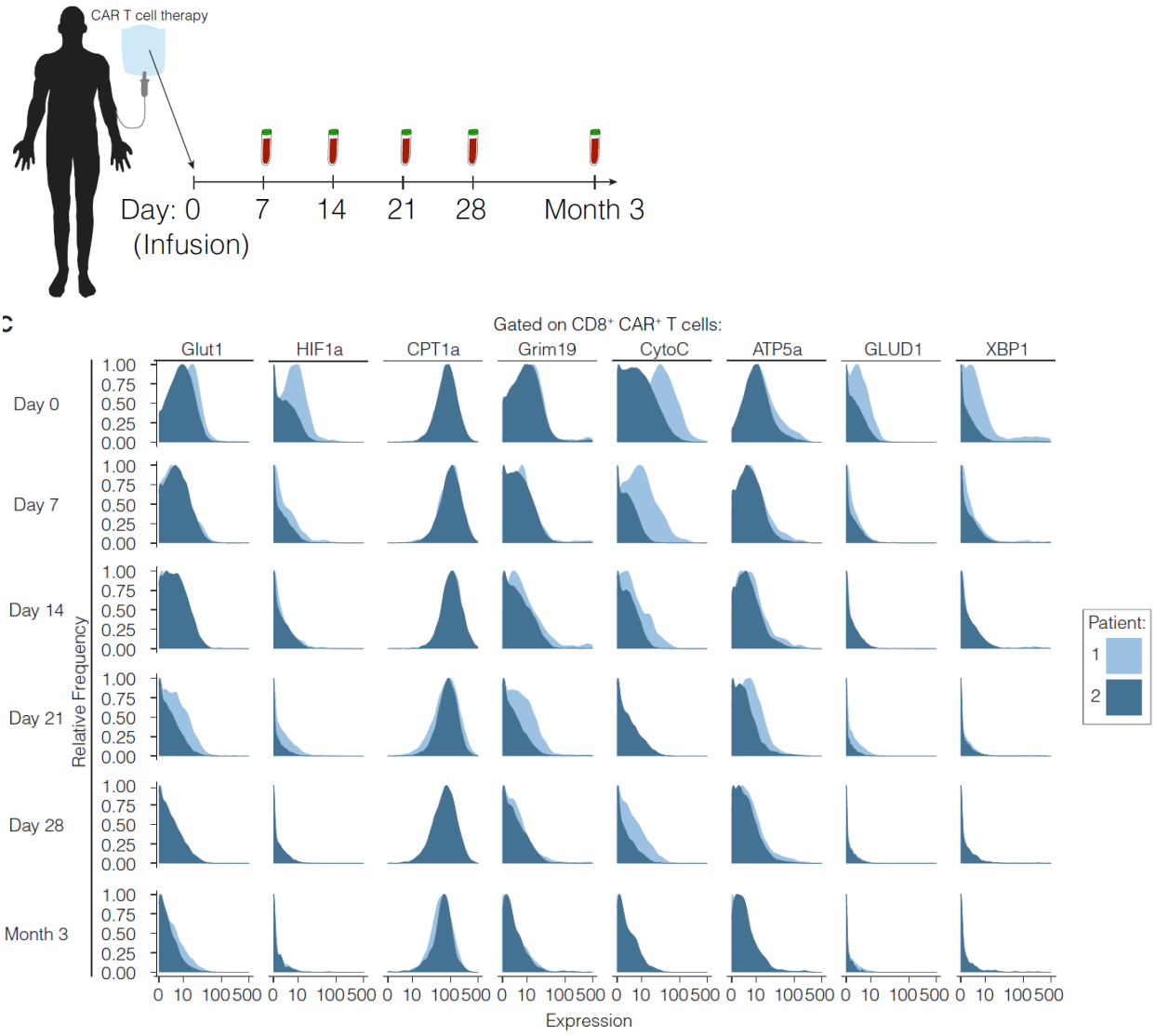

Figure 4.1: CAR T cells undergo metabolic differentiation after infusion into patients. Axicabtagene ciloleucel CAR T cells from two advanced non-Hodgkin lymphoma patients were sampled at the time of infusion, and PBMCs were isolated from the same patients on days 7, 14, 21, and 28 and month 3 post-infusion for analysis by mass cytometry. Shown are CyTOF expression levels of key metabolic markers in CAR T cells at each time point post-infusion by patient.

DON-treated CD8 T cells have reduced persistence but maintain memory function

CAR T cells are a form of adoptive cell therapy, whereby T cells are cultured *in vitro* prior to transfer *in vivo* to exert anti-tumor function. We hypothesized that glutamine inhibition strategies during initial T cell activation would differentially affect the persistence and function of T cells

after adoptive transfer, including their ability to mount a memory response. Intriguingly, knockout of GLS specifically in T cells in CD4-Cre $GLS^{fl/fl}$ mice had no discernable effect on effector and memory CD8 T cell levels during an endogenous response to *Listeria monocytogenes* expressing ovalbumin (Lm-OVA) (**Figure 4.2a-b**). Transient inhibition of glutamine during CD8 T cell activation might lead to a distinct result. Therefore, we designed a model of CD8 T cell activation to test the effects of transient specific GLS inhibitor (GLSi) CB839, pan-glutamine inhibitor DON, and culturing CD8 T cells in media without glutamine (No Q). This establishes a putative gradient of glutamine availability, from control conditions with glutamine, to only GLSi, to pan-glutamine blockade, to little or no glutamine available in media. Splenocyte OVA-specific CD8 T cells from Thy1.1+ mice were activated in the presence of SIINFEKL peptide and IL-2 for 24hr prior to magnet assisted cell sorting (MACS) with a CD8 negative selection kit to remove splenocyte APCs and peptide. CD8 T cells were then cultured for another 24hr in IL-2 prior to adoptive transfer (**Figure 4.2c**).

Inhibition of glutamine metabolism after 48hr reduced CD8 T cell numbers and proliferation without affecting viability (**Figure 4.2e-f**). To measure T cell activation, we measured cell size, granularity, CD69, CD44, CD62L, and CD44 by flow cytometry at 4hr, 24hr, and 48hr. There was approximately equal upregulation of activation marker CD69 at 4hr prior to cell blasting (**Figure 4.2g-h**). DON and No Q conditions delayed T cell blasting. Activation markers CD69, CD44, and CD25 increased as expected during activation, except that in No Q conditions CD44 was delayed and CD69 was elevated. CD62L levels increased relatively more by 48hr in CB839 and DON conditions, canonically associated with a more stem-like differentiation.

To assess the persistence of previously activated “memory-like” cells, OT-I cells were adoptively transferred into Thy1.2+ naïve mice and analyzed 35 days later. DON treatment significantly reduced the number of memory Thy1.1+ OT-I cells in the spleen, with similar trends in adipose tissue and liver (**Figure 4.2i**). To determine if the functionality of the persisting CD8 cells differed, we MACS purified splenic Thy1.1+ cells from this 35-day time point and adoptively transferred these cells in equal numbers to new Thy1.2+ hosts. The next day, the recipient mice were infected with Lm-OVA and secondary effector cells were measured 7 days later. CB839- and DON-treated expanded similarly to control OT-I, but there were fewer No Q responding OT-I cells (**Figure 4.2j**). These results suggest that glutamine blockade with DON reduces the persistence of adoptively transferred cells *in vivo* but those that persist maintain the ability to function as memory cells. Conversely, CD8 T cells cultured without glutamine *in vitro* persist *in vivo* but have a defect in secondary responses weeks later. These results would be consistent with other work showing that cell fate can be determined from as early as the first cell division (Chang et al 2007).

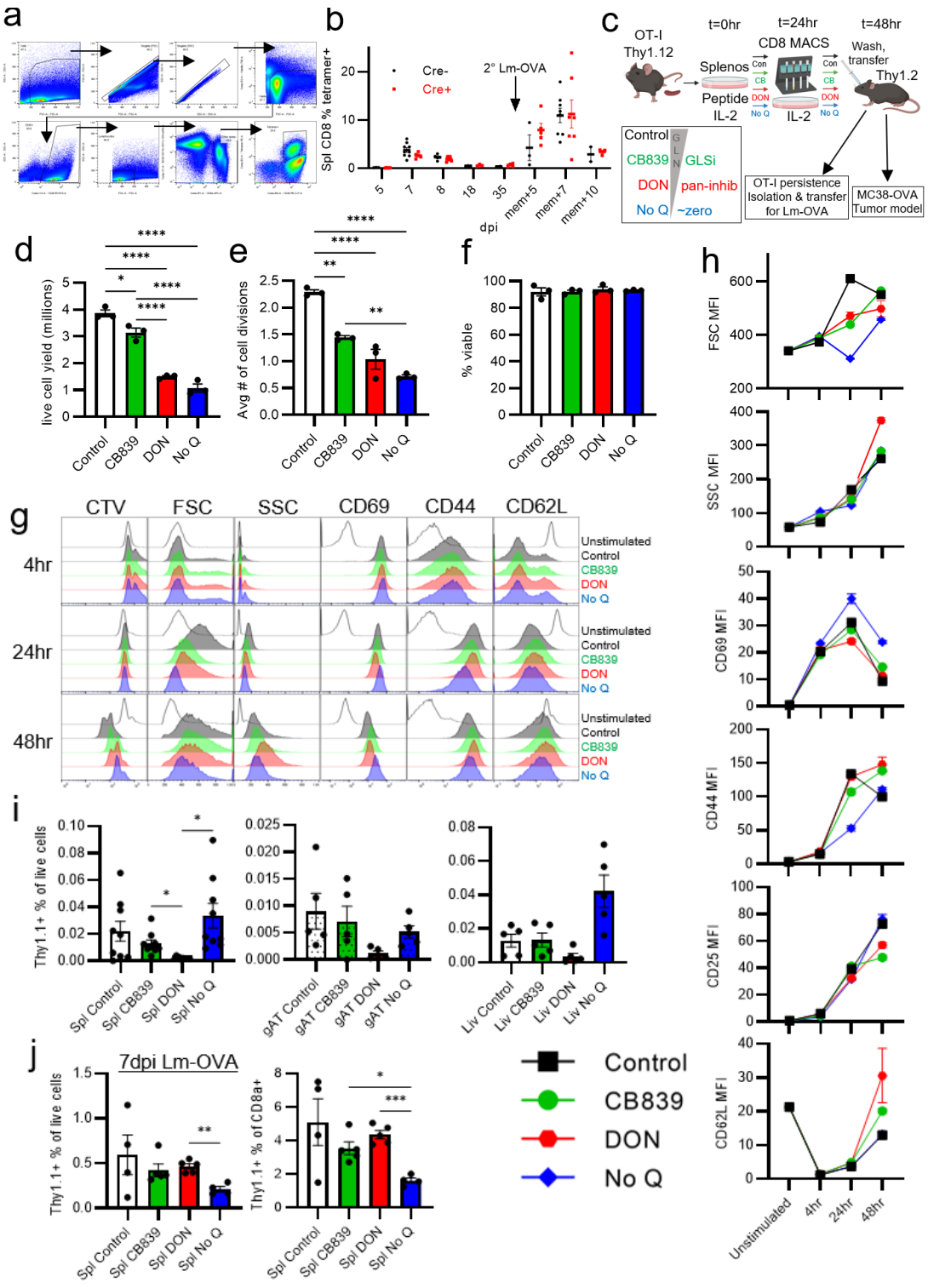

Figure 4.2: Pan-glutamine inhibition reduces *in vivo* persistence of CD8 T cells without affecting recall capacity. **a-b**, Gating scheme (**a**) and quantification (**b**) of splenic antigen-specific tetramer+ CD8 T cells in CD4-Cre Gls fl/fl mice at indicated days post infection (dpi) with Lm-OVA or after secondary infection >35 days post initial infection. **c**, Scheme of in vitro activation of OT-I CD8 T cells in different glutamine conditions prior to adoptive transfer. **d-f**,

Live cell yield (**d**), average number of cell divisions based on dilution of proliferation dye (**e**), and viability (**f**) 48hr post activation of OT-I cells. **g-h**, Flow cytometry analysis of cell morphology and activation markers at indicated timepoints post activation from n=3 mice. **i**, Abundance of Thy1.1+ OT-I cells in spleen (Spl), gonadal adipose tissue (gAT), and liver (Liv) 35 days post adoptive transfer after being activated in indicated glutamine conditions for 48hr. **j**, Abundance of effector Thy1.1+ OT-I cells 7 days after sorting and adoptive transfer of equal numbers into naïve mice then infected with Lm-OVA. Dots indicate biological replicates. Mean and SEM are shown of representative experiments performed at least twice, or from merged experiments in **b** and **i**. Asterisks indicate p-values of Brown-Forsythe and Welch ANOVA tests with multiple comparisons (* $p<0.05$, ** $p<0.01$, *** $p<0.001$, **** $p<0.0001$).

Glutamine alters differentiation markers and effector molecules

We hypothesized that differences in expression of key transcription factors, coinhibitory receptors, or effector molecules over the time course of *in vitro* activation may predict differences in cell fate after adoptive transfer. Key differentiation and effector molecules were measured by flow cytometry at 4, 24, and 48hr post activation. TCF1, a transcription factor associated with stem-like phenotypes in CD8 T cells (Siddiqui et al 2019), was higher in CB839 and DON treated OT-I at the time of adoptive transfer (**Figure 4.3a**). Effector-associated TBET and memory-associated EOMES (Banerjee et al 2010) increased during activation but were highest in No Q CD8 cells at 48hr (**Figure 4.3b-c**). PD-1, a coinhibitory receptor associated with CD8 dysfunction in cancer and chronic viral infection but better contextualized here as an activation marker, was expressed at lower levels in all glutamine-inhibited cells at 24hr but was similar to control by 48hr (**Figure 4.3d**). Cytolytic molecules perforin and granzyme B were similarly blunted initially (**Figure 4.3e-f**). Cytokine production demonstrated differences, most notably decreased IFNγ production across glutamine conditions (**Figure 4.3g-i**). Overall, there were no obvious changes consistent with reduced persistence of DON-treated or with reduced memory function in No Q-treated CD8 cells *in vivo*.

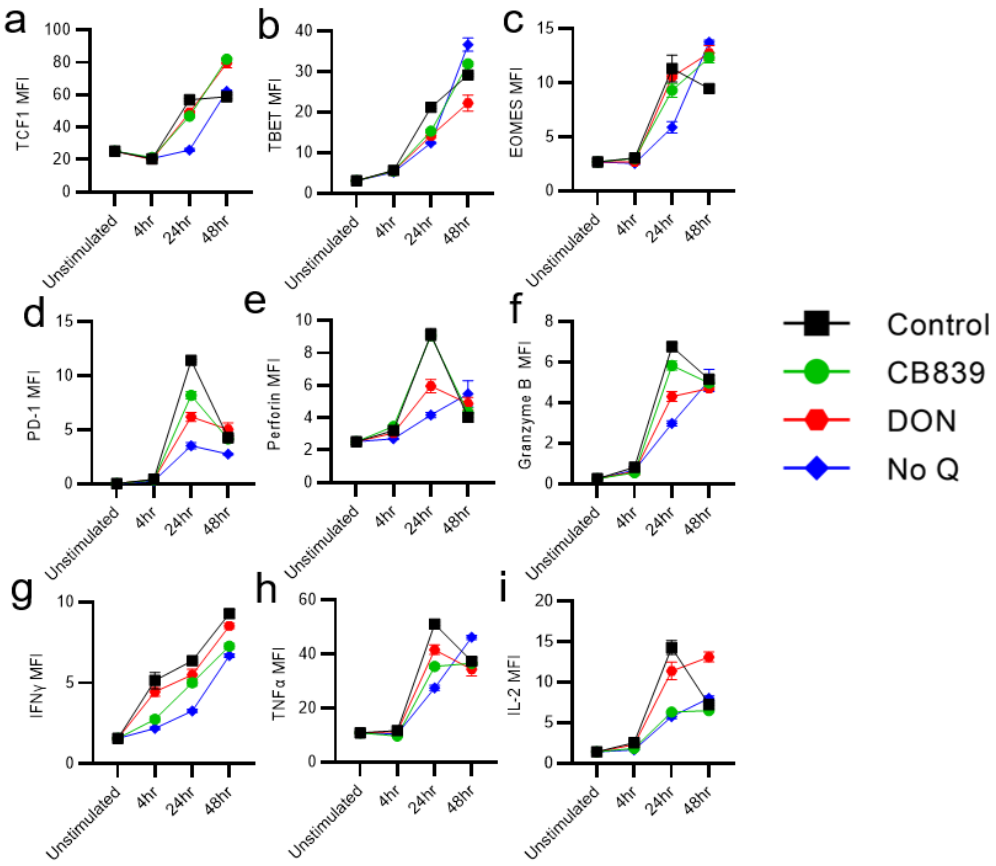

Figure 4.3: Effect of glutamine inhibition on differentiation and effector molecules during the initial 48hr of CD8 T cell activation. Median fluorescence intensities (MFI) of the markers at designated timepoints and with respective glutamine treatments. Intracellular cytokine staining for IFNγ, TNFα, and IL-2 was performed after 4hr PMA/ionomycin stimulation (**g-i**). Data are from n=3 mice and graphs show mean and SEM. Representative of at least 2 independent experiments.

The global transcriptome is most altered by DON treatment

Differentiation markers were not obviously associated with *in vivo* phenotypes, but we hypothesized that alterations to the global transcriptome and metabolome over time would underly differences in glutamine-inhibited T cell fate. We performed RNA sequencing (RNAseq) on *in vitro* activated OT-I cells at 0, 4, 24, and 48hr cultured in control, CB839, DON, and No Q conditions. Principal component analysis (PCA) revealed clustering according to time of activation, with the ability to distinguish DON and No Q-treated samples from other treatment groups at 24 and 48hr (**Figure 4.4a**). Pearson correlation coefficient analysis also demonstrated

grouping according to day of activation, with clear demarcation of DON and No Q samples at 24 and 48hr (**Figure 4.4b**). DON treatment by 48hr appeared to cause greater differences compared to the other treatments. The overall number of differentially expressed genes (DEGs) over time for each treatment was appoximately the same, although more genes changed for DON and No Q in the 24-48hr interval, with a notable number of downregulated genes with DON treatment (**Figure 4.4c**). We hypothesized that genes regulated by glutamine might share similar changes in gene expression across treatment groups, or alternatively that glutamine-sensitive genes that have inverse changes in expression might determine differences between treatments. The number of DEG for CB839 was much lower than for DON and No Q, consistent with its tight clustering with control cells by PCA and Pearson correlation coefficient analysis (**Figure 4.4d**). Substantial numbers of DEGs were shared between DON and No Q groups, including many that, although they are significantly different than control cells, are inversely differentially expressed in the DON and No Q groups. These genes, indicated by ≠ in Figure 4.4d, may provide insights to how DON and no Q groups, similarly the "most restrictive" treatments on glutamine metabolism, can have contrasting effects on CD8 T cell function *in vivo*. Future analyses will focus on interrogating these gene sets.

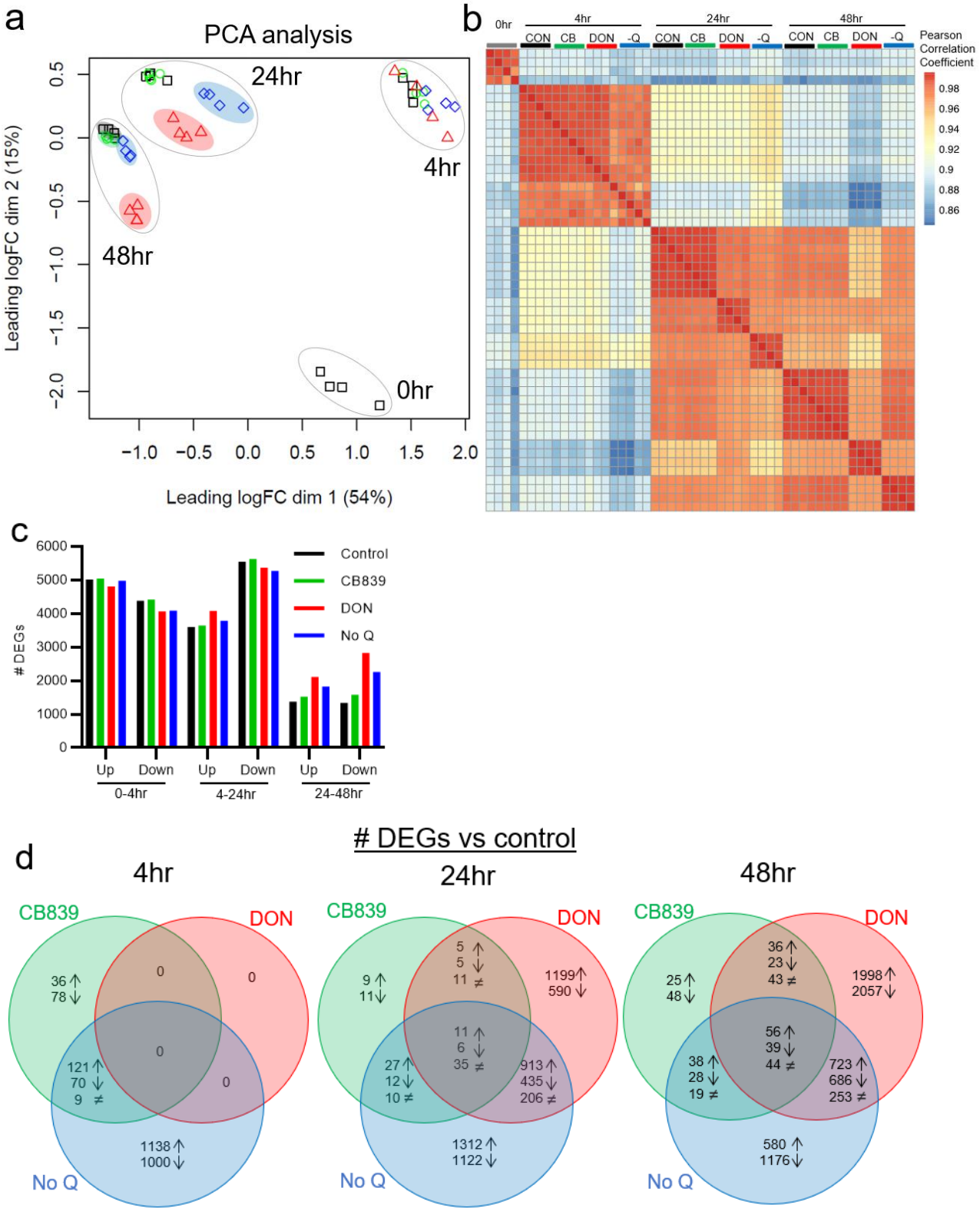

Figure 4.4: Global transcriptome analysis of glutamine-inhibited CD8 T cells. a-b, PCA (**a**) and Pearson correlation coefficient analysis (**b**) of RNAseq transcriptomes from glutamine-inhibited CD8 T cells. **c**, Number of differentially expressed genes (DEGs) within treatment groups during the indicated activation time intervals (FDR<0.05 for indicated comparison). **d**,

Number of DEGs compared to control (FDG<0.05) at the indicated timepoints. Venn diagram demonstrates the number of DEGs shared across treatment groups. Arrows indicate the direction of differential expression compared to control, and ≠ indicates share DEGs with opposite directions of differential expression. Analysis from n=4 biological replicates.

GLS and pan-glutamine blockade promote divergent metabolic programs

Glutamine inhibition has been shown to produce substantial changes in metabolic programs of T cells, included enhanced glycolysis and oxidative metabolism (Johnson et al 2018, Nabe et al 2018, Leone et al 2019). By 48hr after activation, RNAseq expression patterns suggested high levels of glycolysis and fatty acid synthesis-related transcripts in control and CB839 groups (**Figure 4.5a-b**). Fatty acid catabolism-related transcripts appeared to be elevated with DON-treatment, and DON-treatment also uniquely appeared to decrease levels of cytoplasmic aminoacyl-tRNA synthetases necessary for charging tRNA with amino acids for protein translation (**Figure 4.5c-e**). Transcripts for components of the electron transport chain important for oxidative phosphorylation did not appear obviously altered across treatment groups (**Figure 4.5f**).

To characterize the cellular metabolism of glutamine-inhibited CD8 T cells, we performed extracellular flux analysis across the established 0, 4, 24, and 48hr timepoints of differentiation. Basal extracellular acidification rate (ECAR), a proxy for lactate production from glycolysis, and oxygen consumption rate (OCR), a measurement of oxidative metabolism, demonstrated different trajectories of metabolic differentiation according to treatment (**Figure 4.6a-d**). By 4hr, all cells demonstrated increased ECAR consistent with activation-induced glycolysis. After 4hr, distinct metabolic differentiation trajectories become evident. Control and CB839 cells demonstrated relatively higher ECAR than OCR, whereas DON and No Q groups demonstrated relatively higher OCR than ECAR (**Figure 4.6e**). These results are consistent with control and

CB839 cells relying more on glycolysis. Interestingly, CB839 treatment decreased the OCR/ECAR ratio compared to control, suggesting that GLSi confers an opposite effect than more general glutamine inhibition strategies. Although CB839 reduced basal OCR, it retained a greater maximal OCR with a reduced proton leak compared to control T cells, potentially consistent with greater mitochondrial reserve and healthier mitochondria (**Figure 4.6f-g**). Measurement of mitochondrial mass and membrane potential was largely consistent with maximal and basal OCR (**Figure 4.6h-i**). The membrane potential to mass ratio was lowest with CB839, consistent with low basal OCR and potentially reduced proton leak and mitochondrial health (**Figure 4.6j**). mTORC1 signaling is critical for anabolic metabolism in proliferating cells including activated CD8 T cells. Glutamine inhibition broadly blunted mTORC1 signaling early during activation, but it subsequently rebounded particularly with CB839 treatment (**Figure 4.6k**). This may support the relatively high ECAR and low OCR/ECAR ratio with CB839 treatment, consistent with high glycolysis and supported by elevated lactate secretion determined by NMR (**Figure 4.6l**). Overall, our results suggest that the metabolic differentiation trajectories of CB839-treated CD8 T cells varies drastically from DON and No Q-treated cells, with greater glycolysis after GLS-specific inhibition and greater oxidative phosphorylation (OXPHOS) in pan-glutamine inhibition.

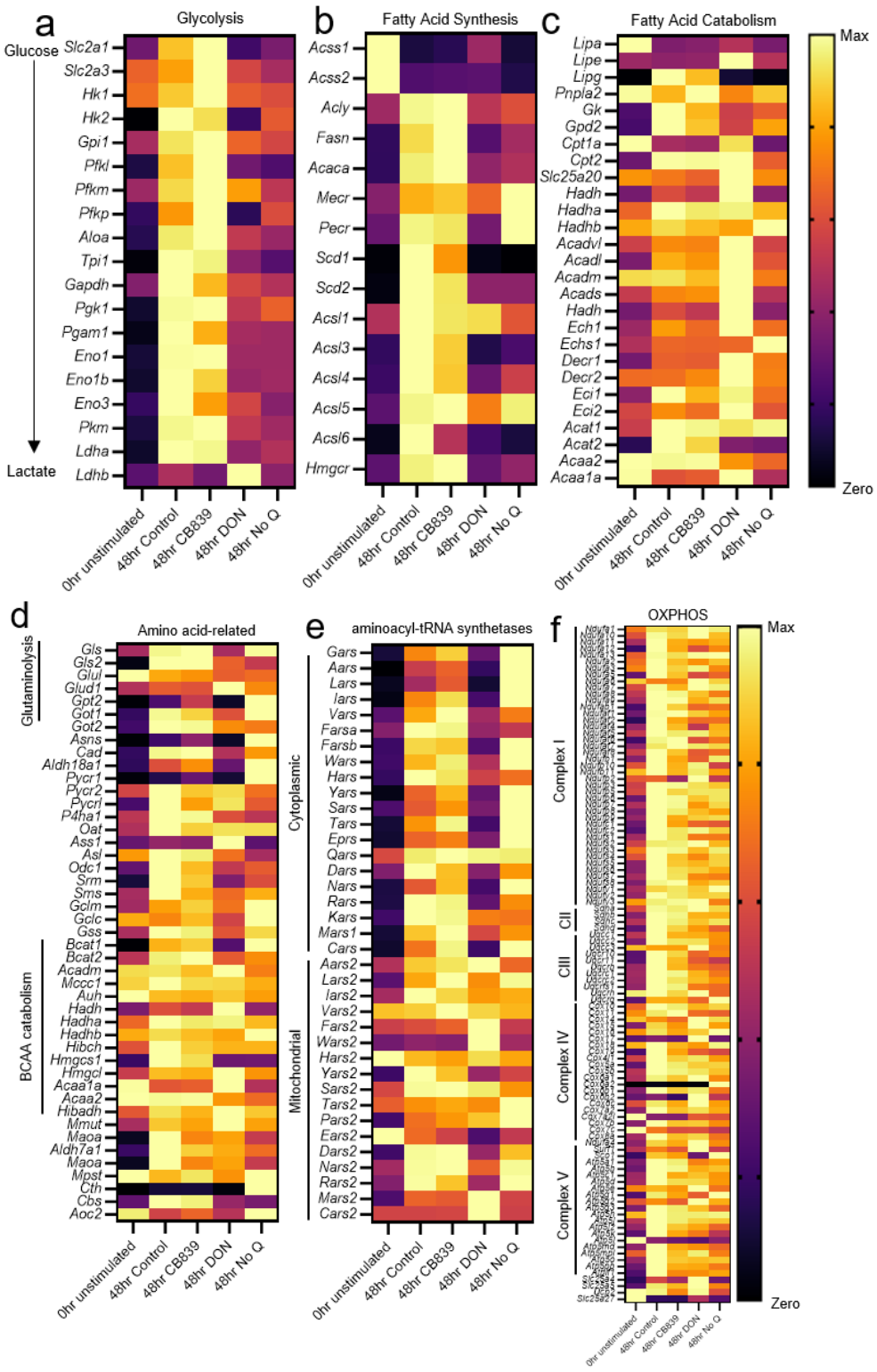

Figure 4.5: The metabolic transcriptome is altered by glutamine inhibition strategies. Heatmaps show curated gene sets of indicated pathways with expression normalized to the maximum average value for that gene across treatment groups. Unstimulated and 48hr expression levels are shown. Data are the average of n=4 biological replicates.

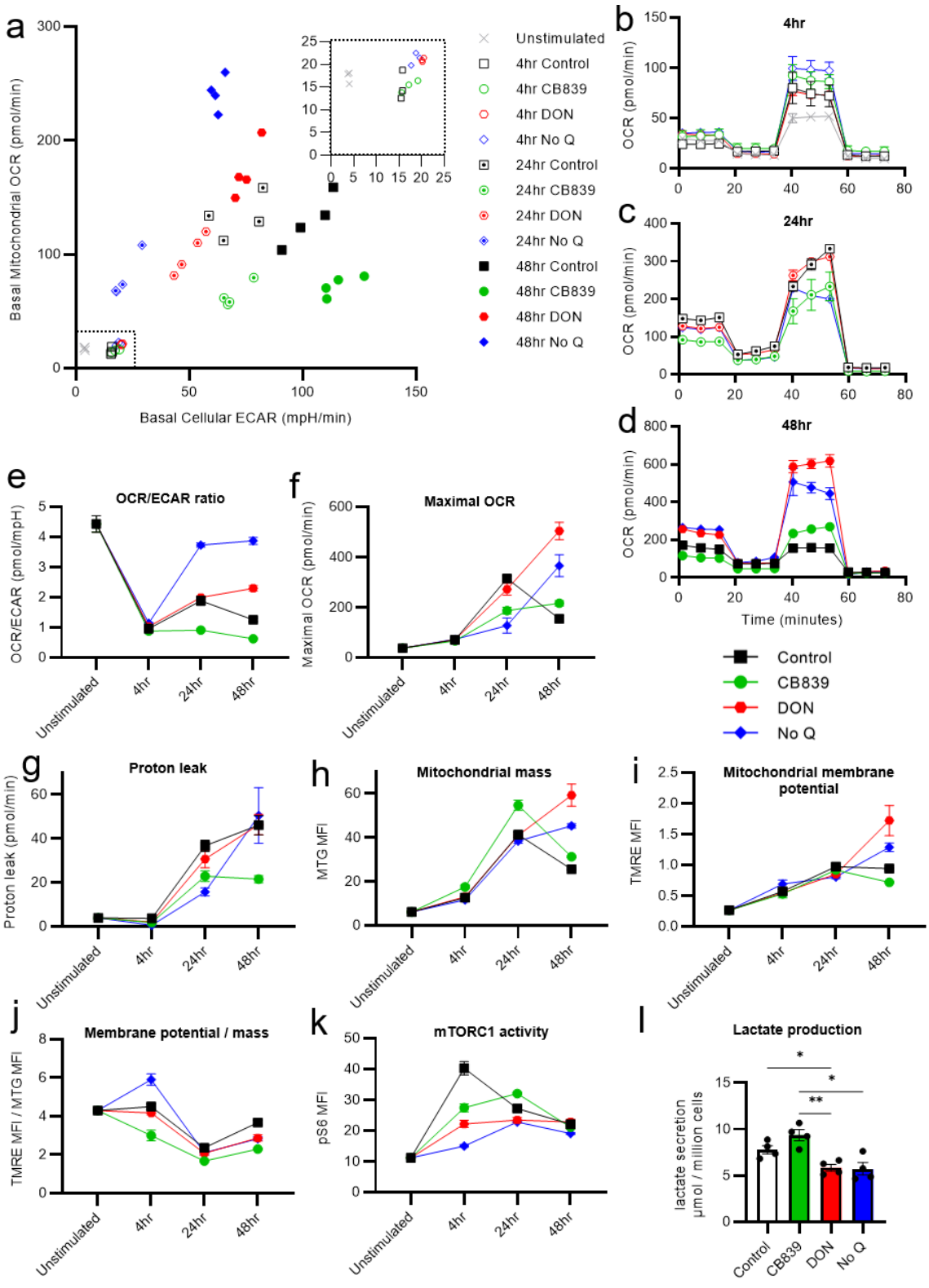

Figure 4.6: Functional metabolic analysis of glutamine-inhibited CD8 T cells. Extracellular flux analysis was performed on OT-I CD8 T cells at indicated timepoints of differentiation with

different glutamine inhibition strategies **a**, Basal mitochondrial OCR versus basal cellular ECAR. 0hr and 4hr timepoints are expanded in upper right corner. **b-d**, Representative OCR tracings of mitostress tests for a given biological replicate (n>3 technical replicates per biological replicate). **e-g**, Calculated OCR parameters from mitostress tests. **h-k**, Flow cytometry MFIs for determination of mitochondrial mass (mitotracker green, MTG) (**h**), mitochondrial membrane potential (Tetramethylrhodamine ethyl ester, TMRE) (**i**), potential normalized to mass (**j**), and phosphorylated S6 protein (pS6) (**k**). **l**, NMR-measured lactate secretion normalized to final cell number from cell culture media at 48hr. N=3-4 mice per experiment. Extracellular flux assays are representative of at least 2 independent experiments. Asterisks indicate p-values of Brown-Forsythe and Welch ANOVA tests with multiple comparisons (* $p<0.05$, ** $p<0.01$).

Global H3K27me^3 and acetylation are altered by glutamine treatment

Epigenetic modifications including histone methylation and acetylation enforce T cell differentiation state (Britt et al 2020). Metabolites are the substrates for acetylation and methylation, and α-ketoglutarate downstream of glutamine is a demethylase cofactor. We hypothesized that glutamine inhibition strategies may have differential effects on histone modifications. We performed CUT&RUN sequencing (CUT&RUNseq) to specifically identify genomic regions around acetylated H3K27 (H3K27Ac), associated with open chromatin and gene transcription, and trimethylated H3K27 (H3K27me^3), associated with closed chromatin. We found global changes according to glutamine treatment at 24hr and 48hr (**Figure 4.7**). Notably, No Q conditions appeared to reduce global H3K27Ac at 24hr but increase acetylation at 48hr, whereas H3K27Ac appears down with CB839 and DON at 48hr. Further analysis of these datasets will shed light on the potential regulation of glutamine on site-specific histone modifications and paired transcription.

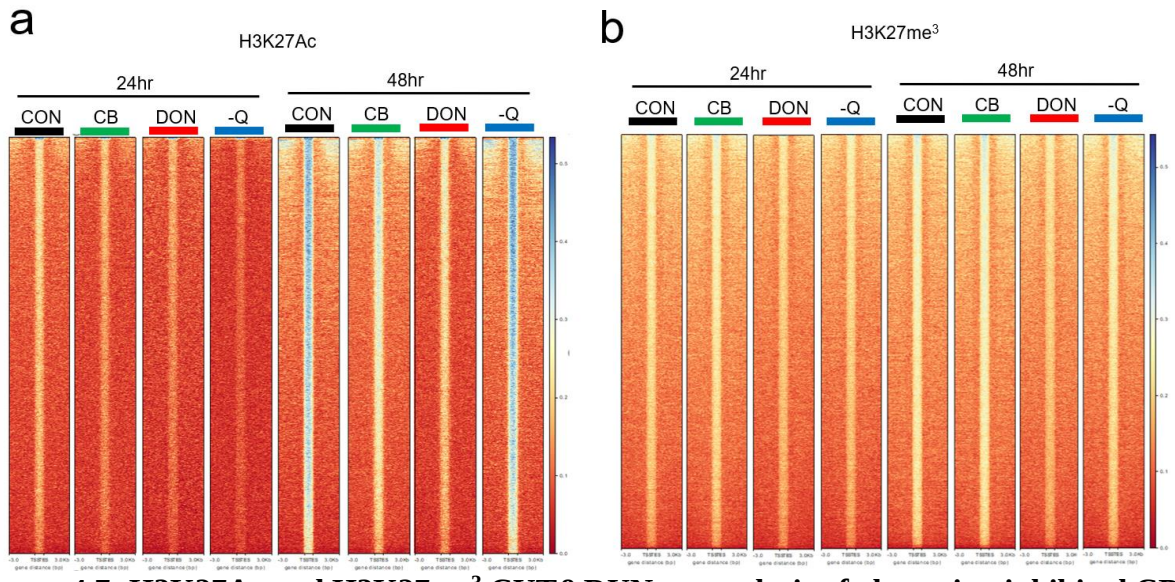

Figure 4.7: H3K27Ac and H3K27me^3 CUT&RUNseq analysis of glutamine-inhibited CD8 T cells. Read peak intensities for CUT&RUNseq of H3K27Ac (**a**) and H3K27me^3 (**b**) to IgG control centered along transcription start sites. Representative data of 2 biological replicates.

DON-treated CD8 T cells have impaired control of tumor growth

We asked if glutamine inhibition strategies could be implemented to support adoptive cell therapy treatment of tumors. MC38 tumors grown in CD4-Cre GLS$^{fl/fl}$ mice demonstrated no difference in final tumor size, tumor T cell infiltration, or T cell IFNγ production (**Figure 4.8a-d**), although there was a striking increase in mTORC1 activity in tumor CD8 T cells (**Figure 4.8e**). To determine if transient glutamine inhibition strategies affect adoptive cell therapy efficacy, we injected MC38-OVA tumor-bearing mice with OT-I CD8 T cells activated for 48hr in control, CB839, DON, or No Q conditions. The dose of OT-I cells was insufficient to eliminate tumors but did slow tumor growth. DON-treated OT-I cells failed to control tumor growth as well as other treatments (**Figure 4.8f**). This was associated with fewer DON-treated OT-I cells infiltrating tumors and in spleens (**Figure 4.8f-h**), consistent with reduced persistence observed in **Figure 4.2**.

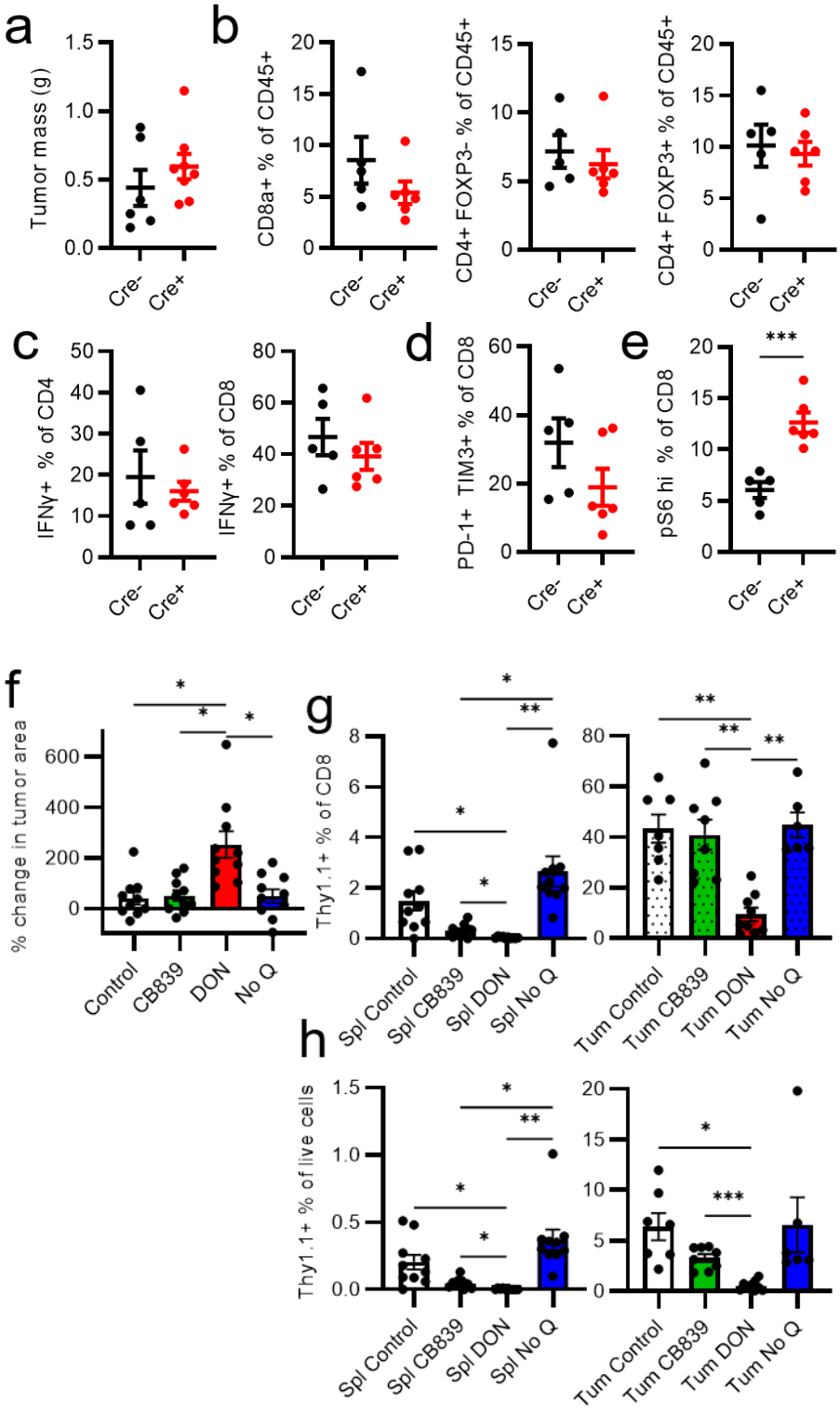

Figure 4.8: Tumor control is impaired by DON treatment of OT-I CD8 T cells. a, Final tumor mass of MC38 tumor grown in CD4-Cre GLS fl/fl mice. **b**, Abundance of indicated T cell subsets in MC38 tumors. **c-d**, IFNγ production in CD8 and CD4 T cells from MC38 tumors. **d-e**, PD-1 and TIM3 coexpression and pS6 levels in CD8 T cells in MC38 tumors. **f**, Change in MC38-OVA tumor

area from day of OT-I T cell injection to endpoint of experiment. **g-h**, Thy1.1+ OT-I T cell abundance in spleens and MC38-OVA tumors. Each dot represents a biological replicate. f-h show results merged from 2 independent experiments. Asterisks indicate p-values of Brown-Forsythe and Welch ANOVA tests with multiple comparisons (* $p<0.05$, ** $p<0.01$, *** $p<0.001$).

Discussion and future directions

We found that the mechanism of glutamine inhibition has broad implications for adoptive cell therapy efficacy. DON treatment impaired tumor-specific CD8 T cell function *in vivo* and was associated with vast differences on the transcriptomic, epigenomic, and metabolic level from control, CB839-treated, and no glutamine-treated T cells. Our findings stand in contrast to Nabe et al 2018 which found enhanced anti-tumor control after transient treatment with DON. The authors relied on EL4-OVA thymoma cancer cells compared to our MC38-OVA model. It is possible that longer *in vitro* expansion and washout of DON for one day prior to transfer selected for healthier cells, thereby improving tumor control compared to control. This result demonstrates the complexities of adoptive cell therapy manufacturing, where culture conditions can produce vast changes in effector cell function *in vivo*. Our results are also distinct from Leone et al 2019, which found that *in vivo* treatment with a DON analog promoted CD8 TIL anabolic metabolism and activity. This contrast could represent differences in utilization of glutamine during distinct stages of T cell function. During initial activation pan-glutamine blockade may be detrimental to CD8 survival, whereas in the tumor microenvironment pan-glutamine blockade may potentiate effector functions based on the local environment and the differentiation state of the T cell. It is also possible that CD8 invigoration by DON *in vivo* is secondary to effects of DON on cancer cells or other cells in the TME. Ongoing clinical trials will ultimately demonstrate efficaciousness of many different glutamine-inhibition strategies in cancer patients (ongoing trials can be found in Lemberg et al 2022).

Our results demonstrate that, in the first 48hr of activation and the first rounds of cell division, glutamine determines the metabolic and differentiation trajectories of CD8 T cells. These results are not consistent with glutamine inhibition "slowing down" differentiation wholesale, although proliferation was reduced particularly with DON and no glutamine treatments.

There are multiple important future directions for this work to determine that full role of glutamine inhibition strategies on CD8 T cell differentiation. A paired analysis of transcriptomic and CUT&RUNseq may reveal specific mediators of glutamine-differentiation on an epigenetic level. Additional gene set enrichment analyses of the RNAseq datasets may also suggest common and divergent effects of GLS versus pan-glutamine inhibition. Particular attention should be paid to the kinetics of changes over time, such as with the Tcseq (time course sequencing data analysis) pipeline (Mengjun 2021).

While we characterized T cell differentiation during the first 48hr of activation, we did not check the transcriptional, epigenetic, and metabolic phenotypes of cell after adoptive transfer *in vivo*. Analysis of sorted cells immediately *ex vivo* will provide powerful evidence that glutamine during early T cell activation has durable effects on differentiation. Similarly, examination of changes between 4hr and 24hr may also be worthwhile, particularly as to how metabolite levels directly tied to epigenetics are changing. These include, in order of importance with respect to glutamine flux: α-ketoglutarate, acetyl-CoA, and S-adenosyl methionine (SAM).

Interest in targeting glutamine metabolism for cancer and autoimmunity continues, and this work highlights the importance of specifying specific targets to optimally affect target cells and avoid

toxicities. Pooled *in vivo* CRISPR screening targeting glutamine-related genes would provide a powerful approach to identify new candidates beyond GLS (Sugiura et al 2022).

CHAPTER 5: OVERALL DISCUSSION AND FUTURE DIRECTIONS

Cell type-specific metabolism in the tumor microenvironment

This dissertation examines how cells in cancer utilize fuels differently and how it effects their function. In Chapter 2, we asked which broad cell types uptake major nutrients in the TME. Using ^{18}F-nutrient tracers, we determined that glucose and glutamine partition into myeloid and cancer cells respectfully. We also found that, rather than competing for scarce nutrient resources in the TME, tumor cells use different nutrients according to their cell programs. These results were surprising, as we expected cancer cells to dominate nutrient uptake. In Chapter 3, we tested multiple specific hypotheses about nutrient uptake in the TME and show that myeloid cells seem to use glucose in other inflammatory contexts, as well. Finally, in Chapter 4, we asked how one cell type, CD8 T cells, are affected by inhibition of glutamine metabolism. We found that GLS-specific inhibition differs sharply from blocking overall glutamine metabolism during early CD8 T cell activation, with distinct differentiation trajectories and subsequent anti-tumor activity.

A theme of our work is the importance of understanding tumor metabolism and immunometabolism in a cell, tissue, and context specific manner. The paradigm of cancer cell aerobic glycolysis was critical in starting the field of tumor metabolism and changed the way scientists thought about the metabolism of proliferating cells. Often, an assumed corollary of the Warburg Effect could be that cancer cells dominate glucose metabolism in the TME. This view conformed with the basic observation and pathophysiology of tumors: cancer cells require energy and biomass to support uncontrolled growth eventually invading healthy tissue, metastasizing, and eventually causing critical organ failure. Cancer cell-centric glucose

consumption was also confirmed on a regular basic clinically through the advent of FDG-PET imaging to monitor patient tumor status.

In the field of immunometabolism, studies revealed that activated immune cells can adopt a metabolic program like cancer cells. Aerobic glycolysis underlies normal immune cell proliferation and effector function. Notably, FDG-PET not only delineates tumors, but also unveils areas of non-malignant inflammation. The assumption that glucose consumption in glycolytic FDG-avid tumors is dominated by cancer cells was strengthened by the hypothesis of nutrient competition in the TME. By consuming all the scarce glucose, cancer cells directly contribute to the immunosuppressive microenvironment and dysfunctional glucose metabolism of tumor CD8 T cells.

In this historical narrative, we asked a basic question: Which cells truly pick up glucose in the TME? We were surprised to uncover results seemingly inverted of the assumed Warburg Effect paradigm. Immune cells, not cancer cells, have the highest glucose uptake in the TME. Glucose uptake is highest in myeloid cells like macrophages and can be changed by pharmacologic targeting or cellular metabolic programming. In contrast to glucose, glutamine is preferentially consumed by cancer cells. Thus, we proposed a model whereby nutrients partition into different cells in the TME according to their cellular programs, not according to competition for scarce metabolites.

“Cell-programmed nutrient partitioning” is a model meant to supplement and complement existing idea of tumor metabolism. Given the heterogeneity of cancer, there may be some tumors

were scarce nutrients are consumed according to competitive uptake and could lead to immune cell dysfunction. However, our data and that of others suggest that nutrient concentrations are not always scarce. Additionally, steady-state concentration will not necessarily reflect the flux of uptake, metabolism, and export. Our model supports focus on the buildup of immunosuppressive metabolites in the TME as mediators of metabolic dysfunction, such as lactate, reactive oxygen species, protons, and kynurenine. Our approach is not without its limitations as outlined in the discussions of Chapter 2 & 3. Of special note, our dependence on live cell FDG uptake may mean that our results reflect nutrient uptake in healthy tissues and non-necrotic tumor areas, and/or that we are selecting for the tumor cells most amenable to processing to single cells.

Future directions in the metabolic tumor microenvironment

In the future, interrogating how specific cells utilize nutrients differently *in vivo* may best inform the next therapeutic strategies. Continuing to measure nutrient uptake is important, but the intracellular fate of nutrients will provide insight into how metabolism shapes cell fate and function. *In vivo* stable isotope tracing with ^{13}C and ^{15}N labelled glucose and glutamine coupled with specific cell isolation would provide major insights. Emerging approaches also permit subcellular localization of labelled nutrients to ascertain organelle-level partitioning of nutrients (Arrojo e Drigo et al 2019).

Metabolic approaches need to be combined with biologically meaningful functional readouts. We have left many questions about what aspects of cellular programming determine metabolism and subsequently how they both contribute to function. Future and ongoing work in the lab interrogates the role of HK3, a myeloid-specific hexokinase, in driving myeloid cell-specific

glucose uptake. Another project interrogates how genetic differences among cancer cells, the fundamental etiology of cancer, shape the TME. In clear cell renal cell carcinoma, loss of VHL is ubiquitous and is hypothesized to drive glycolysis in cancer cells via HIF activity. Other tumors have characteristic activation of other master regulators, which may contribute to the metabolic TME. Other potentially important factors affecting the metabolic TME is cancer cell cell-of-origin and the site of the tumor, including during metastasis. In all of these cases, we may hypothesize a common feature of high myeloid cell glucose uptake, since this appears to be a conserved feature of inflammation. If myeloid cells have low glucose uptake, it would be interesting to uncover what properties of the cancer cells are deterministic. Another more direct metabolite relationship may exist between myeloid cell glucose uptake and cancer cell glutamine uptake. In muscle, macrophages utilize glucose to synthesize glutamine which is then exported and utilized by myocytes (Shang et al 2020).

Another fascinating basic underlying mechanism in the metabolic TME is epigenetic alterations driven by metabolic flux. Just as differential glutamine metabolism changed CD8 T cell epigenetics in Chapter 4, there may be unique epigenetic signatures in tumor cells depending on their metabolic flux and differentiation. Hypothetically, the epigenetic changes would become durable and may shed light on treatment vulnerabilities.

We studied primarily glucose and glutamine uptake in major cell populations of the tumor microenvironment but extending our approach to other metabolites and inflammatory environments should be a major goal. Based on our results, lactate and fatty acid tracing should be highly prioritized. In Chapter 3, we show preliminary results that myeloid cells are major

glucose consumers in other inflammatory conditions. This may be important for autoimmune and autoinflammatory conditions. The use of magnetic microbeads is a powerful approach to isolating major cell populations, but a major advance technically would be the use of flow sorting on ^{18}F-avid cells to determine in vivo uptake on more specific and potentially more biologically relevant cell populations.

Ultimately, how can our results here translate to patient care? FDG PET imaging is used routinely to monitor patient responses in oncology purely as a specific tracer for tumors. Our results suggest that FDG might be marker of myeloid cell activity and that ^{18}F-glutamine may be a more specific marker of cancer cell metabolism. The interaction of glucose and glutamine PET could shed light on monitoring patient outcomes or predicting responses to particular therapies. ^{18}F-deoxycytidine as described in Nair-Gill et al 2010 may also be useful as T cell-specific tracer.

For the design of future therapies targeting the TME, is critical to consider the effect of these molecules on all cell types involved in cancer cell growth and anti-tumor immunity, including T cells and myeloid cells. Synergistic relationships as described by Leone et al 2019, whereby cancer cells falter while anti-tumor immunity is strengthened, should be an idealistic goal of therapy design. In Chapter 4, we interrogate how different approaches to glutamine inhibition have can alter CD8 T cell differentiation and impact anti-tumor immunity. This work can be extended through the identification of specific and hopefully targetable glutamine-related genes or metabolites that determine cell fate. CRISPR screening of glutamine-related genes may be one approach. Experiments adding back metabolites to cell cultures may also prove valuable.

Another major future direction for CD8 T cell metabolism is determination of time and differentiation-specific relationships between metabolites and epigenetic modifications. A major hypothesis in the field of immunometabolism is that metabolic processes directly determine epigenetic modifications through the availability of substrate and epigenetic regulators. These include acetyl-CoA for histone acetylation, SAM for histone and DNA methylation, and α-ketoglutarate as a cofactor for demethylases. CD8 T cell activation affords an opportunity to measure time-specific associations of metabolite levels with epigenetic marks, and subsequent manipulation of metabolic pathways to block the hypothesized flux of a substrate through a metabolic pathway to deposition as an epigenetic modulator.

CHAPTER 6: MATERIALS AND METHODS

Patient Samples

Fresh histology-confirmed clear cell renal cell carcinoma (ccRCC) tumors and matched normal tissue were surgically removed from 14 patients. Supplementary Information Table 1 contains relevant patient and tumor information. Tumor and matched normal kidney were processed by mechanical dissociation (human tumor setting two on Miltenyi gentleMACS™) in HBSS with calcium chloride and magnesium chloride. Mechanical dissociation was followed by enzymatic digestion in 435U/mL deoxyribonuclease I (Sigma-Aldrich, D5025) and 218U/mL collagenase (Sigma-Aldrich, C2674) in RPMI supplemented with 10% FBS, 1% glutamine, 1% pen/strep, 1% Hepes, and 0.1% 2-Mercaptoethanol for 30-45min, depending on tissue toughness, at room temperature with 17 rpm agitation. Tissue digests were washed with HBSS without calcium chloride, magnesium chloride, or magnesium sulfate and then incubated in 5mM EDTA for 20min at room temperature with 17rpm agitation. Tumor and matched normal kidney digests were washed with HBSS with calcium chloride and magnesium chloride. Then they were passed through a 70μm filter and ACK-lysed. Patient peripheral blood mononuclear cells (PBMC) were isolated by density gradient centrifugation using Ficoll-Paque (GE Healthcare, 17144002) in SepMate-50 tubes (Stemcell Technologies, 85450) and subsequently ACK-lysed. Single cell suspensions were frozen in 90% FBS 10% DMSO. Batched tumor and matched PBMC were thawed, rested for 10min at 37°C, counted, stained, and analyzed for flow cytometry. All studies were conducted in accordance with the Declaration of Helsinki principles under a protocol approved by the Vanderbilt University Medical Center (VUMC) Institutional Review Board (protocol #151549). Informed consent was received from all patients prior to inclusion in the study by the Cooperative Human Tissue Network at VUMC.

Interstitial fluid collection & LC/MS metabolite analysis

Tissue interstitial fluid (TIF) was collected from freshly resected ccRCC tumor and matched normal kidney tissue. Specimens were centrifuged against a 0.22μm nylon filter (Corning CLS8169) at 4°C for 5 minutes at 300g. Flow-through TIF was flash-frozen and stored at -80°C prior to batch analysis. Mouse blood was collected via submandibular vein, aliquoted immediately into EDTA, and centrifuged for 10min at 850g at 4°C. Plasma supernatant was collected and then cleared by centrifugation for 20min at 3000g at 4°C. Liquid chromatography/mass spectrometry (LC/MS) quantitation of metabolites was performed as described previously (Sullivan et al 2019).

Mice

C57BL/6J (000664), BALB/cJ (000651), Rag1 KO (002216) Thy1.1, (000406) and OTI transgenic (003831) mice were obtained from the Jackson Laboratory. Glut1 transgenic mice have been previously described and were originally created using full-length rat Glut1 cloned into the pLck.E2 vector (Zhao et al 2007). CD4-Cre $GLS^{fl/fl}$ mice were generated as described in Johnson et al 2017. Functionally wild-type CD4-Cre- $GLS^{fl/fl}$ mice were compared to functionally knock out CD4-Cre+ $GLS^{fl/fl}$ littermates. All mouse procedures were performed under Institutional Animal Care and Use Committee (IACUC)-approved protocols from Vanderbilt University Medical Center and conformed to all relevant regulatory standards. Mice were housed in ventilated cages with at most 5 animals per cage and provided ad libitum food and water. Mice were on 12 hour light/dark cycles which coincided with daylight in Nashville, TN. The mouse housing facility was maintained at 68-76°F and 30-70% humidity. For injectable tumor models, 8-20 week old male and female mice were used. Mice were euthanized if humane endpoint was reached (2cm dimension, ulceration, weight loss >10%). V9302 treatments were

administered intraperitoneally twice daily for five days at 25mg/kg for FDG uptake or once at 75mg/kg 3hr prior to ^{18}F-Gln injection. Rapamycin treatments were administered intraperitoneally daily for four days at 2mg/kg dissolved in 2% DMSO 30% Polyethylene Glycol 300 (Sigma Aldrich 202371), and 5% Tween 80 (sigma Aldrich P1754). 200 μg control IgG (InVivoMab Bio X Cell BE0089) and anti-PD-1 (InVivoMab Bio X Cell BE0146) treatment was administered intraperitoneally every other day starting at day 9. 200 μg control IgG (InVivoMab Bio X Cell BE0087) and anti-CTLA4 (InVivoMab Bio X Cell BE0131) treatment was administered intraperitoneally every other day starting at day 9. Mice were randomized at first day of treatment to control or drug in an unblinded manner, with mice from the same cage receiving different treatments. Sample sizes were chosen based on prior experiments. 25 μg STING agonist ADU-S100 (John Wilson lab, Vanderbilt University) dissolved in 100 μL PBS or PBS alone was injected directly into MC38 tumors using 27G insulin syringes on days 10 and 13 prior to analysis on day 14. PI3Kd/g inhibitor IPI-145 (Cayman Chemical 16800) was resuspended in 0.5% carboxymethylcellulose and 0.05% Tween 80 in ultra-pure water and was administered by oral gavage daily for 15 mg/kg for 5 days prior to analysis on day 14. IKFM double transgenic mice were generated by the Fiona Yull lab and were used as previously described (Connelly et al 2011, Hoover & Hufnagel et al 2020). Overall, mice with the reverse tetracycline transactivator (rtTA) gene expression driven by monocyte/macrophage-specific colony stimulating factor receptor 1 promoter cfms-rtTA (FMR), were bred with mice harboring the NF-κB activating (tet-O)7-FLAG-cIKK2 transgene (IKK). Doxycycline ingested with drinking water promotes rtTA protein binding to the tet operon, driving transcription of FLAG-cIKK2 specifically in the monocyte/macrophages lineage. Drinking water with 1 g/L doxycycline (Sigma Aldrich, St. Louis, MO) and 5% sucrose was started on day 7 post tumor

injection, and analysis occurred on day 14. Littermates lacking one or both transgenes were used as controls. For Alternaria-induced lung inflammation, mice were anesthetized with isoflurane and challenged intranasally with 8μg Alternaria extract (Greer Laboratories) every 3 days for 4 total challenges before analyzing the day after the final challenge (Palmer et al 2019).

Cell lines

The MC38 and CT26 cell lines were provided by Barbara Fingleton and grown in DMEM supplemented with 10% FBS. The Renca cell line was obtained through ATCC and grown in RPMI 1640 supplemented with 10% FBS, 4mM glutamine, 25mM HEPES, essential amino acids, and sodium pyruvate. Cells were trypsinized, washed twice in PBS, and $1x10^6$ cells were injected subcutaneously in 100-200μL of PBS on mouse flanks. Subcutaneous tumors grew for 14 days prior to analysis. The MC38-EL-Thy1.1 cells were generated using a transposon based engineering approach with plasmids that were described previously (O'Neil et al 2018). MC38 cells were electroporated using the NEON transfection system (ThermoFisher) according to manufacturer's recommendations for adherent cell lines. 5 million MC38 cells were suspended in electroporation buffer containing 5μg of the plasmid pCMV-M7PB and 15μg of the plasmid pT-EL-thy1.1, which is a bicistronic transposon vector driving expression of an enhanced firefly luciferase as well as Thy1.1 antigen. Cells were magnetically sorted based on expression of Thy1.1 using magnetic beads (Miltenyi 130-121-273). MC38-OVA cells were generated and provided by Richard O'Neil. Cell lines were regularly tested for mycoplasma via PCR and all cells used in downstream assays were confirmed negative.

Orthotopic renal implantation

For intrarenal Renca injections, survival mouse surgery was performed according to a method previously described (Tracz et al 2014). Briefly, mice were anesthetized by isoflurane inhalation at 2-3% and placed on a warming recirculating water pad set at 37°C to maintain body temperature. Using sterile surgical techniques, a 1-cm incision was made in the skin running parallel to the spine, slightly below the ribcage on the right flank. Next, a 1-cm incision was made in the muscle layer in the same location. Using gentle pressure on the mouse abdomen, the right kidney was exteriorized. $5x10^4$ Renca cells resuspended in 100μL of PBS were injected using a 29-gauge needle inserted through the renal capsule into the cortical space. The injection site was swabbed using sterile gauze and the kidney was returned to the body cavity. The abdominal wall was closed using 6-0 monofilament absorbable sutures (AD Surgical; S-D618R13), and the skin was closed using wound clips. Analgesic was provided pre-surgery and 24 hours post-surgery in the form of ketoprofen injections at 5 mg/kg. Wound clips were removed 7 days following the surgery. Tumors were analyzed 28 days after cancer cell injection.

Spontaneous mouse tumor models

PyMT GEMM mice were bred by crossing male transgenic mice expressing the polyoma virus middle T antigen (PyMT) oncoprotein under the MMTV-LTR (Jackson Laboratory 022974) with wildtype females on a similar B6/FVB mixed background. The GEMM mice were from a colony in which all mice expressed two *Vhl* alleles in which exon 1 is flanked by *loxP* sites (Jackson Laboratory 012933) but did not express a Cre transgene and were thus effectively wildtype. Once weaned, female mice were palpated twice a week and tumors were measured in three dimensions with digital calipers. Mice were collected when any tumor had grown to a size of 1 cm in diameter in any dimension, around 5 months of age. Virgin female littermates were used in these studies.

The AOM/DSS inflammatory colorectal cancer model was used as previously described (Parang et al 2016; Becker et al 2005). In brief, bedding was mixed to normalize microbiome two weeks prior to experimental initiation. 8-12 week-old C57BL/6J mice were intraperitoneally injected with 12.5 mg/kg AOM and exposed to three 4-day cycles of 3% to 4% DSS (TdB Labs 9011-18-1). Each DSS cycle was followed by a 16-day recovery period. Prior to sacrifice, colonoscopy was performed to confirm tumor development. Mice were weighed every other day throughout the experiment. Mice were euthanized 6-8wk after completing the last cycle of DSS. Colons were dissected and tumor tissue was isolated from the mucosa.

PET-CT imaging

For individual studies, a group of MC38 tumor-bearing mice were food-restricted overnight. Then the mice received a retro-orbital injection of ~ 37 MBq/0.1 mL of ^{18}F-FDG and were returned to plate-warmed cages. Forty minutes later, the mice were anesthetized under 2% isofluorane and imaged an Inveon microPET (Siemens Preclinical, Knoxville TN) for 20 min. Data from all possible lines of response (LOR) were saved in the list mode raw data format. The raw data was then binned into 3D sinograms with a span of 3 and ring difference of 47. The images were reconstructed into transaxial slices (128 x 128 x 159) with voxel sizes of 0.0815 x 0.0815 x 0.0796 cm^3, using the MAP algorithm with 16 subsets, 4 iterations, and a beta of 0.0468. For anatomical co-registration, immediately following the PET scans, the mice received a CT scan in a NanoSPECT/CT (Mediso, Washington DC) at an x-ray beam intensity of 90 mAs and x-ray peak voltage of 45 kVp. The CT images were reconstructed into 170 x 170 x 186 voxels at a voxel size of 0.4 x 0.4 x 0.4 mm^3. The PET-CT images were uploaded into Amide (www.sourceforge.com)

and volumetric regions-of-interest were drawn around the tumors. The PET images were normalized to the injected dose and the mean radiotracer concentration within the ROIs were determined.

^{18}F autoradiography

Mice were handled and injected similarly to previously described for the PET-CT imaging, but without overnight fasting. Tumors were harvested, embedded in optimal cutting temperature compound (OCT, Fisher 23-730-571), and frozen on dry ice. Tumors were cut into 10μm sections and imaged in a Beta Imager (Biospacelabs, France) for 1 hr. Regions-of-interest (ROIs) were drawn around the resulting tumor and spleen images and the counts in each ROI were compared.

In vivo *^{18}F-FDG and ^{18}F-Gln nutrient uptake assay*

Tumor-bearing mice were retro-orbitally injected with 1mCi of FDG or ^{18}F-Gln synthesized at VUMC (Hassanein et al 2016). During radiotracer uptake, mice were conscious and had access to food and water. Mice were euthanized and spleen and tumors were harvested 40min after radiotracer administration. Single cell suspensions of splenocytes were prepared by physical dissociation followed by ACK-lysis. Tumors were chopped, mechanically dissociated on the Miltenyi gentleMACS™ Octo Dissociator with Heaters (setting implant tumor one) and digested in 435U/mL deoxyribonuclease I (Sigma-Aldrich, D5025) and 218U/mL collagenase (Sigma-Alrich, C2674) at 37°C for 30min. After enzyme treatment, tumors were passed through a 70μm filter and ACK-lysed. Cells were resuspended in MACS buffer (PBS +2% FBS +2mM EDTA) and counted using trypan blue with the TC20™ Automated Cell Counter (Bio-Rad). In some cases, tumors from different mice were pooled to achieve higher tumor cell number prior to fractionation

to ensure sufficient ^{18}F signal and were ultimately analyzed as biological replicates. Next, tumor cell suspensions were fractionated using serial magnetic bead positive selection according to the manufacturer's instructions (all Miltenyi mouse kits: CD45 TIL 130-110-618, EPCAM 130-105-958, Thy1.1 130-121-273, CD4/8 TIL 130-116-480, CD11b 130-049-601, F4/80 130-110-443, Gr1 130-094-538, CD11c 130-125-835, CD8 TIL 130-116-478, CD4 TIL 130-116-475). Briefly, cells were resuspended at 10 million total cells/90μL MACS buffer and 10μL microbeads for 15min. Then, cell suspensions were applied to LS columns (Miltenyi 130-042-401) in Miltenyi QuadroMACS™ Separators, washed, and eluted according to manufacturer's instructions. Fractions were resuspended in 1mL of media; 10μL were used for trypan blue staining and TC20 cell count, ~50μL were stained for flow cytometry determination of fraction cellular composition, and 900μL were transferred into 5mL tubes to measure radioactivity. 900μL of 2mL splenocyte suspensions and 5 million total cells from the unfractionated whole tumor were also assayed for radioactivity. The Hidex Automatic Gamma Counter was used with 1min read times to measure time-normalized ^{18}F counts per minute (CPM) for each sample. To determine per cell ^{18}F-nutrient avidity, time-normalized CPM was divided by the number of viable cells as determined by trypan count. Harvested tissues and cell fractions were kept on ice or at 4°C in RPMI 1640 supplemented with 10% FBS except when noted.

Flow cytometry

Single cell suspensions obtained from tumors and spleens were incubated in F_c block (1:50, BD 553142) for 10min at room temp, stained for surface markers for 15min at room temp, washed with FACS buffer (PBS +2% FBS) once, and resuspended in FACS buffer for analysis on a Miltenyi MACSQuant Analyzer 10 or 16. For intracellular staining, the eBioscience™ Foxp3/transcription factor staining buffer kit (Fisher 00-5523-00) was used. For intracellular

cytokine staining, tumor single cell suspensions were incubated for 4hr at 37°C 5% CO_2 in supplemented RPMI with PMA (50ng/mL, Sigma Aldrich P8139-1MG), ionomycin (750ng/mL, Sigma Aldrich I0634-1MG), and GolgiPlug (1:1000, BD 555029), and processed using the BD Cytofix/Cytoperm™ Fixation and Permeabilization Solution (ThermoFisher BDB554722). Surface staining was performed as described above, cells were fix/permed for 20min at 4°C, and then stained for intracellular markers for at least 30min at 4°C. Ghost Dye Red 780 viability dye (1:4000, Cell Signaling 18452S) was used identically to surface antibodies. The anti-mouse and cross-reactive antibodies used were: CD45 BV510 (1:1600, 30-F11, Biolegend 103138), B220 e450 (1:400, RA3-6B2, ThermoFisher 48-0452-82), CD11b e450 (1:1600, M1/70, ThermoFisher 48-0112-82), CD11b FITC (1:1600, M1/70, Biolegend 101206), CD8a AF488 (1:1600, 53-6.7, Biolegend 100723), CD8a BV510 (1:600, 53-6.7, BD 563068), CD8a APC (1:200, 53.6-7, BD 17-0081-82), Ly6C FITC (1:4000, HK1.4, Biolegend 128006), CD11c PE (1:1000, N418, BioLegend 117308), FOXP3 PE (1:125, FJK-16s, ThermoFisher 12-5773-82), pS6 Ser235/236 PE (1:100, D57.2.2E, Cell Signaling 5316S), CD4 PerCP-Cy5.5 (1:600, RM4-5, BioLegend 100540), Ly6G PerCP-Cy5.5 (1:800, 1A8, BioLegend 127616), F4/80 PE-Cy7 (1:800, BM8, BioLegend 123114), NKp46 PE-Cy7 (1:200, 29A1.4, BioLegend 137618), CD3 PE-Cy7 (1:200, 17A2, BioLegend 100220), CD3 FITC (1:200, 17A2, BioLegend 100204), CD3 APC (1:200 17A2, BioLegend 100236), CD206 APC (1:500, C068C2, BioLegend 141708), GLUT1 AF647 (1:500, EPR3915, Abcam ab195020), EPCAM PE (1:1500, G8.8, BioLegend 118206), Thy1.1 PerCP-Cy5.5 (1:2000, HIS51, ThermoFisher 45-0900-82), Thy1.1 FITC (1:2000, HIS51, ThermoFisher 11-0900-85), CD45 PE (1:1600, 30-F11, ThermoFisher 12-0451-83), Ly6C BV570 (1:400, HK1.4, BioLegend 128030), CD68 BV605 (1:200, FA-11, BioLegend 137021), HK1 AF647 (1:100, EPR10134(B), Abcam ab197864), HK2 AF647 (1:200, EPR20839, Abcam

EPR20839), CD71 APC (1:100, RI7217, BioLegend 113820), CD98 PE (1:400, RL388, ThermoFisher 12-0981-81), MHCII I-A/I-E APC (1:4000, M5/114.15.2, BioLegend 107614), CD103 PE-Cy7 (1:200, 2E7, BioLegend 121425), LAG3 e450 (1:100, eBioC9B7W, ThermoFisher 48-2231-82), PD1 PE (1:100, 29F-1A12, BioLegend 135206), TIM3 APC (1:100, RMT3-23, BioLegend 119706), IFNγ APC (1:250, XMG1.2, BioLegend 505810), CD25 e450 (1:500, PD61.5, ThermoFisher 48-0251-82), CD44 PE-Cy7 (1:1000, IM7, BioLegend 103030), and CD62L APC (1:200, MEL-14, ThermoFisher 17-0621-82), CD69 FITC (1:200, H1.2F3, BioLegend), TCF1 AF647 (1:200, C64D9, Cell Signaling), TBET PE-Cy7 (1:100, eBio4B10, eBioscience 25-5825-82), EOMES PE (1:100, Dan11mag, eBioscience 12-4875-82), Perforin APC (1:100, eBioOMAK-D, eBioscience 17939280), Granzyme B PE (1:100, NGZB, eBioscience 12-8898-80), IL-2 PE (1:100, BD 554428), and TNFα PE-Cy7 (1:200, MP6-XT22, BioLegend 506324). The anti-human antibodies used were: CD45 BV421 (1:400, HI30, BioLegend 304032), CD3 APC (1:200, UCHT1, BioLegend 300439), CD11b PerCP-Cy5.5 (1:200, ICRF44, BioLegend 301328), CD14 BV510 (1:200, M5E2, BioLegend 301842), CA9 AF647 (1:200, 303123, R&D Systems FAB2188R-100UG), and Human Fc Block (1:50, BD 564220). For *in vivo* intravenous CD45 PE labelling, MC38 tumor-bearing mice were injected with 5μg anti-CD45 PE diluted to 150 μL in PBS via tail vein and euthanized 5min later. For *ex vivo* fluorescent palmitate uptake, tumor single cell suspensions were incubated for 1hr in Krebs buffer (125mM NaCl, 2.5mM KCl, 25mM $NaHCO_3$, 1mM NaH_3PO_4, 1mM $MgCl_2$, 2.5mM $CaCl_2$, pH 7.2) at 37°C 5% CO_2, incubated with BODIPY™ FL C16 (1μM in Krebs buffer, Thermo D3821) for 45min, washed twice with FACS, and then stained for surface markers. For the myeloid suppression assay, microbead-isolated CD11b+ myeloid cells were co-incubated with 100,000 CellTrace Violet-labelled (CTV, Thermo C34557) OT-I splenocytes per well in a

96-well plate in the presence of 1μg/mL SIINFEKL peptide for 3 days prior to analysis by flow cytometry. Mitochondrial mass was measured with 200nM MitoTracker Green FM (Invitrogen M7514) and mitochondrial membrane potential was measured with 150nM TMRE (Lifetech T-669) staining for 30min at 37°C 5% CO_2 in complete media. Flow cytometry data were analyzed using FlowJo v10.7.1. NIH Tetramer Core Facility for provided the SIINFEKL PE tetramer (1:1000).

In vivo *2NBDG and flow sorting*

2NBDG (Cayman Chemical 11046) was dissolved in PBS at 5 mM (1.71 mg/mL) and 100μL (500ng) was injected retro-orbitally. Mice were sacrificed 40 minutes later and tumor cells and splenocytes were harvested as indicated above. Splenic T cells were isolated according to manufacturer's instructions using the Pan T cell Isolation Kit (Miltenyi 130-095-130). $2NBDG^{hi/lo}$ cells were collected on the Nanocellect (San Diego, USA) WOLF cell sorter and subsequently gamma counted as described in the ^{18}F-FDG and ^{18}F-Gln nutrient uptake assay.

Immunohistochemistry and light microscopy

MC38 tumors were fixed overnight in 10% formalin and then switched to 70% ethanol. Single color IHC was performed by Vanderbilt University Medical Center Translation Pathology Shared Resource. Staining was conducted on the Leica Bond Max IHC stainer. All steps besides dehydration, clearing and coverslipping are performed on the Bond Max. Slides were first deparaffinized. Antigen retrial and antibody dilution were altered for maximal staining with each antibody. For CD11b staining (Catalog # NB110-89474, Novus Biologicals, Centennial, CO) slides were placed in a Protein Block (Ref# x0909, DAKO, Carpinteria, CA) for 10min prior to staining. Then, the slides were incubated in epitope retrieval 2 solution for ten minutes, and

subsequently stained (1:10,000 dilution). For CD3 staining (Ab16669, abcam, Cambridge, MA), epitope retrieval 2 solution for 10min prior to staining (1:250 dilution). For F4/80 staining (NB600-404, Novus Biologicals LLC, Littleton, CO), epitope retrieval was conducted in proteinase K for 5 minutes prior to primary antibody staining (1:300 dilution). Rabbit anti rat secondary (BA-4001, Vector Laboratories, Inc., Burlingame, CA) was used at a 1:2000 dilution for 15min for antigen detection. For CD31 staining (Cat.# DIA-310, Dianova, Hamburg, Germany,), epitope retrieval occurred in epitope retrieval 2 solution for 20min and then subsequently stained (1:75ul dilution). Staining with Biotinylated anti rat (Cat.# BA-4000, Vector Laboratories, Inc., Burlingame, CA) was used for antigen detection at a 1:2000 dilution for 15min. For CD45lca staining (cat# HS-427 017, SySy (Synaptic Systems), Goettingen, Germany) epitope retrieval occurred in epitope retrieval solution 2 for 20min, followed by primary antibody (1:500 dilution. Rabbit anti-rat secondary (BA-4001, Vector Laboratories, Inc., Burlingame, CA) was used at a 1:2000 dilution for 15min to detect the antigen. The Bond Refine (DS9800, Buffalo Grove, IL, USA) detection system was used for visualization. Images were captured using an Olympus BX53 microscope (Olympus Corporation, Center Valley, PA), an Olympus DP73 camera, and Olympus cellSens Standard imaging software version 1.17. Low-power images were captured with a 4X objective lens and high-power images were captured with a 40X objective lens.

MC38 anti-F4/80 microbead-fractionated TAM were mounted onto slides using Wescor Cytopro cytocentrifuge and stained with hematoxylin and eosin following manufacturer's guidelines (Fisher 23-122952). Images were captured under oil immersion (100x objective) using an Olympus

BX53 microscope (Olympus Corporation, Center Valley, PA), an Olympus DP73 camera, and Olympus cellSens Standard imaging software.

Extracellular flux assay

Tumor cell fractions were obtained as described above. Each fraction was plated at 200,000 live cells/well in technical quadruplicate on a Cell-Tak-coated plate (Corning 354240) in Agilent Seahorse RPMI 1640 supplemented with 10mM glucose, 1mM sodium pyruvate, and 2mM glutamine. Cells were analyzed on a Seahorse XFe 96 bioanalyzer using the Mitostress assay (Agilent 103015–100) with 1μM oligomycin, 2μM FCCP, and 0.5μM rotenone/antimycin A. For *in vitro* activated T cells, 150,000 live cells/well were plated. Data were analyzed in Agilent Wave software version 2.6.

Cell sorting and mRNA transcript analysis

$CD45^+$ and $CD45^-$ tumor cell fractions were obtained as described above. Cell fractions were stained for the indicated surface markers and viability dye and sorted on a BD FACSAria III cell sorter. RNA was isolated from tumor cell populations and unstained whole tumor single cell suspensions using the Quick-RNA™ Microprep Kit (Zymo R1050) according to manufacturer's instructions. RNA transcripts were quantified using the NanoString nCounter Metabolic Pathways Gene Expression Panel (XT-CSO-MMP1-12) according to manufacturer's instructions. Transcript counts of 768 genes enriched in cellular metabolic pathways were analyzed using NACHOv1.0.1 (Canouil et al 2020), an R package for parsing, visualization, quality control, and normalization designed for NanoString nCounter data. While parsing raw transcript counts, manufacturer-designated housekeeping genes were used to normalize between samples: *Abcf1*, *Agk*, *Cog7*, *Dhx16*, *Dnajc14*, *Edc3*, *Fcf1*, *G6Pdx*, *Mrps5*, *Nrde2*, *Oaz1*, *Polr2a*, *Sap130*, *Shda*, *Stk11ip*,

Tbc1d10b, *Tbp*, *Tlk2*, *Ubb*, *Usp39*. Sample quality was evaluated based on normal ranges provided by the manufacture for 1) binding density (0.1-2.25), 2) Field of View (<75), 3) Positive Control Linearity (<0.95), and 4) limit of detection (<2). Samples were excluded if they failed any of the four conditions. The third replicates of M-MDSC Rapa and CD4 Rapa were excluded as outliers for abnormal positive control linearity and limit of detection, respectively. Normalization was performed using geometric means based on housing genes, positive, and negative controls. The normalized data from this experiment has been deposited in Geo and can be accessed at GSE165223. Principal component analysis was performed using "FactoMineRv2.3" (Lê et al 2008) package in R. Differentially expressed metabolic genes were identified using a one-way ANOVA performed on transcript count across samples. P-values were adjusted for multiple testing using Benjamini & Hochberg false discovery rate using the "p.adjust" R function. For metabolic genes passing an adjusted p-value <0.01, we performed hierarchical clustering across samples and genes using default settings with the 'seaborn' package (version v0.11.0) in Python. Based on the hierarchical clustering, we grouped genes and performed gene set enrichment analyses using gProfiler (Raudvere et al 2019) with Reactome gene sets compared to all genes. "Metabolism" was the most highly enriched pathway for each cell type and was excluded from bar graphs for space. Differentially expressed genes between the rapamycin and vehicle treated samples for each cell type were identified using "edgeR" (Robinson et al 2010) (version 3.28.1). First, the dispersion (variance of transcript counts) was estimated using the function "estimateDisp". Next, the differential expression between conditions was evaluated using a likelihood ratio test for a negative binomial generalized log-linear model. We considered transcripts with a false discovery rate < 10% and/or a 2-tailed t-test p-value <0.01 as being differentially expressed. All analyses were performed using the R (version 4.0.2).

Protein quantification

Whole cell lysate was extracted using radioimmunoprecipitation assay (RIPA) buffer supplemented with 1x Halt protease and phosphatase inhibitors (Thermo Fisher Scientific). Protein concentration was quantified with a Pierce BCA assay (Thermo Fisher 23227).

CyTOF Mass Cytometry analysis of patient CAR T cells

Samples were collected from two advanced Non-Hodgkin Lymphoma patients receiving Axicabtagene ciloleucel therapy as standard of care. Patient CAR T cell sample collection was approved by the Vanderbilt University Medical Center IRB (#171340).

All mass cytometry antibodies and concentrations used for analysis can be found in Table 6.1. Primary conjugates of mass cytometry antibodies were prepared using the MaxPAR antibody conjugation kit (Fluidigm, South San Francisco, CA) according to the manufacturer's recommended protocol sourcing metals from Fluidigm (Fluidigm, South San Francisco, CA)

For experiments with human samples, blood and was obtained from two advanced Non-Hodgkin Lymphoma patients receiving axicabtagene ciloleucel therapy as standard of care. Residual CAR T product was rinsed from infusion bags immediately following infusion completion and frozen until analysis. Within two hours of blood collection, patient PBMCs were isolated by centrifugation in CPT tubes (BD, Franklin Lakes, NJ) and frozen at 80°C until analysis. PBMCs isolated from advanced non-Hodgkin Lymphoma patients as above were thawed, washed in RPMI media supplemented with 10% FBS, glutamine, HEPES, and beta mercaptoethanol, and rested for 15min in media at 37°C, 5% CO2. Cells were counted,

and then dispensed into a 96-well plate for staining. Cells were stained in 200nM cisplatin, washed, stained with surface antibodies, washed, fixed with 1.6% PFA, washed, permeabilized in methanol, washed, stained with intracellular antibodies, washed, and resuspended with 191/193Ir DNA intercalator overnight at 4°C as above. Mass cytometry samples were washed, resuspended to 500,000 cells/mL containing bead standards for acquisition on a Helios mass cytometer.

Table 6.1: Metal-conjugated CyTOF antibodies used for patient CAR T cell analysis

Channel	Marker	Vendor	Catalog No.	Clone	Species	[Optimal] (μg/ml)
89Y	CD45	Fluidigm	3089003B	HI30	Human	2.5
141Pr	CD49d	Fluidigm	3141004B	9F10	Human	2.5
142Nd	TOX	Miltenyi	130-126-455	REA473	Human	5
143Nd	CD278/ICOS	Fluidigm	3143025B	C398.4A	Human	2.5
144Nd	ATP5a	Abcam	ab110273	7H10BD4F9	Human	2.5
145Nd	CAR	Kite Pharma	Custom	KIP3	Human	2.5
146Nd	CD197 (CCR7)	BioLegend	353237	G043H7	Human	2.5
147Sm	CD183 (CXCR3)	BioLegend	353733	G025H7	Human	2.5
148Nd	CPT1a	Abcam	ab128568	8F6AE9	Human	2.5
149Sm	CD29	BioLegend	303021	TS2/16	Human	1.25
150Nd	CD134 (OX40)	Fluidigm	3150023B	ACT35	Human	2.5
151Eu	Grim19	Abcam	ab110240	6E1BH7	Human	5
152Sm	CD95 (Fas)	Fluidigm	3152017B	DX2	Human	2.5
153Eu	HIF1a	CST	36169	D1S7W	Human	10
154Sm	TIM-3	Fluidigm	3154010B	F38-2E2	Human	2.5
155Gd	CD279 (PD-1)	Fluidigm	3155009B	EH12.2H7	Human	2.5
156Gd	Eomes	Miltenyi	81493BF	D8D1R	Human	5
158Gd	CD137/4-1BB	Fluidigm	3158013B	4B4-1	Human	2.5
159Tb	Glud1	Abcam	ab168352	EPR11370	Human	5
160Gd	XBP1s	CST	27901	E8C2Z	Human	5
161Dy	T-bet	Fluidigm	3161014B	4B10	Human	10
162Dy	CD27	Fluidigm	3162009B	L128	Human	2.5
163Dy	Glut1	Novus	NB110-39113	polyclonal	Human	1.25
164Dy	CytoC	BD	556432	6H2.B4	Human	0.625
165Ho	CD45RO	Fluidigm	3165011B	UCHL1	Human	2.5
166Er	CD28	BioLegend	302937	CD28.2	Human	2.5
167Er	TCF1	Miltenyi	2203BF	C63D9	Human	5
168Er	CD8a	Fluidigm	3168002B	SK1	Human	2.5
169Tm	CD45RA	Fluidigm	3169008B	HI100	Human	2.5
170Er	CD3	Fluidigm	3170001B	UCHT1	Human	2.5
171Yb	Granzyme B	Fluidigm	3171002B	GB11	Human	2.5
172Yb	Ki67	Fluidigm	3172024B	B56	Human	2.5
173Yb	CD223/LAG-3	BioLegend	369302	11C3C65	Human	2.5
174Yb	CD4	Fluidigm	3174004B	SK3	Human	2.5
175Lu	Perforin	Fluidigm	3175004B	B-D48	Human	5
176Yb	CD127	Fluidigm	3176004B	A019D5	Human	2.5

T cell culturing and adoptive transfer

OT-I Thy1.12 mouse splenocytes were ACK-lysed and resuspended to 2 million splenocytes/mL in complete RPMI media supplemented with 10% FBS, pen/strep, HEPES, glutamine, and β-mercaptoethanol, or in complete RPMI without glutamine. OT-I cells were activated with 100 IU/mL recombinant human IL-2 (NCI) and 10ng/mL SIINFEKL peptide. CB839 (vehicle DMSO) and DON (vehicle PBS) were added to a final concentration of 1μM (Johnson et al 2018, Leone et al 2019, Nabe et al 2018). 24hr later, CD8 T cells were isolated via negative selection using the CD8 isolation kit (Miltenyi 130-095-236) according to manufacturer instructions and T cells were resuspended at 200,000 cells/mL in media plus drug and 100IU/mL rhIL-2. For bulk processing of cells prior to 24hr for extracellular flux analysis, RNAseq, and CUT&RUNseq, OT-I cells were always isolated with a CD8 isolation kit and purity was always checked by flow cytometry. 500,000 48hr-activated OT-I cells were transferred into mice via retroorbital injection. For transfer of persisting memory-like cells into a second recipient, Thy1.1 positive selection beads were used on splenocytes, purity was measured by flow cytometry, and 400 OT-I cells were transferred into recipient mice with carrier splenocytes before Lm-OVA infection the next day.

Lm-OVA infection

Listeria monocytogenes expressing OVA (Lm-OVA) was generated by Aduro Biotech and provided by the Mary Philip lab (Gomathinayagam et al 2009). Lm-OVA was stored at -80°C. Mice were injected intraperitoneally with $1x10^7$ CFU.

Adipose tissue processing to single cells

Gonadal adipose tissue was dissected from mice and minced with scissors in FACS buffer. To isolate the stromal vascular fraction, minced adipose tissue was incubated for 30min with rocking in FACS buffer supplemented with 4mg/mL Type II collagenase (Worthington LS00418) and 0.25mg/mL DNase 1, passed through a 100μm filter, ACK-lysed, and filtered again prior to analysis.

RNA-sequencing

RNA was extracted from isolated T cells using the Quick-RNA™ Microprep Kit (Zymo R1050) according to manufacturer's instructions. Quality control analysis was performed and mRNA enrichment and cDNA library preparation utilizing the stranded mRNA (polyA-selected) library preparation kit was performed. Sequencing was performed at Paired-End 150 bp on the Illumina NovaSeq 6000 targeting an average of 50M reads per sample. Library preparation and sequencing occurred at the Vanderbilt Technologies for Advanced Genomics (VANTAGE). Raw read quality was assessed using FastQC (v0.11.5). STAR (v2.7.3a) was used to align reads to the mouse genome (GRCm38.primary assembly from gencode). The transcript quantification was done using featureCounts using the pair-end mode to count both reads that mapped uniquely. Then the differentially expressed genes were called using edgeR (v2.26.5) with Benjamini-Hochberg adjusted p-value < 0.05. Multidimensional scaling analysis (MDS) was done within edgeR.

CUT&RUNseq

CUT&RUN was performed using a CUT&RUN kit (Cell Signaling, CUT&RUN Assay Kit, Cat#86652) with a magnetic based method. Briefly, 250,000 cells were harvested by centrifugation (600g, 3 min) and washed twice with kit wash buffer. The cells were resuspended in 100µl wash buffer and mixed with 10µl pre-activated Concanavalin A beads on a rotator for 5min. Then cells were incubated in antibody binding buffer containing either 2.5µl H3K27me3 antibody (Cell Signaling 9733S), 2.5µl H3K27ac antibody (Cell Signaling 8173S), or 5µl IgG control and incubated at 4°C for 2hr on a rotator. Beads were then washed once in digitonin buffer and resuspended in 100 µl digitonin buffer containing 1.5µl pAG-MNase and incubated at 4°C for 1hr on a rotator. After 2 washes with digitonin buffer beads were resuspended in 150µl digitonin buffer and pAG-MNase was activated with the addition of 3µl $CaCl_2$ to a final concentration of 2 mM. Beads incubated in a ice/water mix for 30min to digest, and the reaction was quenched with 150µl stop buffer. Cleaved fragments were liberated into the supernatant by incubating the beads at 37°C for 10min. DNA fragments were extracted from the supernatant and uniquely dual indexed libraries were prepared. Sequencing was performed at PE 150 on the NovaSeq 6000 targeting an average of 10M reads per sample. Library preparation and sequencing occurred at the Vanderbilt Technologies for Advanced Genomics (VANTAGE). Paired-end fragments were first trimmed with Trimmomatic (version 0.39) to remove adapter and low-quality nucleotides and then mapped to the mouse genome GRCm38.p6 using bowtie2 (version 2.3.5.1) with options: --local --very-sensitive-local --no-unal --no-mixed --no-discordant --phred33 -k 1 -I 10 -X 700. Then the alignment SAM files were transformed to BAM and BIGWIG files using samtools (version 1.9) and deeptools (version 3.3.1) for the following data analysis and visualization. For mapping signal around gene promoters, the gene annotation track

(geocode version 23 known genes track) was downloaded from the UCSC table browser as a bed file and used as reference for heatmaps. MACS2 (version 2.2.7.1) was used for calling peaks with options: --broad -p 1e-5 -f BAMPE --keep-dup all.

Quantification and statistical analysis

Graphs and statistical tests were generated using GraphPad Prism 9 unless otherwise noted. Sample sizes were chosen based on previous studies. Graphs show mean and SEM unless otherwise stated.

REFERENCES

Adams, W. C., Chen, Y. H., Kratchmarov, R., Yen, B., Nish, S. A., Lin, W. H. W., ... & Reiner, S. L. (2016). Anabolism-associated mitochondrial stasis driving lymphocyte differentiation over self-renewal. Cell reports, 17(12), 3142-3152.

Ahluwalia, G. S., Grem, J. L., Hao, Z., & Cooney, D. A. (1990). Metabolism and action of amino acid analog anti-cancer agents. Pharmacology & therapeutics, 46(2), 243-271.

Andrejeva, G., & Rathmell, J. C. (2017). Similarities and distinctions of cancer and immune metabolism in inflammation and tumors. Cell metabolism, 26(1), 49-70.

Angelin, A., Gil-de-Gómez, L., Dahiya, S., Jiao, J., Guo, L., Levine, M. H., ... & Beier, U. H. (2017). Foxp3 reprograms T cell metabolism to function in low-glucose, high-lactate environments. Cell metabolism, 25(6), 1282-1293.

Balmer, M. L., Ma, E. H., Thompson, A. J., Epple, R., Unterstab, G., Lötscher, J., ... & Hess, C. (2020). Memory CD8+ T cells balance pro-and anti-inflammatory activity by reprogramming cellular acetate handling at sites of infection. Cell metabolism, 32(3), 457-467.

Banerjee, A., Gordon, S. M., Intlekofer, A. M., Paley, M. A., Mooney, E. C., Lindsten, T., ... & Reiner, S. L. (2010). Cutting edge: The transcription factor eomesodermin enables CD8+ T cells to compete for the memory cell niche. The Journal of Immunology, 185(9), 4988-4992.

Bantug, G. R., Fischer, M., Grählert, J., Balmer, M. L., Unterstab, G., Develioglu, L., ... & Hess, C. (2018). Mitochondria-endoplasmic reticulum contact sites function as immunometabolic hubs that orchestrate the rapid recall response of memory CD8+ T cells. Immunity, 48(3), 542-555.

Becker, C., Fantini, M. C., Wirtz, S., Nikolaev, A., Kiesslich, R., Lehr, H. A., ... & Neurath, M. F. (2005). In vivo imaging of colitis and colon cancer development in mice using high resolution chromoendoscopy. Gut, 54(7), 950-954.

Bengsch, B., Johnson, A. L., Kurachi, M., Odorizzi, P. M., Pauken, K. E., Attanasio, J., ... & Wherry, E. J. (2016). Bioenergetic insufficiencies due to metabolic alterations regulated by the inhibitory receptor PD-1 are an early driver of CD8+ T cell exhaustion. Immunity, 45(2), 358-373.

Blank, C. U., Haining, W. N., Held, W., Hogan, P. G., Kallies, A., Lugli, E., ... & Zehn, D. (2019). Defining 'T cell exhaustion'. Nature Reviews Immunology, 19(11), 665-674.

Brand, A., Singer, K., Koehl, G. E., Kolitzus, M., Schoenhammer, G., Thiel, A., ... & Kreutz, M. (2016). LDHA-associated lactic acid production blunts tumor immunosurveillance by T and NK cells. Cell metabolism, 24(5), 657-671.

Britt, E. C., John, S. V., Locasale, J. W., & Fan, J. (2020). Metabolic regulation of epigenetic remodeling in immune cells. Current opinion in biotechnology, 63, 111-117.

Buck, M. D., O'Sullivan, D., Geltink, R. I. K., Curtis, J. D., Chang, C. H., Sanin, D. E., ... & Pearce, E. L. (2016). Mitochondrial dynamics controls T cell fate through metabolic

programming. Cell, 166(1), 63-76.

Canouil, M., Bouland, G. A., Bonnefond, A., Froguel, P., 't Hart, L. M., & Slieker, R. C. (2020). NACHO: an R package for quality control of NanoString nCounter data. Bioinformatics, 36(3), 970-971.

Carr, E. L., Kelman, A., Wu, G. S., Gopaul, R., Senkevitch, E., Aghvanyan, A., ... & Frauwirth, K. A. (2010). Glutamine uptake and metabolism are coordinately regulated by ERK/MAPK during T lymphocyte activation. The Journal of Immunology, 185(2), 1037-1044.

Chafe, S. C., McDonald, P. C., Saberi, S., Nemirovsky, O., Venkateswaran, G., Burugu, S., ... & Dedhar, S. (2019). Targeting hypoxia-induced carbonic anhydrase IX enhances immune-checkpoint blockade locally and systemically. Cancer Immunol Res 7 (7): 1064–1078.

Chang, C. H., Qiu, J., O'Sullivan, D., Buck, M. D., Noguchi, T., Curtis, J. D., ... & Pearce, E. L. (2015). Metabolic competition in the tumor microenvironment is a driver of cancer progression. Cell, 162(6), 1229-1241.

Chang, J. T., Palanivel, V. R., Kinjyo, I., Schambach, F., Intlekofer, A. M., Banerjee, A., ... & Reiner, S. L. (2007). Asymmetric T lymphocyte division in the initiation of adaptive immune responses. science, 315(5819), 1687-1691.

Chen, D. S., & Mellman, I. (2013). Oncology meets immunology: the cancer-immunity cycle. immunity, 39(1), 1-10.

Choi, B. K., Lee, D. Y., Lee, D. G., Kim, Y. H., Kim, S. H., Oh, H. S., ... & Kwon, B. S. (2017). 4-1BB signaling activates glucose and fatty acid metabolism to enhance CD8+ T cell proliferation. Cellular & molecular immunology, 14(9), 748-757.

Chowdhury, P. S., Chamoto, K., Kumar, A., & Honjo, T. (2018). PPAR-induced fatty acid oxidation in T cells increases the number of tumor-reactive CD8+ T cells and facilitates anti–PD-1 therapy. Cancer immunology research, 6(11), 1375-1387.

Colegio, O. R., Chu, N. Q., Szabo, A. L., Chu, T., Rhebergen, A. M., Jairam, V., ... & Medzhitov, R. (2014). Functional polarization of tumour-associated macrophages by tumour-derived lactic acid. Nature, 513(7519), 559-563.

Cong, J. (2020). Metabolism of natural killer cells and other innate lymphoid cells. Frontiers in immunology, 1989.

Connelly, L., Barham, W., Onishko, H. M., Chen, L., Sherrill, T. P., Zabuawala, T., ... & Yull, F. E. (2011). NF-kappaB activation within macrophages leads to an anti-tumor phenotype in a mammary tumor lung metastasis model. Breast cancer research, 13(4), 1-14.

Cortese, N., Capretti, G., Barbagallo, M., Rigamonti, A., Takis, P. G., Castino, G. F., ... & Marchesi, F. (2020). Metabolome of pancreatic juice delineates distinct clinical profiles of pancreatic cancer and reveals a link between glucose metabolism and PD-1+ cells. Cancer immunology research, 8(4), 493-505.

Covarrubias, A. J., Aksoylar, H. I., Yu, J., Snyder, N. W., Worth, A. J., Iyer, S. S., ... & Horng, T. (2016). Akt-mTORC1 signaling regulates Acly to integrate metabolic input to control of macrophage activation. elife, 5, e11612.

Davis, R. J., Moore, E. C., Clavijo, P. E., Friedman, J., Cash, H., Chen, Z., ... & Allen, C. (2017). Anti-PD-L1 efficacy can be enhanced by inhibition of myeloid-derived suppressor cells with a selective inhibitor of PI3Kδ/γ. Cancer research, 77(10), 2607-2619.

DeBerardinis, R. J., Mancuso, A., Daikhin, E., Nissim, I., Yudkoff, M., Wehrli, S., & Thompson, C. B. (2007). Beyond aerobic glycolysis: transformed cells can engage in glutamine metabolism that exceeds the requirement for protein and nucleotide synthesis. Proceedings of the National Academy of Sciences, 104(49), 19345-19350.

e Drigo, R. A., Lev-Ram, V., Tyagi, S., Ramachandra, R., Deerinck, T., Bushong, E., ... & Hetzer, M. W. (2019). Age mosaicism across multiple scales in adult tissues. Cell metabolism, 30(2), 343-351.

Esensten, J. H., Helou, Y. A., Chopra, G., Weiss, A., & Bluestone, J. A. (2016). CD28 costimulation: from mechanism to therapy. Immunity, 44(5), 973-988.

Faubert, B., Li, K. Y., Cai, L., Hensley, C. T., Kim, J., Zacharias, L. G., ... & DeBerardinis, R. J. (2017). Lactate metabolism in human lung tumors. Cell, 171(2), 358-371.

Fiore, A., & Murray, P. J. (2021). Tryptophan and indole metabolism in immune regulation. Current Opinion in Immunology, 70, 7-14.

Flood, B. A., Higgs, E. F., Li, S., Luke, J. J., & Gajewski, T. F. (2019). STING pathway agonism as a cancer therapeutic. Immunological reviews, 290(1), 24-38.

Frauwirth, K. A., Riley, J. L., Harris, M. H., Parry, R. V., Rathmell, J. C., Plas, D. R., ... & Thompson, C. B. (2002). The CD28 signaling pathway regulates glucose metabolism. Immunity, 16(6), 769-777.

Ganeshan, K., & Chawla, A. (2014). Metabolic regulation of immune responses. Annual review of immunology, 32, 609-634.

Geltink, R. I. K., O'Sullivan, D., Corrado, M., Bremser, A., Buck, M. D., Buescher, J. M., ... & Pearce, E. L. (2017). Mitochondrial priming by CD28. Cell, 171(2), 385-397.

Gemta, L. F., Siska, P. J., Nelson, M. E., Gao, X., Liu, X., Locasale, J. W., ... & Bullock, T. N. (2019). Impaired enolase 1 glycolytic activity restrains effector functions of tumor-infiltrating CD8+ T cells. Science immunology, 4(31), eaap9520.

Guedan, S., Madar, A., Casado-Medrano, V., Shaw, C., Wing, A., Liu, F., ... & Posey, A. D. (2020). Single residue in CD28-costimulated CAR-T cells limits long-term persistence and antitumor durability. The Journal of clinical investigation, 130(6), 3087-3097.

Hassanein, M., Hight, M. R., Buck, J. R., Tantawy, M. N., Nickels, M. L., Hoeksema, M. D., ... & Manning, H. C. (2016). Preclinical evaluation of 4-[18F] fluoroglutamine PET to assess

ASCT2 expression in lung cancer. Molecular imaging and biology, 18(1), 18-23.

Hesketh, R. L., Wang, J., Wright, A. J., Lewis, D. Y., Denton, A. E., Grenfell, R., ... & Brindle, K. M. (2019). Magnetic resonance imaging is more sensitive than PET for detecting treatment-induced cell death–dependent changes in glycolysis. Cancer research, 79(14), 3557-3569.

Ho, P. C., Bihuniak, J. D., Macintyre, A. N., Staron, M., Liu, X., Amezquita, R., ... & Kaech, S. M. (2015). Phosphoenolpyruvate is a metabolic checkpoint of anti-tumor T cell responses. Cell, 162(6), 1217-1228.

Hoover, A. A., Hufnagel, D. H., Harris, W., Bullock, K., Glass, E. B., Liu, E., ... & Yull, F. E. (2020). Increased canonical NF-kappaB signaling specifically in macrophages is sufficient to limit tumor progression in syngeneic murine models of ovarian cancer. BMC cancer, 20(1), 1-16.

Huang, S. C. C., Smith, A. M., Everts, B., Colonna, M., Pearce, E. L., Schilling, J. D., & Pearce, E. J. (2016). Metabolic reprogramming mediated by the mTORC2-IRF4 signaling axis is essential for macrophage alternative activation. Immunity, 45(4), 817-830.

Jacobs, S. R., Herman, C. E., MacIver, N. J., Wofford, J. A., Wieman, H. L., Hammen, J. J., & Rathmell, J. C. (2008). Glucose uptake is limiting in T cell activation and requires CD28-mediated Akt-dependent and independent pathways. The Journal of Immunology, 180(7), 4476-4486.

Jeong, H., Kim, S., Hong, B. J., Lee, C. J., Kim, Y. E., Bok, S., ... & Ahn, G. O. (2019). Tumor-associated macrophages enhance tumor hypoxia and aerobic glycolysis. Cancer research, 79(4), 795-806.

Jha, A. K., Huang, S. C. C., Sergushichev, A., Lampropoulou, V., Ivanova, Y., Loginicheva, E., ... & Artyomov, M. N. (2015). Network integration of parallel metabolic and transcriptional data reveals metabolic modules that regulate macrophage polarization. Immunity, 42(3), 419-430.

Johnson, M. O., Wolf, M. M., Madden, M. Z., Andrejeva, G., Sugiura, A., Contreras, D. C., ... & Rathmell, J. C. (2018). Distinct regulation of Th17 and Th1 cell differentiation by glutaminase-dependent metabolism. Cell, 175(7), 1780-1795.

June, C. H., & Sadelain, M. (2018). Chimeric antigen receptor therapy. New England Journal of Medicine, 379(1), 64-73.

Kapsenberg, M. L. (2003). Dendritic-cell control of pathogen-driven T-cell polarization. Nature Reviews Immunology, 3(12), 984-993.

Kawalekar, O. U., O'Connor, R. S., Fraietta, J. A., Guo, L., McGettigan, S. E., Posey Jr, A. D., ... & June, C. H. (2016). Distinct signaling of coreceptors regulates specific metabolism pathways and impacts memory development in CAR T cells. Immunity, 44(2), 380-390.

Kilgour, M. K., MacPherson, S., Zacharias, L. G., Ellis, A. E., Sheldon, R. D., Liu, E. Y., ... & Lum, J. J. (2021). 1-Methylnicotinamide is an immune regulatory metabolite in human ovarian cancer. Science advances, 7(4), eabe1174.

Kishore, M., Cheung, K. C., Fu, H., Bonacina, F., Wang, G., Coe, D., ... & Marelli-Berg, F. M. (2017). Regulatory T cell migration is dependent on glucokinase-mediated glycolysis. Immunity, 47(5), 875-889.

Kishton, R. J., Sukumar, M., & Restifo, N. P. (2017). Metabolic regulation of T cell longevity and function in tumor immunotherapy. Cell metabolism, 26(1), 94-109.

Klebanoff, C. A., Crompton, J. G., Leonardi, A. J., Yamamoto, T. N., Chandran, S. S., Eil, R. L., ... & Restifo, N. P. (2017). Inhibition of AKT signaling uncouples T cell differentiation from expansion for receptor-engineered adoptive immunotherapy. JCI insight, 2(23).

Klein Geltink, R. I., Edwards-Hicks, J., Apostolova, P., O'Sullivan, D., Sanin, D. E., Patterson, A. E., ... & Pearce, E. L. (2020). Metabolic conditioning of CD8+ effector T cells for adoptive cell therapy. Nature Metabolism, 2(8), 703-716.

Klein, L., Kyewski, B., Allen, P. M., & Hogquist, K. A. (2014). Positive and negative selection of the T cell repertoire: what thymocytes see (and don't see). Nature Reviews Immunology, 14(6), 377-391.

Klysz, D., Tai, X., Robert, P. A., Craveiro, M., Cretenet, G., Oburoglu, L., ... & Taylor, N. (2015). Glutamine-dependent α-ketoglutarate production regulates the balance between T helper 1 cell and regulatory T cell generation. Science signaling, 8(396), ra97-ra97.

Kohl, A., Kao, K. C., & Ho, P. C. (2021). Can tumor cells take it all away?. Cell Metabolism, 33(6), 1071-1072.

Kono, M., Yoshida, N., Maeda, K., Suárez-Fueyo, A., Kyttaris, V. C., & Tsokos, G. C. (2019). Glutaminase 1 inhibition reduces glycolysis and ameliorates lupus-like disease in MRL/lpr mice and experimental autoimmune encephalomyelitis. Arthritis & Rheumatology, 71(11), 1869-1878.

Kumar, B. V., Connors, T. J., & Farber, D. L. (2018). Human T cell development, localization, and function throughout life. Immunity, 48(2), 202-213.

Kumar, S., & Dikshit, M. (2019). Metabolic insight of neutrophils in health and disease. Frontiers in immunology, 2099.

Lavin, Y., Mortha, A., Rahman, A., & Merad, M. (2015). Regulation of macrophage development and function in peripheral tissues. Nature Reviews Immunology, 15(12), 731-744.

Lê, S., Josse, J., & Husson, F. (2008). FactoMineR: an R package for multivariate analysis. Journal of statistical software, 25, 1-18.

LeBien, T. W., & Tedder, T. F. (2008). B lymphocytes: how they develop and function. Blood, The Journal of the American Society of Hematology, 112(5), 1570-1580.

Lee, M. J., Yun, S. J., Lee, B., Jeong, E., Yoon, G., Kim, K., & Park, S. (2020). Association of TIM-3 expression with glucose metabolism in Jurkat T cells. BMC immunology, 21(1), 1-13.

Lemberg, K. M., Gori, S. S., Tsukamoto, T., Rais, R., & Slusher, B. S. (2022). Clinical development of metabolic inhibitors for oncology. The Journal of clinical investigation, 132(1).

Leone, R. D., Zhao, L., Englert, J. M., Sun, I. M., Oh, M. H., Sun, I. H., ... & Powell, J. D. (2019). Glutamine blockade induces divergent metabolic programs to overcome tumor immune evasion. Science, 366(6468), 1013-1021.

Levine, L. S., Hiam-Galvez, K. J., Marquez, D. M., Tenvooren, I., Madden, M. Z., Contreras, D. C., ... & Spitzer, M. H. (2021). Single-cell analysis by mass cytometry reveals metabolic states of early-activated CD8+ T cells during the primary immune response. Immunity, 54(4), 829-844.

Li, W., Tanikawa, T., Kryczek, I., Xia, H., Li, G., Wu, K., ... & Zou, W. (2018). Aerobic glycolysis controls myeloid-derived suppressor cells and tumor immunity via a specific CEBPB isoform in triple-negative breast cancer. Cell metabolism, 28(1), 87-103.

Liu, P. S., Wang, H., Li, X., Chao, T., Teav, T., Christen, S., ... & Ho, P. C. (2017). α-ketoglutarate orchestrates macrophage activation through metabolic and epigenetic reprogramming. Nature immunology, 18(9), 985-994.

Ma, E. H., Verway, M. J., Johnson, R. M., Roy, D. G., Steadman, M., Hayes, S., ... & Jones, R. G. (2019). Metabolic profiling using stable isotope tracing reveals distinct patterns of glucose utilization by physiologically activated CD8+ T cells. Immunity, 51(5), 856-870.

Mabuchi, S., Komura, N., Sasano, T., Shimura, K., Yokoi, E., Kozasa, K., ... & Kimura, T. (2020). Pretreatment tumor-related leukocytosis misleads positron emission tomography-computed tomography during lymph node staging in gynecological malignancies. Nature communications, 11(1), 1-12.

Macintyre, A. N., Gerriets, V. A., Nichols, A. G., Michalek, R. D., Rudolph, M. C., Deoliveira, D., ... & Rathmell, J. C. (2014). The glucose transporter Glut1 is selectively essential for CD4 T cell activation and effector function. Cell metabolism, 20(1), 61-72.

Madden, M. Z., & Rathmell, J. C. (2021). The complex integration of T-cell metabolism and immunotherapy. Cancer Discovery, 11(7), 1636-1643.

Mantovani, A., Cassatella, M. A., Costantini, C., & Jaillon, S. (2011). Neutrophils in the activation and regulation of innate and adaptive immunity. Nature reviews immunology, 11(8), 519-531.

Maude, S. L., Laetsch, T. W., Buechner, J., Rives, S., Boyer, M., Bittencourt, H., ... & Grupp, S. A. (2018). Tisagenlecleucel in children and young adults with B-cell lymphoblastic leukemia. New England Journal of Medicine, 378(5), 439-448.

Mendoza, A., Fang, V., Chen, C., Serasinghe, M., Verma, A., Muller, J., ... & Schwab, S. R. (2017). Lymphatic endothelial S1P promotes mitochondrial function and survival in naive T cells. Nature, 546(7656), 158-161.

Mengjun, L. G. (2019). TCseq: Time course sequencing data analysis.

Michalek, R. D., Gerriets, V. A., Jacobs, S. R., Macintyre, A. N., MacIver, N. J., Mason, E. F., ... & Rathmell, J. C. (2011). Cutting edge: distinct glycolytic and lipid oxidative metabolic

programs are essential for effector and regulatory CD4+ T cell subsets. The Journal of Immunology, 186(6), 3299-3303.

Michelucci, A., Cordes, T., Ghelfi, J., Pailot, A., Reiling, N., Goldmann, O., ... & Hiller, K. (2013). Immune-responsive gene 1 protein links metabolism to immunity by catalyzing itaconic acid production. Proceedings of the National Academy of Sciences, 110(19), 7820-7825.

Miller, B. C., Sen, D. R., Al Abosy, R., Bi, K., Virkud, Y. V., LaFleur, M. W., ... & Haining, W. N. (2019). Subsets of exhausted CD8+ T cells differentially mediate tumor control and respond to checkpoint blockade. Nature immunology, 20(3), 326-336.

Morris, A. (2018). Inhibiting glycolysis in tumour cells. Nature Reviews Endocrinology, 14(6), 323-323.

Murphy, K., & Weaver, C. (2016). Janeway's immunobiology. Garland science.

Myers, D. R., Norlin, E., Vercoulen, Y., & Roose, J. P. (2019). Active tonic mTORC1 signals shape baseline translation in naive T cells. Cell reports, 27(6), 1858-1874.

Nabe, S., Yamada, T., Suzuki, J., Toriyama, K., Yasuoka, T., Kuwahara, M., ... & Yamashita, M. (2018). Reinforce the antitumor activity of CD 8+ T cells via glutamine restriction. Cancer science, 109(12), 3737-3750.

Nair-Gill, E., Wiltzius, S. M., Wei, X. X., Cheng, D., Riedinger, M., Radu, C. G., & Witte, O. N. (2010). PET probes for distinct metabolic pathways have different cell specificities during immune responses in mice. The Journal of clinical investigation, 120(6), 2005-2015.

Nakagawa, M. M., & Rathinam, C. V. (2018). Constitutive activation of the canonical NF-κB Pathway leads to bone marrow failure and induction of erythroid signature in hematopoietic stem cells. Cell reports, 25(8), 2094-2109.

Nakagawa, M. M., Chen, H., & Rathinam, C. V. (2018). Constitutive activation of NF-κB pathway in hematopoietic stem cells causes loss of quiescence and deregulated transcription factor networks. Frontiers in Cell and Developmental Biology, 143.

Nakaya, M., Xiao, Y., Zhou, X., Chang, J. H., Chang, M., Cheng, X., ... & Sun, S. C. (2014). Inflammatory T cell responses rely on amino acid transporter ASCT2 facilitation of glutamine uptake and mTORC1 kinase activation. Immunity, 40(5), 692-705.

Noe, J. T., Rendon, B. E., Geller, A. E., Conroy, L. R., Morrissey, S. M., Young, L. E., ... & Mitchell, R. A. (2021). Lactate supports a metabolic-epigenetic link in macrophage polarization. Science advances, 7(46), eabi8602.

O'Brien, K. L., & Finlay, D. K. (2019). Immunometabolism and natural killer cell responses. Nature Reviews Immunology, 19(5), 282-290.

O'Neil, R. T., Saha, S., Veach, R. A., Welch, R. C., Woodard, L. E., Rooney, C. M., & Wilson, M. H. (2018). Transposon-modified antigen-specific T lymphocytes for sustained therapeutic protein delivery in vivo. Nature communications, 9(1), 1-10.

O'Neill, L. A. (2015). A broken krebs cycle in macrophages. Immunity, 42(3), 393-394.

O'Neill, L. A., Kishton, R. J., & Rathmell, J. (2016). A guide to immunometabolism for immunologists. Nature Reviews Immunology, 16(9), 553-565.

Okkenhaug, K. (2013). Signaling by the phosphoinositide 3-kinase family in immune cells. Annual review of immunology, 31, 675-704.

Pacella, I., & Piconese, S. (2019). Immunometabolic checkpoints of Treg dynamics: adaptation to microenvironmental opportunities and challenges. Frontiers in immunology, 1889.

Pacella, I., Procaccini, C., Focaccetti, C., Miacci, S., Timperi, E., Faicchia, D., ... & Piconese, S. (2018). Fatty acid metabolism complements glycolysis in the selective regulatory T cell expansion during tumor growth. Proceedings of the National Academy of Sciences, 115(28), E6546-E6555.

Palmer, L. D., Maloney, K. N., Boyd, K. L., Goleniewska, A. K., Toki, S., Maxwell, C. N., ... & Skaar, E. P. (2019). The innate immune protein S100A9 protects from T-helper cell type 2–mediated allergic airway inflammation. American Journal of Respiratory Cell and Molecular Biology, 61(4), 459-468.

Palsson-McDermott, E. M., Curtis, A. M., Goel, G., Lauterbach, M. A., Sheedy, F. J., Gleeson, L. E., ... & O'Neill, L. A. (2015). Pyruvate kinase M2 regulates Hif-1α activity and IL-1β induction and is a critical determinant of the warburg effect in LPS-activated macrophages. Cell metabolism, 21(1), 65-80.

Parang, B., Barrett, C. W., & Williams, C. S. (2016). AOM/DSS model of colitis-associated cancer. In Gastrointestinal Physiology and Diseases (pp. 297-307). Humana Press, New York, NY.

Parry, R. V., Chemnitz, J. M., Frauwirth, K. A., Lanfranco, A. R., Braunstein, I., Kobayashi, S. V., ... & Riley, J. L. (2005). CTLA-4 and PD-1 receptors inhibit T-cell activation by distinct mechanisms. Molecular and cellular biology, 25(21), 9543-9553.

Patrono, C., & Rocca, B. (2009). Nonsteroidal antiinflammatory drugs: past, present and future. Pharmacological Research, 59(5), 285-289.

Patsoukis, N., Bardhan, K., Chatterjee, P., Sari, D., Liu, B., Bell, L. N., ... & Boussiotis, V. A. (2015). PD-1 alters T-cell metabolic reprogramming by inhibiting glycolysis and promoting lipolysis and fatty acid oxidation. Nature communications, 6(1), 1-13.

Pearce, E. J., & Everts, B. (2015). Dendritic cell metabolism. Nature Reviews Immunology, 15(1), 18-29.

Peng, M., Yin, N., Chhangawala, S., Xu, K., Leslie, C. S., & Li, M. O. (2016). Aerobic glycolysis promotes T helper 1 cell differentiation through an epigenetic mechanism. Science, 354(6311), 481-484.

Perry, D. J., Yin, Y., Telarico, T., Baker, H. V., Dozmorov, I., Perl, A., & Morel, L. (2012).

Murine lupus susceptibility locus Sle1c2 mediates CD4+ T cell activation and maps to estrogen-related receptor γ. The Journal of Immunology, 189(2), 793-803.

Philip, M., Fairchild, L., Sun, L., Horste, E. L., Camara, S., Shakiba, M., ... & Schietinger, A. (2017). Chromatin states define tumour-specific T cell dysfunction and reprogramming. Nature, 545(7655), 452-456.

Philipson, B. I., O'Connor, R. S., May, M. J., June, C. H., Albelda, S. M., & Milone, M. C. (2020). 4-1BB costimulation promotes CAR T cell survival through noncanonical NF-κB signaling. Science signaling, 13(625), eaay8248.

Previte, D. M., Martins, C. P., O'Connor, E. C., Marre, M. L., Coudriet, G. M., Beck, N. W., ... & Piganelli, J. D. (2019). Lymphocyte activation gene-3 maintains mitochondrial and metabolic quiescence in naive CD4+ T cells. Cell reports, 27(1), 129-141.

Qiu, J., Villa, M., Sanin, D. E., Buck, M. D., O'Sullivan, D., Ching, R., ... & Pearce, E. L. (2019). Acetate promotes T cell effector function during glucose restriction. Cell reports, 27(7), 2063-2074.

Raudvere, U., Kolberg, L., Kuzmin, I., Arak, T., Adler, P., Peterson, H., & Vilo, J. (2019). g: Profiler: a web server for functional enrichment analysis and conversions of gene lists (2019 update). Nucleic acids research, 47(W1), W191-W198.

Reinfeld, B. I., Madden, M. Z., Wolf, M. M., Chytil, A., Bader, J. E., Patterson, A. R., ... & Rathmell, W. K. (2021). Cell-programmed nutrient partitioning in the tumour microenvironment. Nature, 593(7858), 282-288.

Ringel, A. E., Drijvers, J. M., Baker, G. J., Catozzi, A., García-Cañaveras, J. C., Gassaway, B. M., ... & Haigis, M. C. (2020). Obesity shapes metabolism in the tumor microenvironment to suppress anti-tumor immunity. Cell, 183(7), 1848-1866.

Robinson, M. D., McCarthy, D. J., & Smyth, G. K. (2010). edgeR: a Bioconductor package for differential expression analysis of digital gene expression data. Bioinformatics, 26(1), 139-140.

Rodríguez-Prados, J. C., Través, P. G., Cuenca, J., Rico, D., Aragonés, J., Martín-Sanz, P., ... & Boscá, L. (2010). Substrate fate in activated macrophages: a comparison between innate, classic, and alternative activation. The Journal of Immunology, 185(1), 605-614.

Ron-Harel, N., Ghergurovich, J. M., Notarangelo, G., LaFleur, M. W., Tsubosaka, Y., Sharpe, A. H., ... & Haigis, M. C. (2019). T cell activation depends on extracellular alanine. Cell reports, 28(12), 3011-3021.

Rosenberg, S. A., & Restifo, N. P. (2015). Adoptive cell transfer as personalized immunotherapy for human cancer. Science, 348(6230), 62-68.

Roy, D. G., Chen, J., Mamane, V., Ma, E. H., Muhire, B. M., Sheldon, R. D., ... & Jones, R. G. (2020). Methionine metabolism shapes T helper cell responses through regulation of epigenetic reprogramming. Cell metabolism, 31(2), 250-266.

Ryan, D. G., & O'Neill, L. A. (2020). Krebs cycle reborn in macrophage immunometabolism. Annual review of immunology, 38, 289-313.

Sabharwal, S. S., Rosen, D. B., Grein, J., Tedesco, D., Joyce-Shaikh, B., Ueda, R., ... & Zúñiga, L. A. (2018). GITR agonism enhances cellular metabolism to support CD8+ T-cell proliferation and effector cytokine production in a mouse tumor model. Cancer Immunology Research, 6(10), 1199-1211.

Saxton, R. A., & Sabatini, D. M. (2017). mTOR signaling in growth, metabolism, and disease. Cell, 168(6), 960-976.

Scharping, N. E., Menk, A. V., Moreci, R. S., Whetstone, R. D., Dadey, R. E., Watkins, S. C., ... & Delgoffe, G. M. (2016). The tumor microenvironment represses T cell mitochondrial biogenesis to drive intratumoral T cell metabolic insufficiency and dysfunction. Immunity, 45(2), 374-388.

Scharping, N. E., Rivadeneira, D. B., Menk, A. V., Vignali, P. D., Ford, B. R., Rittenhouse, N. L., ... & Delgoffe, G. M. (2021). Mitochondrial stress induced by continuous stimulation under hypoxia rapidly drives T cell exhaustion. Nature immunology, 22(2), 205-215.

Schildberg, F. A., Klein, S. R., Freeman, G. J., & Sharpe, A. H. (2016). Coinhibitory pathways in the B7-CD28 ligand-receptor family. Immunity, 44(5), 955-972.

Schulte, M. L., Fu, A., Zhao, P., Li, J., Geng, L., Smith, S. T., ... & Manning, H. C. (2018). Pharmacological blockade of ASCT2-dependent glutamine transport leads to antitumor efficacy in preclinical models. Nature medicine, 24(2), 194-202.

Senyilmaz, D., & Teleman, A. A. (2015). Chicken or the egg: Warburg effect and mitochondrial dysfunction. F1000prime reports, 7.

Shang, M., Cappellesso, F., Amorim, R., Serneels, J., Virga, F., Eelen, G., ... & Mazzone, M. (2020). Macrophage-derived glutamine boosts satellite cells and muscle regeneration. Nature, 587(7835), 626-631.

Siddiqui, I., Schaeuble, K., Chennupati, V., Marraco, S. A. F., Calderon-Copete, S., Ferreira, D. P., ... & Held, W. (2019). Intratumoral Tcf1+ PD-1+ CD8+ T cells with stem-like properties promote tumor control in response to vaccination and checkpoint blockade immunotherapy. Immunity, 50(1), 195-211.

Sinclair, L. V., Barthelemy, C., & Cantrell, D. A. (2020). Single cell glucose uptake assays: a cautionary tale. Immunometabolism, 2(4).

Sinclair, L. V., Howden, A. J., Brenes, A., Spinelli, L., Hukelmann, J. L., Macintyre, A. N., ... & Cantrell, D. A. (2019). Antigen receptor control of methionine metabolism in T cells. Elife, 8, e44210.

Sinclair, L. V., Rolf, J., Emslie, E., Shi, Y. B., Taylor, P. M., & Cantrell, D. A. (2013). Control of amino-acid transport by antigen receptors coordinates the metabolic reprogramming essential

for T cell differentiation. Nature immunology, 14(5), 500-508.

Siska, P. J., Beckermann, K. E., Mason, F. M., Andrejeva, G., Greenplate, A. R., Sendor, A. B., ... & Rathmell, J. C. (2017). Mitochondrial dysregulation and glycolytic insufficiency functionally impair CD8 T cells infiltrating human renal cell carcinoma. JCI insight, 2(12).

Spranger, S., Dai, D., Horton, B., & Gajewski, T. F. (2017). Tumor-residing Batf3 dendritic cells are required for effector T cell trafficking and adoptive T cell therapy. Cancer cell, 31(5), 711-723.

Sugiura, A., Andrejeva, G., Voss, K., Heintzman, D. R., Xu, X., Madden, M. Z., ... & Rathmell, J. C. (2022). MTHFD2 is a metabolic checkpoint controlling effector and regulatory T cell fate and function. Immunity, 55(1), 65-81.

Sukumar, M., Liu, J., Ji, Y., Subramanian, M., Crompton, J. G., Yu, Z., ... & Gattinoni, L. (2013). Inhibiting glycolytic metabolism enhances CD8+ T cell memory and antitumor function. The Journal of clinical investigation, 123(10), 4479-4488.

Sullivan, M. R., Danai, L. V., Lewis, C. A., Chan, S. H., Gui, D. Y., Kunchok, T., ... & Muir, A. (2019). Quantification of microenvironmental metabolites in murine cancers reveals determinants of tumor nutrient availability. Elife, 8, e44235.

Szefel, J., Danielak, A., & Kruszewski, W. J. (2019). Metabolic pathways of L-arginine and therapeutic consequences in tumors. Advances in medical sciences, 64(1), 104-110.

Tannahill, G. M., Curtis, A. M., Adamik, J., Palsson-McDermott, E. M., McGettrick, A. F., Goel, G., ... & O'Neill, L. A. J. (2013). Succinate is an inflammatory signal that induces IL-1β through HIF-1α. Nature, 496(7444), 238-242.

Tracz, A., Mastri, M., Lee, C. R., Pili, R., & Ebos, J. M. (2014). Modeling spontaneous metastatic renal cell carcinoma (mRCC) in mice following nephrectomy. JoVE (Journal of Visualized Experiments), (86), e51485.

Tsurutani, N., Mittal, P., Rose, M. C. S., Ngoi, S. M., Svedova, J., Menoret, A., ... & Vella, A. T. (2016). Costimulation endows immunotherapeutic CD8 T cells with IL-36 responsiveness during aerobic glycolysis. The Journal of Immunology, 196(1), 124-134.

van der Windt, G. J., Everts, B., Chang, C. H., Curtis, J. D., Freitas, T. C., Amiel, E., ... & Pearce, E. L. (2012). Mitochondrial respiratory capacity is a critical regulator of CD8+ T cell memory development. Immunity, 36(1), 68-78.

van Teijlingen Bakker, N., & Pearce, E. J. (2020). Cell-intrinsic metabolic regulation of mononuclear phagocyte activation: Findings from the tip of the iceberg. Immunological reviews, 295(1), 54-67.

Vander Heiden, M. G., & DeBerardinis, R. J. (2017). Understanding the intersections between metabolism and cancer biology. Cell, 168(4), 657-669.

Varghese, S., Pramanik, S., Williams, L. J., Hodges, H. R., Hudgens, C. W., Fischer, G. M., ... &

Gopal, Y. V. (2021). The glutaminase inhibitor CB-839 (telaglenastat) enhances the antimelanoma activity of T-cell–mediated immunotherapies. Molecular cancer therapeutics, 20(3), 500-511.

Vitale, I., Manic, G., Coussens, L. M., Kroemer, G., & Galluzzi, L. (2019). Macrophages and metabolism in the tumor microenvironment. Cell metabolism, 30(1), 36-50.

Wang, R., Dillon, C. P., Shi, L. Z., Milasta, S., Carter, R., Finkelstein, D., ... & Green, D. R. (2011). The transcription factor Myc controls metabolic reprogramming upon T lymphocyte activation. Immunity, 35(6), 871-882.

Warburg O. (1956). On the origin of cancer cells. Science, 123:309.

Warburg O., Posener K., Negelein E. (1924). Biochem Z. 152:319.

Watson, M. J., Vignali, P. D., Mullett, S. J., Overacre-Delgoffe, A. E., Peralta, R. M., Grebinoski, S., ... & Delgoffe, G. M. (2021). Metabolic support of tumour-infiltrating regulatory T cells by lactic acid. Nature, 591(7851), 645-651.

Wei, J., Long, L., Zheng, W., Dhungana, Y., Lim, S. A., Guy, C., ... & Chi, H. (2019). Targeting REGNASE-1 programs long-lived effector T cells for cancer therapy. Nature, 576(7787), 471-476.

Wei, S. C., Duffy, C. R., & Allison, J. P. (2018). Fundamental mechanisms of immune checkpoint blockade therapy. Cancer discovery, 8(9), 1069-1086.

Wen, T., & Rothenberg, M. E. (2016). The regulatory function of eosinophils. Microbiology spectrum, 4(5), 4-5.

Wenes, M., Shang, M., Di Matteo, M., Goveia, J., Martín-Pérez, R., Serneels, J., ... & Mazzone, M. (2016). Macrophage metabolism controls tumor blood vessel morphogenesis and metastasis. Cell metabolism, 24(5), 701-715.

Wise, D. R., & Thompson, C. B. (2010). Glutamine addiction: a new therapeutic target in cancer. Trends in biochemical sciences, 35(8), 427-433.

Wofford, J. A., Wieman, H. L., Jacobs, S. R., Zhao, Y., & Rathmell, J. C. (2008). IL-7 promotes Glut1 trafficking and glucose uptake via STAT5-mediated activation of Akt to support T-cell survival. Blood, The Journal of the American Society of Hematology, 111(4), 2101-2111.

Xia, X., Cao, G., Sun, G., Zhu, L., Tian, Y., Song, Y., ... & Gao, Y. (2020). GLS1-mediated glutaminolysis unbridled by MALT1 protease promotes psoriasis pathogenesis. The Journal of clinical investigation, 130(10), 5180-5196.

Xiang, X., Wind, K., Wiedemann, T., Blume, T., Shi, Y., Briel, N., ... & Brendel, M. (2021). Microglial activation states drive glucose uptake and FDG-PET alterations in neurodegenerative diseases. Science translational medicine, 13(615), eabe5640.

Xu, T., Stewart, K. M., Wang, X., Liu, K., Xie, M., Ryu, J. K., ... & Ding, S. (2017). Metabolic control of TH17 and induced Treg cell balance by an epigenetic mechanism. Nature, 548(7666),

228-233.

Yoshida, G. J. (2020). Beyond the Warburg effect: N-Myc contributes to metabolic reprogramming in cancer cells. Frontiers in oncology, 10, 791.

Yu, Y. R., Imrichova, H., Wang, H., Chao, T., Xiao, Z., Gao, M., ... & Ho, P. C. (2020). Disturbed mitochondrial dynamics in CD8+ TILs reinforce T cell exhaustion. Nature immunology, 21(12), 1540-1551.

Zeng, H. U., Cohen, S., Guy, C., Shrestha, S., Neale, G., Brown, S. A., ... & Chi, H. (2016). mTORC1 and mTORC2 kinase signaling and glucose metabolism drive follicular helper T cell differentiation. Immunity, 45(3), 540-554.

Zhang, Y., Kurupati, R., Liu, L., Zhou, X. Y., Zhang, G., Hudaihed, A., ... & Ertl, H. C. (2017). Enhancing CD8+ T cell fatty acid catabolism within a metabolically challenging tumor microenvironment increases the efficacy of melanoma immunotherapy. Cancer cell, 32(3), 377-391.

Zhao, Y., Altman, B. J., Coloff, J. L., Herman, C. E., Jacobs, S. R., Wieman, H. L., ... & Rathmell, J. C. (2007). Glycogen synthase kinase 3α and 3β mediate a glucose-sensitive antiapoptotic signaling pathway to stabilize Mcl-1. Molecular and cellular biology, 27(12), 4328-4339.

Zheng, Y., Delgoffe, G. M., Meyer, C. F., Chan, W., & Powell, J. D. (2009). Anergic T cells are metabolically anergic. The Journal of Immunology, 183(10), 6095-6101.

Zhou, D., Chu, W., Chen, D. L., Wang, Q., Reichert, D. E., Rothfuss, J., ... & Mach, R. H. (2009). [F-18]-and [C-11]-Labeled N-benzyl-isatin sulfonamide analogues as PET tracers for Apoptosis: synthesis, radiolabeling mechanism, and in vivo imaging study of apoptosis in Fas-treated mice using [C-11] WC-98. Organic & Biomolecular Chemistry, 7(7), 1337-1348.

Zhu, J., Yamane, H., & Paul, W. E. (2009). Differentiation of effector CD4 T cell populations. Annual review of immunology, 28, 445-489.